

Diss. ETH No. 21821

# **HEAT TRANSFER ENHANCEMENT IN A SOLAR BIOMASS GASIFIER**

A thesis submitted to attain the degree of  
DOCTOR OF SCIENCES of ETH ZURICH  
(Dr. sc. ETH Zurich)

presented by  
**MICHAEL KRÜSI**  
MSc ETH ME  
born 09.10.1985  
citizen of Schönengrund (AR)

accepted on the recommendation of  
Prof. Dr. Aldo Steinfeld, examiner  
Prof. Dr. Claudio Augusto Oller do Nascimento, co-examiner  
Dr. Zoran R. Jovanovic, co-examiner

2014



*to my fiancée, Sholpan*



## **Abstract**

This thesis investigates the production of synthesis gas, a mixture of hydrogen and carbon monoxide, via steam-based thermochemical gasification of biomass using concentrated solar energy for process heat.

Energy and exergy analyses of the gasification of Brazilian sugarcane bagasse revealed the potential benefits of solar-driven over conventional autothermal gasification that include the superior quality of the syngas and the higher yield per unit of feedstock. Theoretical upgrade factors (ratio of the energy content of syngas produced over that of the feedstock) of up to 126%, along with the treatment of wet feedstock and the elimination of the air separation unit, support the potential benefits of solar-driven over autothermal gasification.

Reaction rates for the gasification of fast pyrolyzed bagasse char were measured by thermogravimetric analysis and a rate law based on the oxygen exchange mechanism was formulated.

A two-zone laboratory-scale allothermal gasifier that combines drop-tube and fixed-bed concepts was developed with the aim to provide pyrolysis and gasification conditions yielding high carbon conversion into syngas and low amounts of tar and gaseous hydrocarbons. In the upper drop-tube zone, a high radiative heat flux to the dispersed particles induces their fast pyrolysis. In the lower zone, a fixed bed provides sufficient residence time and temperature for the char gasification and the decomposition of the other pyrolysis products. Testing was performed in an electric furnace. Experimental runs at reactor temperatures of 1073–1573 K and a biomass feed rate of 2.8 g/s·m<sup>2</sup> yielded high-quality syngas of molar ratios H<sub>2</sub>/CO = 1.6 and CO<sub>2</sub>/CO = 0.31, and with lower heating values of 15.3–16.9 MJ/kg, resulting in an upgrade factor of 112%.

The two-zone reactor concept was then further developed and a solar reactor was built and evaluated experimentally using simulated concentrated solar energy at a 1.5 kW solar input scale. In order to enhance the heat transfer to the lower char gasification zone, the fixed bed was replaced by a trickle bed established by a structured packing made of well conducting reticulate porous ceramic (RPC) foam. The packing provides residence time for the solids and enhances the heat transfer for the efficient char gasification and for the decomposition of the hydrocarbons. A series of 20 min gasification experiments comparing the two-zone reactor vs. a drop-tube reactor were performed with a maximum particle flux of 16 g/s-m<sup>2</sup>. It has been demonstrated that the former allows for more efficient decomposition of CH<sub>4</sub> and C<sub>2</sub> hydrocarbons at comparable reactor temperatures. The LHV of the product gas was around 15.9 MJ/kg, thus significantly higher than those typically obtained in conventional autothermal gasifiers. Solar energy was chemically stored in the product gas resulting in an upgrade factor of 105% and a maximum energy conversion efficiency of 21%. An analysis of the heat losses of the reactor identified the main losses via conduction through the insulation and along the reactor tube.

To study the heat and mass transfer in the trickle-bed zone of the two-zone reactor, an externally heated gas-solid trickle-flow reactor with a RPC packing was tested with beech char particles in a series of 43–51 min long experiments achieving carbon conversions of up to 52%. A two-dimensional finite volume model coupling chemical reaction with conduction, convection, and radiation of heat within the porous structure was developed and tested against experimentally observed temperatures and gasification rates. The sensitivity of the gasification rate and reactor temperatures to variations of the RPC's pore diameter, porosity, thermal conductivity, and particle loading was studied. Furthermore, a numerical comparison with a moving bed demonstrated that the increased heat transfer via combined radiation and conduction leads to a more uniform temperature distribution and higher gasification rates.

## Zusammenfassung

Die vorliegende Doktorarbeit untersucht die Herstellung von Synthesegas, einer Mischung aus Wasserstoff und Kohlenmonoxid, durch thermochemische Dampfvergasung von Biomasse mithilfe konzentrierter Sonnenenergie als Prozesswärme.

Eine energetische und exergetische Evaluierung der Dampfvergasung von brasilianischer Zuckerrohr-Bagasse zeigt die potenziellen Vorteile der solar betriebenen gegenüber der herkömmlichen autothermen Vergasung auf. Diese umfassen die überlegene Qualität des Synthesegases sowie die höhere Ausbeute pro Biomasseeinheit. Die theoretische Erhöhung des Energiegehalts des Synthesegases gegenüber dem Ausgangsstoff von 26%, sowie die sich eröffnenden Möglichkeiten feuchte Biomasse zu verwenden und auf eine Luftzerlegungsanlage zu verzichten unterstreichen die potentiellen Vorteile der solarbetriebenen gegenüber der herkömmlichen Vergasung.

Die Reaktionsraten der Vergasung von schnell pyrolysierten Bagassekohle wurden durch thermogravimetrische Analyse gemessen. Daraus wurde dann ein Geschwindigkeitsgesetz auf der Grundlage des Sauerstoff-Austausch-Mechanismus formuliert.

Ein Zweizonenvergaser im Labormassstab, der Fallrohr- und Festbettkonzepte kombiniert, wurde mit dem Ziel entwickelt, Pyrolyse- und Vergasungsbedingungen zu schaffen, die für einen hohen Umsatz der Kohle zu Synthesegas sowie für geringe Mengen Teer und gasförmiger Kohlenwasserstoffe sorgen. In der oberen Fallrohrzone induziert ein hoher Strahlungswärmefluss die schnelle Pyrolyse der dispergierten Biomassepartikel. In der unteren Zone stellt ein Festbett genügend lange Feststoffverweilzeiten und genügend hohe Temperaturen für die Kohlevergasung und die Zersetzung der anderen Pyrolyseprodukte zur Verfügung. Die experimentellen Tests wurden an einem Elektroofen bei Temperaturen im Bereich 1073–1573 K und Biomasseströmen von  $2.8 \text{ g/s} \cdot \text{m}^2$

durchgeführt. Dabei wurde qualitativ hochwertiges Synthesegas mit molaren H<sub>2</sub>/CO- und CO<sub>2</sub>/CO-Verhältnissen von 1.6 bzw. 0.31 sowie Heizwerten von 15.3–16.9 MJ/kg produziert. Dies entspricht einer Erhöhung des Energiegehalts gegenüber dem Ausgangsstoff um 12%.

Das Zweizonen-Reaktorkonzept wurde dann weiterentwickelt und es wurde ein Solarreaktor gebaut und experimentell unter simulierter konzentrierter Sonnenenergie bei Eingangsleistungen bis 1.5 kW getestet. Um den Wärmetransport in der untenliegenden Kohlevergasungszone zu verbessern wurde das Festbett durch ein Rieselbett ersetzt. Das Rieselbett wurde mithilfe einer strukturierten Packung aus netzartiger poröser Keramik mit guter Wärmeleitfähigkeit realisiert. Die Packung schafft genügend hohe Feststoffverweilzeiten und erhöht den Wärmetransport für eine effiziente Kohlevergasung und die Zersetzung der Kohlenwasserstoffe. Zum Vergleich des Zweizonen-Reaktors mit einem Fallrohrreaktor wurde eine Serie 20-minütiger Vergasungsexperimente mit maximalen Feststoffmassenflüssen von 16 g/s·m<sup>2</sup> durchgeführt. Es konnte gezeigt werden, dass der erstere bei vergleichbaren Temperaturen eine effizientere Zersetzung von CH<sub>4</sub> und C<sub>2</sub>-Kohlenwasserstoffen erlaubt. Der Heizwert des Produktgases war mit 15.9 MJ/kg signifikant höher als die typischerweise in konventionellen autothermen Vergasern erreichten Werte. Solar-energie konnte erfolgreich chemisch im Produktgas gespeichert werden. Die Erhöhung des Energiegehalts des Synthesegases gegenüber dem Ausgangsstoff betrug 5%. Dabei wurde eine maximale Energieumsatzeffizienz von 21% erreicht. Mit einer Wärmeverlustanalyse des Solarreaktors wurden die Wärmeleitung durch die Isolation sowie entlang des Reaktorrohres als die grössten Verluste identifiziert.

Um den Wärme- und Stofftransport im Rieselbett des Zweizonen-Reaktors genauer zu untersuchen wurde ein extern beheizter Gas-Feststoff-Rieselbettreaktor mit einer porösen Keramikpackung in einer Serie von 43–51-minütiger Experimente mit Buchenholzkohengreis getestet. Dabei wurde ein Kohlenstoffumsatz von 52% erreicht. Es wurde ein zweidimensionales Finite-Volumen-Modell für Wärmeübergang und Stofftransport entwickelt. Dieses koppelt die chemische Reaktion mit dem Wärmetransport innerhalb der porösen Struktur durch Wärmeleitung, Konvektion und Strahlung. Die Modell-

vorhersagen wurden mit den im Reaktor gemessenen Temperaturen und Vergasungsraten verglichen. Eine Sensitivitätsanalyse zeigt den Einfluss von Veränderungen des Poredurchmessers, der Porosität, der Wärmeleitfähigkeit und der Partikelbeladung des RPC's auf die Vergasungsrate und die Reaktortemperaturen. Ein numerischer Vergleich mit einem Wanderbettreaktor demonstrierte, dass die Erhöhung des Wärmetransports durch kombinierte Wärmeleitung und -strahlung zu einer gleichmässigeren Temperaturverteilung sowie höheren Vergasungsraten führt.



## Acknowledgements

First of all, I thank Prof. Dr. Aldo Steinfeld, head of the Professorship of Renewable Energy Carriers at ETH Zürich, for giving me the opportunity to perform my dissertation in this interesting, challenging, and exciting field of research, and for his supervision and support.

I am very grateful to Prof. Claudio Augusto Oller do Nascimento from the Departamento de Engenharia Química, at the Escola Politécnica of the Universidade de São Paulo for the collaboration in the project, the inspiring support, and for acting as a co-examiner.

Very special thanks go to Dr. Zoran Jovanovic, my direct supervisor, for his guidance, the many challenging and critical discussions, and for being co-examiner. His confidence in my work and his support were extremely important for my motivation and the success of this work.

I thank Dr. Andreas Haselbacher for his support in the modeling tasks of this work and Dr. Hyug Chul Yoon my former advisor.

I acknowledge the support of Dr. Christian Wieckert and Alwin Frei from the Solar Technology Laboratory at the Paul Scherrer Institute.

I thank the Bachelor and Master students Serge Zihlmann, Jules Petit, Alexander David, Elena Cândida dos Santos, Michele Bernini, and Adrian Ljutic for their contributions to this work and support in the experimental campaigns.

I acknowledge the technical support in the design and construction of the experimental setups that I have received from Philipp Haueter, Dominik Herrmann, and Laurenz Schlumpf.

I thank all my colleagues at the Professorship of Renewable Energy Carriers for providing a joyful research environment. Special thanks go to my longtime office mates Thomas Cooper, Philipp Furler, and Peter Poživil for the many fruitful personal and scientific discussions, Dr. Nicolas Piatkowski and Dr.

Gilles Maag who supported me with their knowledge of solar gasification, and Dr. Jonathan Scheffe and Dr. Matt Roesle for their many inputs.

I would like to thank my parents Cornelia and Werner, my sister Alexandra, and all friends for the support they have given me over all the years.

Last but not least I thank my fiancée Sholpan for her love, support, and encouragement she has given me throughout my doctoral studies.

This project has been made possible by the financial support of the Brazilian-Swiss Joint Research Programme (Grant Agreement No. BJRP 011005).

# Contents

<b>Abstract .....</b>	<b>v</b>
<b>Zusammenfassung .....</b>	<b>vii</b>
<b>Acknowledgements .....</b>	<b>xi</b>
<b>Nomenclature .....</b>	<b>xvii</b>
<b>1      Introduction .....</b>	<b>1</b>
1.1     Thesis Outline .....	4
<b>2      Background .....</b>	<b>7</b>
2.1     Principles of Biomass Gasification.....	7
2.1.1    Pyrolysis .....	8
2.1.2    Gasification.....	9
2.1.3    Tar Formation and Reduction .....	11
2.2     Conventional Biomass Gasifier Technology .....	12
2.3     Solar Gasifier Technology.....	16
<b>3      Feedstocks .....</b>	<b>21</b>
3.1     Sugarcane Bagasse .....	21
3.2     Beech Char .....	22
3.3     Physical and Chemical Properties .....	22
<b>4      Thermodynamics of Bagasse Gasification .....</b>	<b>25</b>
4.1     Equilibrium Considerations.....	25
4.2     1 <sup>st</sup> and 2 <sup>nd</sup> Law Analyses .....	30
4.3     Conclusions .....	36

<b>5</b>	<b>Gasification Kinetics of Bagasse.....</b>	<b>39</b>
5.1	Thermogravimetric Analysis.....	39
5.2	Rate Law .....	42
5.2.1	Reaction Mechanism .....	42
5.2.2	Surface Area Dependence .....	44
5.2.3	Evaluation of the Rate Constants.....	46
5.3	Conclusions.....	48
<b>6</b>	<b>Drop-Tube Fixed-Bed Solar Gasifier Concept .....</b>	<b>49</b>
6.1	Gasifier Concept .....	49
6.2	Gasifier Testing in an Electric Furnace.....	50
6.2.1	Experimental Setup and Procedures .....	50
6.2.2	Results .....	52
6.3	Conclusions.....	55
<b>7</b>	<b>Drop-Tube Trickle-Bed Solar-Driven Gasifier.....</b>	<b>57</b>
7.1	Gasifier Concept .....	57
7.2	Gasifier Testing on a High Flux Solar Simulator.....	60
7.2.1	Experimental Setup .....	60
7.2.2	Experimental Procedure .....	62
7.3	Results and Discussion.....	64
7.4	Energy Balance and Heat Losses .....	72
7.4.1	Heat Transfer to Reactants .....	73
7.4.2	Radiation Losses.....	74
7.4.3	Convective Losses .....	75
7.4.4	Conduction through the Cavity Walls .....	77
7.4.5	Conduction along Reactor Tube .....	77
7.4.6	Interpretation .....	78
7.5	Conclusions.....	80

---

<b>8</b>	<b>Heat- and Mass-Transfer Analysis of a Trickle-Bed Gasifier .....</b>	<b>83</b>
8.1	Experimental Investigation.....	84
8.1.1	Experimental Setup.....	84
8.1.2	Experimental Procedure.....	87
8.1.3	Experimental Results .....	88
8.2	Numerical Model.....	90
8.2.1	Governing Equations .....	90
8.2.2	Boundary Conditions .....	94
8.2.3	Domain Properties .....	96
8.2.4	Numerical Implementation .....	98
8.2.5	Code Verification.....	99
8.3	Simulation Results.....	101
8.3.1	Model Predictions versus Experimental Results.....	101
8.3.2	Sensitivity Analysis .....	103
8.3.3	Numerical Comparison of the Trickle Bed to a Moving Bed .....	108
8.4	Conclusions .....	113
<b>9</b>	<b>Overall Conclusions and Outlook .....</b>	<b>115</b>
9.1	Thermodynamics and Kinetics .....	115
9.2	Reactor Design and Testing.....	117
9.3	Modeling .....	118
9.4	Outlook.....	119
<b>A</b>	<b>Appendix A: Solar Gasification of Microalgae in a Drop-Tube .....</b>	<b>121</b>
A.1	Materials .....	123
A.2	Experimental Setup .....	125
A.3	Experimental Procedures .....	126
A.4	Results .....	128
A.5	Conclusions .....	133

<b>Appendix B: Thermal Conductivity of a Bed of Char .....</b>	<b>135</b>
<b>Appendix C: Numerical Implementation of the Heat and Mass Transfer Model.....</b>	<b>139</b>
C.1    Definitions.....	139
C.2    Discretization .....	140
C.3    Determination of the Flow Field .....	143
C.4    Species Equation.....	145
C.5    Fluid Phase Energy Equation.....	148
C.6    Solid Phase Energy Equation.....	152
C.7    Solution Strategy.....	153
<b>List of Figures .....</b>	<b>155</b>
<b>List of Tables .....</b>	<b>161</b>
<b>References .....</b>	<b>163</b>
<b>Curriculum Vitae .....</b>	<b>177</b>
<b>List of Publications.....</b>	<b>179</b>

# Nomenclature

## Latin Characters

$A$	surface area, m <sup>2</sup>
$A_0$	specific surface area, m <sup>2</sup> /m <sup>3</sup>
$C$	solar concentration ratio, -
$C_p$	(isobaric) heat capacity, J/kg-K
$d$	diameter, m
$d_p$	particle size, m
$D$	diffusion/dispersion coefficient, m <sup>2</sup> /s / thickness, m
$e_s$	sensible energy, J/m <sup>3</sup>
$E$	error, -
$E_A$	activation energy, J/mol
$\dot{Ex}_{\text{destr}}$	exergy destruction rate, W
$\dot{Ex}_{\text{loss}}$	exergy loss rate, W
$F$	configuration factor, -
$g$	acceleration of gravity, 9.81 m/s <sup>2</sup>
$h$	mass specific enthalpy, J/kg / height, m
$\bar{h}$	molar enthalpy, J/mol
$h_s$	mass specific sensible enthalpy, J/kg
$h_{\text{sf}}$	interfacial heat transfer coefficient, W/m <sup>2</sup> -K
$\Delta \bar{h}_f^0$	enthalpy of formation, J/mol
$\Delta h_R$	reaction enthalpy, J/kg
$\Delta \bar{h}_R$	reaction enthalpy, J/mol
$\dot{H}$	enthalpy flow, W
$I$	direct normal insolation (DNI), W/m <sup>2</sup>
$k$	reaction rate, according to rate law / thermal conductivity, W/m-K
$k_0$	frequency factor, s <sup>-1</sup>
$K$	extinction coefficient, m <sup>-1</sup>

$l$	loading, -
$L$	length, m
LHV	lower heating value, J/kg
$m$	mass, kg
$\dot{m}$	mass flow rate, kg/s
$\dot{m}_c$	mass consumption rate of carbon per unit volume, kg/s-m <sup>3</sup>
$M$	molar mass, kg/mol
$\dot{n}$	molar flow rate, mol/s
$N$	number of moles, mol
$p$	pressure / partial pressure, Pa
$P$	perimeter, m
$q$	heat flux, W/m <sup>2</sup>
$q_a$	order of accuracy, -
$\dot{Q}$	heat transfer rate, W
$r$	radial coordinate, m / reaction rate, s <sup>-1</sup>
$R$	molar gas constant, 8.31447 J/mol-K / residual, -
$S$	mass source, kg/m <sup>3</sup> -s / surface area, m <sup>2</sup> / molar entropy, J/mol-K
$t$	time, s
$T$	temperature, K
$u$	velocity (superficial in porous domain), m/s
$U$	upgrade factor, -
$V$	volume, m <sup>3</sup>
$v^c$	correction velocity, m/s
$w_k$	mass fraction of species $k$ , -
$\dot{W}_{\text{ASU}}$	power to air separation unit (ASU), W
$x$	elemental molar ratio of H/C, -
$x_i$	mass fraction of species $i$ in the solid, -
$X$	conversion, -
$y$	elemental molar ratio of O/C, -
$y_k$	mole fraction of species $k$ , -
$z$	axial coordinate, m

---

## Greek Characters

$\alpha$	absorptivity, -
$\varepsilon$	emissivity, -
$\bar{\varepsilon}$	molar exergy, J/mol
$\eta$	thermal efficiency, -
$\eta_{\text{abs}}$	absorption efficiency, -
$\eta_{\text{ex}}$	exergetic efficiency, -
$\theta$	surface coverage, -
$\kappa$	optical thickness, -
$\mu$	dynamic viscosity, Pa-s
$\nu$	kinematic viscosity, m <sup>2</sup> /s
$\rho$	density, kg/m <sup>3</sup>
$\sigma$	Stefan-Boltzmann's constant, 5.67·10 <sup>-8</sup> W/m <sup>2</sup> ·K <sup>4</sup>
$\tau$	tortuosity, -
$\phi$	equivalence ratio, -
$\varphi$	porosity, -

## Subscripts

$\parallel$	parallel to flow
$\perp$	perpendicular to flow
0	at normal conditions ( $T_0 = 273.15$ K, $p_0 = 101,325$ Pa) / initial
apt	aperture
cav	cavity
ch	chemical
cond	conduction
conv	convection
eff	effective
exp	experiment
f	final / fluid
ins	insulation

<i>k</i>	species index
liq	liquid
med	medium
nom	nominal
prod	products
quench	quencher
rad	radiation
reac	reactants
rerad	reradiation
s	solid
sim	numerical simulation
sol-chem	solar to chemistry
surf	surface
tot	total

### Dimensionless Groups

Gr	Grashof number
Nu	Nusselt number
Pe	Péclet number
Pr	Prandtl number
Ra	Rayleigh number
Re	Reynolds number

---

## Abbreviations

ASU	air separation unit
CPC	compound parabolic concentrator
CSP	concentrated solar power
DMC	dichloromethane
DNI	direct normal insolation
ETH	Eidgenössische Technische Hochschule (Swiss Federal Institute of Technology)
FVM	finite volume method
GC	gas chromatography
HEX	heat exchanger
HFSS	high flux solar simulator
LHV	lower heating value
MB	moving bed
MMS	method of manufactured solutions
ppi	pores per inch
PV	photovoltaics
RPC	reticulate porous ceramic



# **Chapter 1**

## **Introduction**

Affordable, transportable, and dispatchable energy is a key driver for a thriving economy. Today's world primary energy demand is around 13,100 Mtoe<sup>a</sup> (2011) of which 82% are covered by fossil sources [1]. The energy demand is expected to increase sharply to 17,400–18,600 Mtoe by 2035. This is an increase of 33–43% over today's demand. The increase is mainly due to global population growth and expanding economic activity. The rate of consumption of fossil fuels is higher than their formation rate which inevitably leads to a limited supply in the future. Moreover, concerns about climate change due to CO<sub>2</sub> emissions call for a reduction in the usage of fossil fuels [2].

To match demand and supply in the long term while limiting CO<sub>2</sub> emissions and keeping energy prices at an affordable level, efforts have to be made on both, the demand and the supply side. On the demand side, a reduction in energy intensity is crucial. Although technological progress is made, the projected reductions cannot offset the demand growth as the population and economic growth are larger than the efficiency gains [1].

For the electricity market, additional supply of low carbon energy may be provided by renewable sources such as wind, biomass, geothermal and solar (PV and CSP), or nuclear power. For the transportation and the petrochemicals sector, the key drivers for increasing oil demand [1], these technologies have limited applicability. Especially for transportation, where high energy density is critical, liquid hydrocarbon fuels are indispensable.

The use of concentrated solar energy for chemical processes can play an important role in the transition away from fossil towards renewable

---

<sup>a</sup> million tonnes of oil equivalent, 1 Mtoe = 41.868 PJ

transportation fuels. Although the solar energy hitting the earth's surface is very dilute ( $\sim 1 \text{ kW/m}^2$ ), it can be concentrated by focusing it with mirrors. The concentrated solar energy can then be utilized as energy source to drive high temperature thermochemical processes such as the production of syngas a, mixture composed of  $\text{H}_2$  and  $\text{CO}$  [3]. Thereby, the intermittent solar energy can be chemically stored. Syngas is a primary building block for the production of chemicals and transportation fuels. It can be processed to  $\text{H}_2$  via water-gas shift reaction or to liquid hydrocarbon fuels such as diesel or kerosene via Fischer-Tropsch synthesis, or to methanol and then gasoline via the methanol-to-gasoline process (Mobil). Alternatively, the syngas may be used for the production of other chemicals or directly as a combustion fuel for power generation.

The production of liquid transportation fuels has several benefits as they are storable, transportable (from optimal production sites to where the demand is), and do not require a change in the massive global distribution and fueling infrastructure or in the highly developed vehicle propulsion technologies. There are two promising routes for the production of solar fuels [4]. In the short/midterm the path to solar syngas is via thermochemical gasification of carbonaceous feedstocks such as coal, biomass, and carbon containing waste materials. The long-term route is the production of syngas directly from  $\text{H}_2\text{O}$  and  $\text{CO}_2$  via solar thermochemical cycles. This work focuses on the short/midterm pathway of solar-driven steam gasification of carbonaceous feedstock, specifically the gasification of biomass illustrated in Figure 1-1. The use of biomass feedstock makes the product of any of the above mentioned conversion processes to chemicals, energy, or transportation fuels, in principle,  $\text{CO}_2$  neutral because of the biogenic source of syngas. The biomass feedstocks used in this work are Brazilian sugarcane bagasse, a residue from the sugar and ethanol production, and beech char.

At temperatures of 1000 K or higher and in the presence of steam, biomass is thermochemically converted into syngas via highly endothermic reactions. The conversion comprises two main steps: (1) pyrolysis, producing tar, gases and char, and (2) steam-based gasification and reforming of char, gas, and tar to form syngas [5].



In conventional autothermal gasifiers such as the Texaco entrained flow gasifier, the GTI high-pressure oxygen-blown fluidized bed gasifier, or the gasifiers specifically studied for the gasification of bagasse [6-9], the heat required for the gasification is supplied by combusting a significant amount of the feedstock in-situ with a stream of air or pure O<sub>2</sub>. The combustion consumes about 30–40% of the feedstock [10, 11], reducing its utilization and the quality of the syngas due to combustion byproducts, i.e. increased amounts of CO<sub>2</sub> in the syngas, lower H<sub>2</sub>/CO ratio, and a lower calorific value. Indirectly heated (allothermal) gasifiers such as dual fluidized bed gasifiers [12] can overcome the reduction of quality due to combustion byproducts but they still require a significant amount of the feedstock to be combusted to provide the reaction enthalpy.

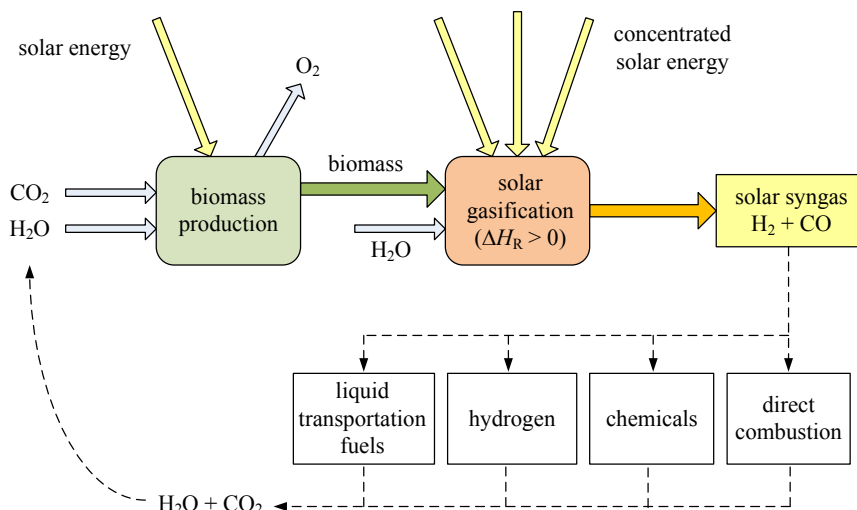


**Figure 1-1:** Solar-driven steam gasification process flow sheet.

Solar-driven gasification uses highly concentrated solar radiation as source of high-temperature process heat to drive the steam-based gasification of the carbonaceous feedstock. Thus, solar energy in an amount equal to the enthalpy change of the endothermic reactions (Eqs. 1.1 and 1.2) is chemically stored, which leads to a syngas with a higher calorific content per unit of feedstock. The smaller amount of low-density feedstock that is needed to produce the same output reduces capital and operating costs related to transportation, storage, pre-processing, and feeding of the biomass. Furthermore, the absence of combustion eliminates the need for pure oxygen from an air separation plant. Since no internal combustion products contaminate the syngas, the required size of CO<sub>2</sub> separation plant is reduced. All these advantages may justify the specific cost of solar concepts brought in by the concentrating mirror system and the syngas storage imposed by intermittent availability of solar energy.

## 1.1 Thesis Outline

This thesis aims at developing solar reactor technology for the thermochemical conversion of biomass to syngas via pyrolysis and gasification. It was carried out in the framework of a joint research project of the Universidade de São Paulo, Brazil and ETH Zürich, Switzerland.

Chapter 2 gives a background on the principles of biomass gasification, different gasification technologies such as auto- and allothermal gasification, and solar gasification technology. In Chapter 3, the investigated feedstocks are introduced and characterized. Chapter 4 studies the thermodynamic equilibrium compositions for solar and autothermal gasification of Brazilian sugarcane bagasse emphasizing the differences in syngas quality. Moreover, first and second law analyses are carried out in order to assess the performance of the solar and the autothermal gasification, to find the maximum energy and exergy conversion efficiencies, and to identify the major sources of irreversibility. In Chapter 5, a thermogravimetric analysis is performed and a kinetic rate law for the gasification of bagasse char is formulated as a design basis for a solar-driven gasifier. Chapter 6 presents a solar reactor concept for the gasification of

highly volatile biomass feedstock that is based on a combination of drop-tube and fixed bed designs. Further, gasification of bagasse is experimentally tested in a tubular externally heated gasifier. In Chapter 7, the reactor design is refined and a solar reactor consisting of a drop-tube and a trickle-bed zone is built and tested at ETH's high flux solar simulator. The performance of the two-zone reactor is experimentally examined with sugarcane bagasse particles and compared to the performance of a drop-tube configuration. In Chapter 8, an externally heated gas-solid trickle-flow reactor with a well-conducting reticulate porous ceramic (RPC) packing is tested with beech char particles. Moreover, a two-dimensional finite volume heat and mass transfer model coupling chemical reaction with heat and mass transfer is developed. Its predictions are compared to the experimental measurements and its sensitivity to parameter changes is analyzed. Further, a model comparison of the trickle-flow reactor to a moving bed reactor is discussed. Finally, the overall conclusions and an outlook are presented in Chapter 9.



## **Chapter 2**

### **Background**

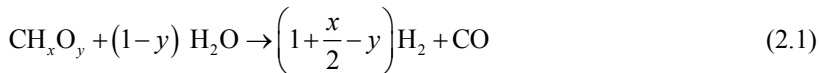
#### **2.1 Principles of Biomass Gasification**

Biomass is bulky and has a low energy density ( $LHV \approx 15\text{--}19\text{ MJ/kg}$ ) [13]. This makes its handling, storage and transportation difficult and expensive. The gasification of the biomass is an attractive path to convert this low-value material into high-value products. In the gasification process, a wide range of carbonaceous materials can be converted into a combustible gas or a synthesis gas containing mainly  $H_2$ ,  $CO$ ,  $CO_2$ , and  $CH_4$ .

The thermochemical conversion of biomass into synthesis gas is usually performed at temperatures of 1000 K or higher using air, oxygen, steam, or  $CO_2$  as gasifying medium. Depending on the gasifier design and gasifying medium, the gasification process may involve several of the following physical, chemical, or thermal process steps [14]:

- drying
- thermal decomposition or pyrolysis
- partial combustion
- gasification of decomposition products

For the gasification of biomass with steam to synthesis gas, as it is proposed in this work, the overall thermochemical conversion can be expressed by the idealized simplified net reaction



where  $x$  and  $y$  are the elemental molar ratios of H/C and O/C in the biomass.

### 2.1.1 Pyrolysis

Pyrolysis is the thermal decomposition of the feedstock into char, gases, and tar in the total absence or a limited supply of an oxidizing agent such as  $\text{O}_2$ ,  $\text{H}_2\text{O}$ , or  $\text{CO}_2$ . It is an essential process step in every gasifier. Figure 2-1 illustrates the pyrolysis of a biomass particle. When the biomass is heated to temperatures above 500 K via radiation and convection, gas such as light volatile hydrocarbons,  $\text{H}_2$ ,  $\text{CO}$ ,  $\text{CO}_2$ , and tar are released, leaving behind char. The tar then undergoes secondary gas-phase reactions in which the large complex hydrocarbons break down into smaller molecules.

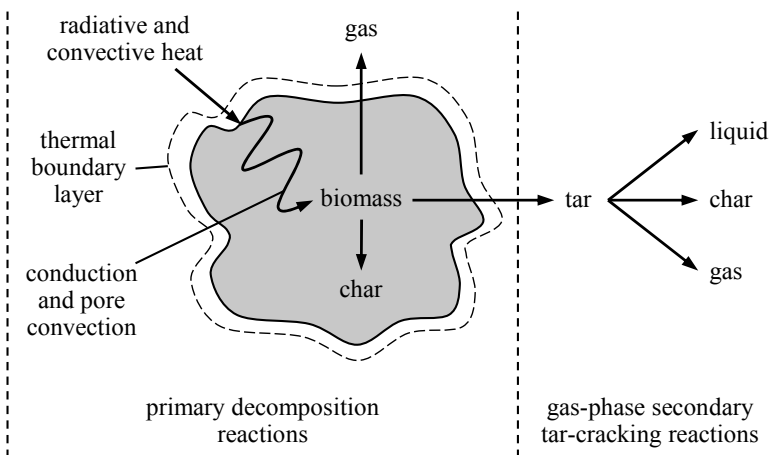


**Figure 2-1:** Primary and secondary reactions during pyrolysis of a biomass particle. Adapted from ref. [14].

The final pyrolysis products can be classified as [14]:

- solid (char or carbon)
- liquid (tar, heavy hydrocarbons, water)
- gaseous ( $H_2$ , CO,  $CO_2$ ,  $CH_4$ , and light hydrocarbons)

The biomass pyrolysis conditions such as heating rate, gas temperature, and residence time have a strong influence on the release of tar and gases, as well as on the formation and reactivity of the char. In general, the release of volatiles is enhanced and char formation suppressed by rapid high-temperature pyrolysis [15, 16]. Such pyrolysis conditions yield only low amounts of char that has a high reactivity [17-20]. Moreover, high gas temperatures facilitate cracking of tar and other hydrocarbons [18, 21-23]. Slower heating and longer residence time lead to the formation of secondary char, which is produced from a reaction between the primary char and the volatiles [14].

### **2.1.2 Gasification**

In the gasification step, char and hydrocarbons released during the pyrolysis react with an oxidant such as air, oxygen, steam, or  $CO_2$  to produce syngas. It is usually performed in the temperature range 1000–1300 K and can be exothermic or endothermic depending on the oxidant used. The primary solid remainder of the gasification is ash, which consists of mineral matter and minor amounts of unreacted carbon.

The gasification and reforming of the char and the hydrocarbons are complex processes consisting of several homogeneous and heterogeneous reactions. The principal reactions and their reaction enthalpies are given by Eqs. 2.2–2.10 [24].

### Combustion reactions



### Water-gas reaction



### Boudouard reaction



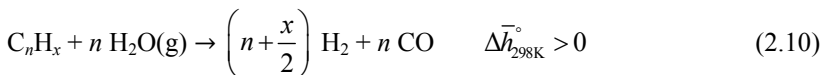
### Hydrogasification reaction



### Water-gas shift reaction



### Steam reforming reactions



The rates of the heterogeneous reactions vary greatly with the combustion reaction (Eq. 2.2) being the fastest followed by the water-gas reaction (Eq. 2.5), the Boudouard reaction (Eq. 2.6), and the hydrogasification reaction (Eq. 2.7) [14].

$$R_{\text{C+O}_2} \gg R_{\text{C+H}_2\text{O}} > R_{\text{C+CO}_2} \gg R_{\text{C+H}_2} \quad (2.11)$$

Although the production of char with high reactivity, discussed in the previous section, is beneficial for the heterogeneous char gasification reactions, the char gasification remains the rate limiting step of the overall process [5]. The water-gas shift reaction (Eq. 2.8) is of particular interest for the production of synthesis gas as it allows adjusting the CO/H<sub>2</sub> ratio for the production of liquid fuels.

### 2.1.3 Tar Formation and Reduction

Tar is an undesired byproduct of the pyrolysis step. Devi et al. [25] define it as a complex mixture of condensable hydrocarbons, which includes single- to 5-ring hydrocarbons, other oxygen-containing hydrocarbons, and complex polycyclic aromatic hydrocarbons. In other definitions, all organic product gas contaminants with molecular mass larger than 78, i.e. larger than benzene are considered as tar [26].

Tar can condensate and plug downstream equipment, and contaminate the product gas limiting its use. Keeping the tar levels low is necessary as most downstream processes can only handle a certain amount of tar. Internal combustion and diesel engines tolerate 10–100 mg/Nm<sup>3</sup> and gas turbines 0.5–5 mg/Nm<sup>3</sup> [27]. For synthesis gas applications such as methanol or Fischer-Tropsch synthesis, the tar content should not exceed 0.1 mg/Nm<sup>3</sup> [28] as tar poisons the catalyst.

Tar is mainly produced during the pyrolysis phase. In the temperature range of 500–800 K, the biomass components cellulose, hemicellulose, and lignin break down into primary tar. At temperatures above 800 K, primary tar components start to decompose into lighter non-condensable gases (CO<sub>2</sub>, CO, H<sub>2</sub>O, and light hydrocarbons), and longer chain hydrocarbons molecules known as secondary tar. At temperatures higher than 1050 K, primary tar is destroyed and tertiary tar such as benzene, naphthalene, and 3- and 4-ring aromatics are produced. [14, 29]

The methods to reduce the amount of tar can be classified into primary and secondary methods. The primary methods avoid or convert tar formed within the gasifier by adjusting the operating conditions that play an important role in the tar formation and reduction. An increase in the gasifier temperature reduces most tar components. Only the formation of tertiary is increased tar. For many gasifier types, a limiting factor to the increase in temperature is the risk of sintering or melting of the ash. For the gasification with steam, an increase in the steam to biomass ratio also leads to a reduction in the tar content. Tar and other hydrocarbons are then reduced via steam-reforming reactions. [14]



The addition of a catalyst to the gasifier is another primary method for the reduction of tar. Dolomite, olivine, alkali metal, nickel and also char are catalytically active and enhance tar reforming within the gasifier. [25]

Secondary methods reduce the tar content downstream of the reactor via thermal or catalytic cracking, or via mechanical separation using cyclones, filters, etc. [25].

## 2.2 Conventional Biomass Gasifier Technology

Several reactor types are being studied or are industrially used for the gasification of biomass. These include updraft, downdraft, fluidized bed, dual fluidized bed, and entrained-flow gasifiers, of which a brief description is given below. Figure 2-2 gives a schematic overview of these gasifier types and their main flow streams. The colors indicate the relative reactor temperatures. Red stands for hot, yellow for medium, and gray for cold sections of the reactor. An overview of typical gas compositions is given in Table 2-1.

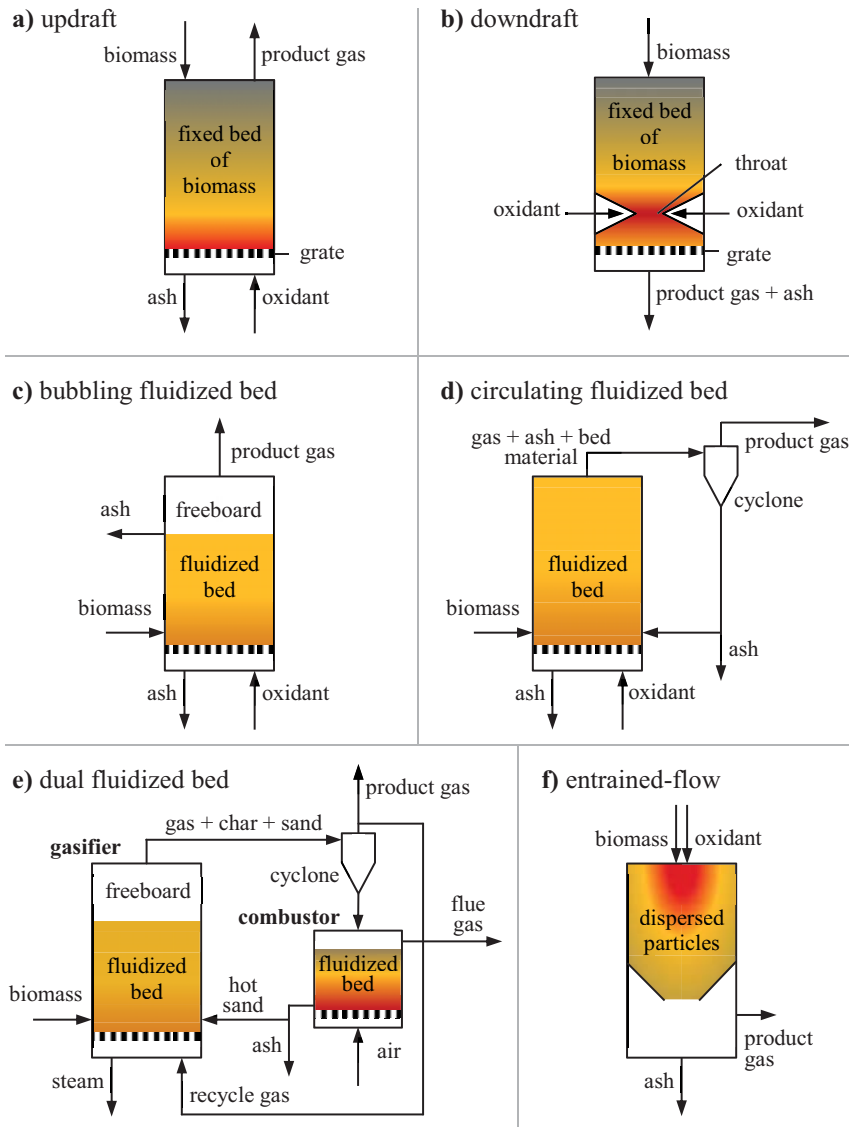


**Figure 2-2:** Biomass gasifier types with main flow streams: a) updraft (countercurrent), b) downdraft (concurrent), c) bubbling fluidized bed, d) circulating fluidized bed, e) dual fluidized bed, and f) entrained-flow. Colors indicate relative temperatures (red = hot, yellow = medium, gray = cold). Adapted from ref. [5].

In updraft gasifiers schematically shown in Figure 2-2a, a packed bed of biomass supported by a grate moves downwards. The oxidant is introduced from the bottom and the product gas is withdrawn from the top. Ash is removed at the bottom of the gasifier. Such a design is very simple, robust, and scalable. Due to its countercurrent arrangement it offers a high thermal efficiency, yields a high carbon conversion, and can tolerate feedstock moisture contents of up to 60%<sub>wt</sub>. The tar levels are very high because the gaseous and liquid pyrolysis products never pass the hottest zone of the reactor. It is thus unsuitable for the production of clean product gas for highly volatile feedstocks. [5, 14]

Downdraft gasifiers, as depicted in Figure 2-2b, have a descending packed bed of biomass that is supported by a throat at which air or oxygen is injected. Both, the gas and the solids flow downwards concurrently. The tar and the gaseous hydrocarbons released during pyrolysis in the upper zone of the gasifier pass through the turbulent oxidation zone that is maintained at temperatures in the range of 1273–1473 K and are cracked and reformed. The relatively clean product gas with low tar and volatile hydrocarbon levels makes oxygen- and air-blown downdraft gasifiers the preferred concepts for the production of high quality syngas from highly volatile feedstocks. Due to the throats limited size the scalability is low. The tolerated level of moisture is up to 25%<sub>wt</sub>–30%<sub>wt</sub>. [5, 14]

**Table 2-1:** Typical product gas composition for different biomass gasifiers.

gasifier type	gas composition [% <sub>vol</sub> ]				
	H <sub>2</sub>	CO	CO <sub>2</sub>	CH <sub>4</sub>	N <sub>2</sub>
updraft (air-blown) <sup>*</sup>	11	24	9	3	53
downdraft (air-blown) <sup>*</sup>	17	21	13	1	48
downdraft (oxygen-blown) <sup>*</sup>	32	48	15	2	3
fluidized bed (air-blown) <sup>*</sup>	9	14	20	7	50
dual fluidized bed <sup>†</sup>	38	27	21	11	3

<sup>\*</sup> from ref. [5]

<sup>†</sup> from ref. [30]

There are two types of single fluidized bed gasifiers used for biomass: bubbling (Figure 2-2c) and circulating (Figure 2-2d). In the bubbling fluidized bed gasifiers, the solids stay in reactor because the fluid velocity is low. In the circulating fluidized bed gasifiers, the fluid velocity is higher so that a large part of the solids are entrained in the product gas. The solids are then separated with a cyclone and returned to the gasifier to increase the carbon conversion, which is eventually higher than in the bubbling bed. Both fluidized bed concepts are characterized by a good gas-solid mixing and high temperature uniformity. The typical operating temperatures are between 1073 and 1173 K. The tar levels in the product gas are between the levels of updraft and downdraft gasifiers. [5, 14]

Dual fluidized bed gasifiers (Figure 2-2e) are allothermal, which allows gasifying the biomass using pure steam. Hot sand is used to supply the reaction enthalpy to the gasifier. The sand is heated in a separate fluidized bed combustor that burns the char produced in the gasifier. Dual fluidized bed gasifiers yield medium heating value gas without requiring pure O<sub>2</sub> as oxidant. As the gasification is done with steam, the product gas contains high amounts of H<sub>2</sub>. Without additional fuel in the combustor, the temperatures in the gasifier are low (~1073 K) resulting in high CH<sub>4</sub> and moderate tar levels. The design is very complex and costly. [5, 14, 30]

In entrained-flow gasifiers (Figure 2-2f), the solid feedstock and the oxidant are injected into the chamber from the top or the side with a high velocity jet. The ash and the product gas leave the chamber at the bottom and are then separated. The reactor temperatures are usually well above 1273 K. This means that the ash accrues as a slag. The high reactor temperatures especially at the inlet lead to a good tar decomposition. Entrained-flow gasifiers are successfully used for large scale coal gasification but its suitability for the commercial gasification of biomass is questionable. The short residence times of only a few seconds require very fine particles, which are difficult to produce from fibrous biomass. Moreover, the molten ash is very aggressive and can corrode the reactor lining. [5, 14]

### 2.3 Solar Gasifier Technology

For the steam gasification of carbonaceous feedstock reactor temperatures in the range of 1000–1500 K have to be reached. Providing these temperatures by solar energy requires a mean solar concentration ratio on the order of  $C = 1,000\text{--}2,000$  suns<sup>a</sup>. Such concentrations can be provided by two types of solar concentrating systems, parabolic dishes ( $C = 1,000\text{--}10,000$  suns) and tower configurations ( $C = 500\text{--}5,000$  suns) [3]. Solar gasification reactors are usually designed to operate in conjunction with a solar tower system due to the larger scale of the system. As shown in Figure 2-3a, the solar reactor is positioned on top of a central tower that is surrounded by a large field two-axis tracking mirrors, so-called heliostats. The incident solar radiation is being reflected by the heliostats and concentrated at the aperture of the solar reactor to supply high-temperature heat to the endothermic steam gasification process. For solar reactor configurations with an aperture at the top of the reactor, beam-down systems as shown in Figure 2-3b are used. A mirror, commonly of hyperbolic

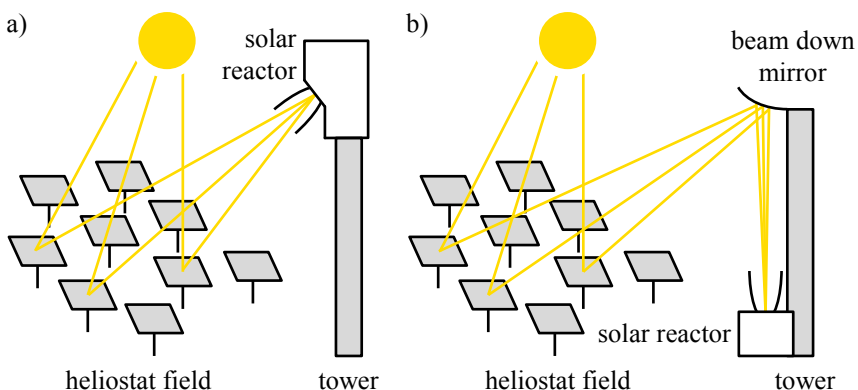


**Figure 2-3:** Solar tower concentrating systems: a) solar reactor on top of tower and b) beam down design with secondary hyperbolic mirror on tower and solar reactor at ground. Adapted from ref. [31].

---

<sup>a</sup> 1 sun = 1 kW/m<sup>2</sup>/DNI, DNI = direct normal irradiation [kW/m<sup>2</sup>]

shape, is installed at the top of the tower redirecting the concentrated solar radiation to the reactor situated on the ground.

Several solar reactor concepts for the gasification of various types of carbonaceous feedstock have been investigated [32, 33] and experimentally demonstrated on a laboratory-scale [34-40]. An overview of the reactor configurations and the feedstocks used is given in Table 2-2. Most concepts exploit a cavity-receiver configuration, in which the concentrated solar radiation passes through an aperture into a cavity to create a high-temperature region within the cavity and supply high-temperature heat to the endothermic reactions. Such configurations are suitable for solar concentrating applications as they approach blackbody absorbers and minimize reradiation losses, while providing a homogeneous temperature distribution through multiple internal reflections and reradiation [3].

As for solar-driven gasification no heat is generated within the gasifier, efficient transfer of the concentrated solar radiation to the reaction site is critical for high productivity and favorable gas-phase selectivity. Directly-irradiated solar gasifiers, where the solar radiation is absorbed directly by the

**Table 2-2:** Existing solar gasifier concepts and feedstocks used.

reference	reactor concept	feedstock
[32-34]	directly irradiated fluidized / packed bed	activated charcoal, flexicoke, PD coke
[36]	directly irradiated packed bed gravity-feed	coal, activated carbon, petroleum coke, walnut shells mixed with coal
[37]	directly and indirectly irradiated fluidized bed	cellulose
[38, 39, 41]	indirectly irradiated entrained-flow	cellulose, beech char
[40]	indirectly irradiated packed-bed	scrap tire chips and powders, sewage and industrial sludge, fluff

feedstock at the reaction site, enable high heat transfer rates. Yet, those also require a transparent window that has to be kept clean during operation. In addition, the window introduces limitations in the operating pressure and the scale-up as the window designs become very complex. [32-37, 42-44]

In indirectly-irradiated reactors the incident solar radiation impinges on the outer wall of an opaque absorber which confines feedstock. The heat is transferred to the inner absorber wall by conduction and from there to the feedstock by convection and radiation. Therefore, the need for a window is eliminated at the expense of having less efficient heat transfer. This imposes even more stringent constraints on the materials of the absorber with regards to its operating temperature, chemical stability, thermal conductivity, radiative absorptance, and resistance to thermal shock. [10, 37-41, 45-47]

A commonly suggested method to achieve the required heat transfer rates in an indirectly-irradiated gasifier is the drop-tube or entrained-flow reactor concept. As shown in Figure 2-4a, the solar radiation is concentrated through an aperture into either a specularly reflecting [38, 46] or absorbing [39, 41, 46, 47] cavity-receiver housing one or more vertical reactor tubes. The reactor tubes absorb the high-flux irradiation and re-radiate the heat to the particles flowing through. However, this reactor concept is suitable only for particles of up to a couple of hundred microns in size for which the radiative heat transfer mode is dominant [48] and the residence time of the order of a second is long enough. Grinding raw biomass to this size range imposes high capital and operating costs that often justify a partial low temperature pyrolysis of the biomass (torrefaction) in order to improve its grindability [49]. At the same time, as the gas is mainly convectively heated by the surface area of the particles that are in a rather dilute flow, this kind of reactor generally does not provide gas temperatures high enough for effective tar and methane cracking and reforming. Alternative reactor concepts such as packed or moving beds allow the use of coarser biomass particles by providing reaction time that is sufficiently long for high carbon conversion. An example is shown in Figure 2-4b. The concentrated solar radiation enters the reactor from the top, is absorbed by an absorber-emitter plate. The plate reradiates onto the packed bed in the lower section of the reactor that is supplied with steam from the bottom.

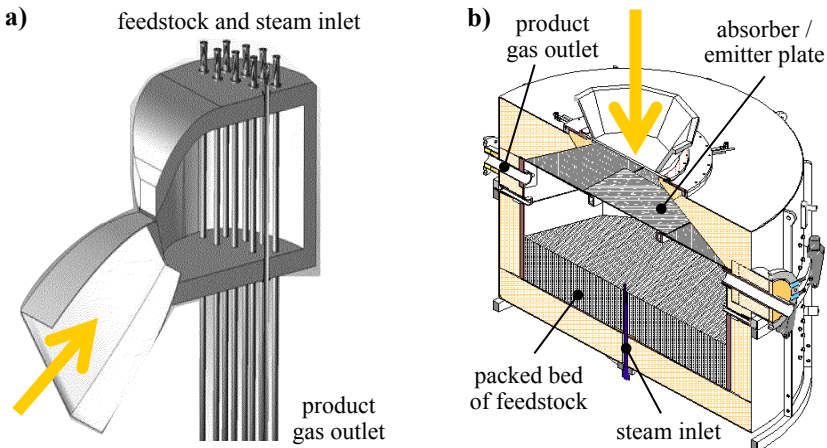


**Figure 2-4:** Solar gasifier concepts: a) tower-mounted drop-tube [41] and b) packed bed for a beam-down configuration [40]. Arrow indicates where the concentrated solar radiation enters the reactor.

Unfortunately, these concepts suffer from significantly impaired overall heat transfer due to high extinction of radiation by the densely packed bed of feedstock and ash [40, 44]. As the heat transfer becomes the limiting factor, large temperature gradients and non-uniform reaction rates adversely impact energy conversion efficiency. The scale-up from pilot to commercial scale is generally driven by providing the heat transfer rates that are necessary for target product rate and quality. Preferably, this is achieved by increasing the number of cavities or, for tubular reactors, by increasing the number of tubes within the cavity to adjust the heat transfer area per throughput [41, 50]. The reasonable scale for commercial solar thermochemical plants is considered to be in the range 10–100 MW of solar power measured at the aperture of the cavity to the reactor [41, 50-53]. This corresponds to a heliostat area of approximately 28,000–287,000 m<sup>2</sup> [53].



# Chapter 3

## Feedstocks<sup>a</sup>

The feedstocks used for the experimentation and the modeling work of this thesis are Brazilian sugarcane bagasse and beech char (Figure 3-1). In this chapter they are briefly described and characterized.

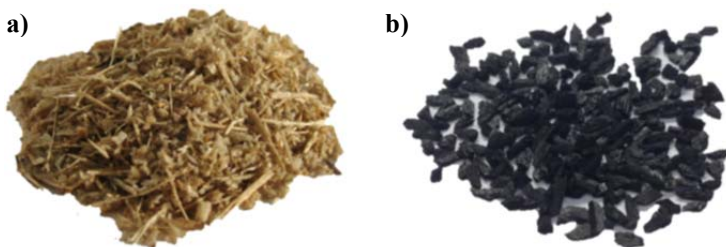


**Figure 3-1:** Biomass feedstocks used: a) Brazilian sugarcane bagasse and b) beech char.

### 3.1 Sugarcane Bagasse

Sugarcane bagasse is a fibrous residue of the sugar or ethanol production from sugarcane. It remains after crushing the sugarcane to extract their juice. Each metric ton of sugarcane processed produces roughly 280 kg of bagasse, with a moisture content in the order of 50%<sub>wt</sub> [54, 55]. On a dry and ash free basis,

---

<sup>a</sup> Material of this chapter has been published in: M. Kruesi, Z. R. Jovanovic, E. C. dos Santos, H. C. Yoon, and A. Steinfeld, "Solar-driven steam-based gasification of sugarcane bagasse in a combined drop-tube and fixed-bed reactor – Thermodynamic, kinetic, and experimental analyses", *Biomass and Bioenergy*, vol. 52, pp. 173-183, 2013.

bagasse is composed of about 50%<sub>wt</sub> cellulose, 25%<sub>wt</sub> hemicellulose, and 25%<sub>wt</sub> lignin [56].

The world production of sugarcane is 1,661 Mt/y, out of which 40% are produced in Brazil alone [57]. The arising bagasse is mainly combusted in boilers at low conversion efficiencies to satisfy the heat and electricity demand of the sugar and alcohol industry. The unused quantity represents about 20% of the total bagasse production [58]. Thus, bagasse is a vast and readily available source of waste biomass.

### 3.2 Beech Char

Beech char or charcoal is a pyrolyzed biomass. As such it has high fixed carbon and low content of volatiles. The beech char was chosen as a model feedstock as it allows studying the steam gasification section of a solar reactor independently from the pyrolysis section because the measurements are not intruded by the presence of pyrolysis products.

### 3.3 Physical and Chemical Properties

The feedstocks were characterized by elemental composition, volatiles, fixed carbon and ash contents, lower heating value, and particle size distribution. The characteristic values are reported in Table 3-1. Before all experiments and analyses the feedstocks were dried for at least 4 h at 378 K. To obtain more homogeneous material properties, the fibrous bagasse was sieved with 1 mm mesh size on a sieve shaker. The beech char particles were ground and sieved to a size of 0.56–1.00 mm.

*Ultimate analysis* – The ultimate analysis to determine the elemental composition was done with CHN-900 for carbon, hydrogen, and nitrogen, RO-478 for oxygen, and CHNS-932 for sulfur (all LECO Corporation, St. Joseph, MI). The unpyrolyzed bagasse has a carbon content of 43%<sub>wt</sub>, a hydrogen content of 6%<sub>wt</sub>, and an oxygen content of 38%<sub>wt</sub>. The contents of nitrogen and

sulfur were 0.41%<sub>wt</sub> and 0.09%<sub>wt</sub>. In contrast, the already pyrolyzed beech char has a very high carbon content of 86%<sub>wt</sub> and low hydrogen and oxygen contents of 2.5%<sub>wt</sub> and 8%<sub>wt</sub>, respectively. Nitrogen and sulfur are in the same range as for the bagasse. On a dry basis and after neglecting the presence of ash, nitrogen and sulfur, the bagasse and the beech char can be represented by the average chemical formulas CH<sub>1.665</sub>O<sub>0.663</sub> and CH<sub>0.349</sub>O<sub>0.072</sub>, respectively.

*Proximate analysis* – The proximate analysis to determine the content of volatiles, fixed carbon, and ash was done in a thermogravimetric balance (Netzsch STA 409 CD). The samples were heated to 393 K in an Ar atmosphere and kept at this temperature for 20 min to finalize the drying process. Then they were heated at 20 K/min to 873 K and held there for 20 min to pyrolyze, attributing the mass loss to the volatiles content. Finally, O<sub>2</sub> was introduced and the temperature was increased a rate of 20 K/min to 1273 K at and kept there for another 20 min to combust the fixed carbon. The remaining

**Table 3-1:** Physical and chemical properties of bagasse and beech char: Ultimate and proximate analyses, heating value and mean particle size.

		bagasse	beech char
carbon (C)	[% <sub>wt</sub> ]	42.51	85.94
hydrogen (H)	[% <sub>wt</sub> ]	5.94	2.50
oxygen (O)	[% <sub>wt</sub> ]	37.54	8.23
nitrogen (N)	[% <sub>wt</sub> ]	0.41	0.92
sulfur (S)	[% <sub>wt</sub> ]	0.09	0.05
H/C = $x$	[mol/mol]	1.665	0.349
O/C = $y$	[mol/mol]	0.663	0.072
volatiles	[% <sub>wt</sub> ]	77.3	17.1*
fixed carbon	[% <sub>wt</sub> ]	12.6	80.8*
ash	[% <sub>wt</sub> ]	10.2	2.1*
LHV	[MJ/kg]	16.50	32.12*
$\bar{d}_p$	[μm]	455	811

\* from ref. [40]

mass was attributed to ash. The bagasse has a volatiles content of around 77%<sub>wt</sub> and a fixed carbon content of 13%<sub>wt</sub>. The beech char has a volatiles content of only 17%<sub>wt</sub> but a fixed carbon content of more than 80%<sub>wt</sub>. The ash content of the bagasse is with 10%<sub>wt</sub> far higher than the one of the beech with only 2%<sub>wt</sub>.

*Heating value* – The lower heating value (LHV) was determined with calorimeter measurements (C7000, IKA-Werke). Due to the higher fixed carbon content in the beech char, the LHV of the beech char (32.12 MJ/kg) is higher than the one of the raw bagasse (16.50 MJ/kg).

*Particle size distribution* – The particle size plays a very important role in the design and performance of a solar reactor as they affect the effective heating rates during pyrolysis and influence the time needed for the gasification step. The particle size distributions were measured using a laser diffraction particle size analyzer (LA-950, HORIBA). Figure 3-2 depicts the particle size distribution for the two feedstocks. The mean particle sizes  $\bar{d}_p$  of bagasse and beech char are 455 and 811  $\mu\text{m}$ , respectively.

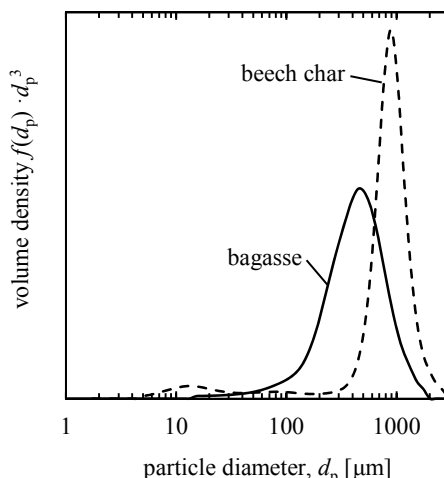


**Figure 3-2:** Particle size distribution functions of ground and sieved bagasse, and beech char analyzed with LA-950 analyzer (HORIBA).

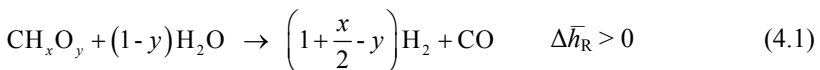
## Chapter 4

# Thermodynamics of Bagasse Gasification<sup>a</sup>

In this chapter, thermodynamic equilibrium compositions are determined for the solar and the autothermal gasification of Brazilian sugarcane bagasse with steam emphasizing the differences in the syngas composition. Moreover, first and second law analyses of the solar and the autothermal gasification are conducted in order to determine the maximum energy and exergy conversion efficiencies, and to identify the major sources of irreversibility.

### 4.1 Equilibrium Considerations

The overall thermochemical conversion can be expressed by the simplified net reaction



where  $x$  and  $y$  are the elemental molar ratios of H/C and O/C in the bagasse, respectively. Equilibrium compositions of the system of Eq. 4.1 with  $\text{CH}_{1.665}\text{O}_{0.663}$  were computed by the direct Gibbs energy minimization technique using the commercial HSC code [59]. Nitrogen and sulfur were neglected as their presence in trace amounts does not affect the equilibrium compositions.

---

<sup>a</sup> Material of this chapter has been published in: M. Kruesi, Z. R. Jovanovic, E. C. dos Santos, H. C. Yoon, and A. Steinfeld, "Solar-driven steam-based gasification of sugarcane bagasse in a combined drop-tube and fixed-bed reactor – Thermodynamic, kinetic, and experimental analyses", *Biomass and Bioenergy*, vol. 52, pp. 173-183, 2013.

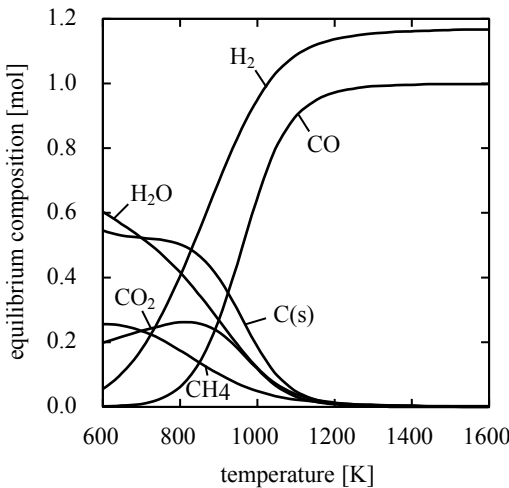


**Figure 4-1:** Equilibrium composition as a function of temperature of the stoichiometric system of Eq. 4.1 for bagasse ( $\text{CH}_{1.665}\text{O}_{0.663}$ ) at 1 bar.

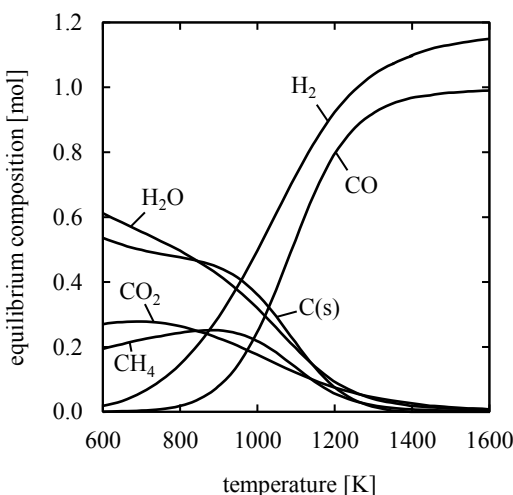


**Figure 4-2:** Equilibrium composition as a function of temperature of the stoichiometric system of Eq. 4.1 for bagasse ( $\text{CH}_{1.665}\text{O}_{0.663}$ ) at 10 bar.

Figure 4-1 shows the equilibrium compositions as a function of temperature at an absolute pressure of 1 bar. Product species with computed mole fractions less than  $10^{-5}$  have been omitted. CH<sub>4</sub>, CO<sub>2</sub>, H<sub>2</sub>O, and C are the thermodynamically favored species at temperatures below 800 K. At temperatures above 1350 K, H<sub>2</sub> and CO are thermodynamically favored, yielding a syngas with a molar H<sub>2</sub>/CO ratio of 1.17. According to Le Châtelier's principle, the thermodynamic equilibrium at elevated pressures favors the production of CH<sub>4</sub>, CO<sub>2</sub>, H<sub>2</sub>O, and C. This can be seen in Figure 4-2 which shows the equilibrium composition at a pressure of 10 bar. As a result, higher temperatures are required to achieve full conversion towards H<sub>2</sub> and CO.

Figure 4-3 shows the reaction enthalpy  $\Delta h_R$  and the lower heating value (LHV) of the product gas as a function of temperature for the system CH<sub>x</sub>O<sub>y</sub> + (1-y) H<sub>2</sub>O of Eq. 4.1 when reactants are fed at 298 K and 1 bar and products are obtained at the indicated temperature having an equilibrium composition as shown in Figure 4-1. The reference enthalpy of the bagasse is determined based on its LHV and its composition.

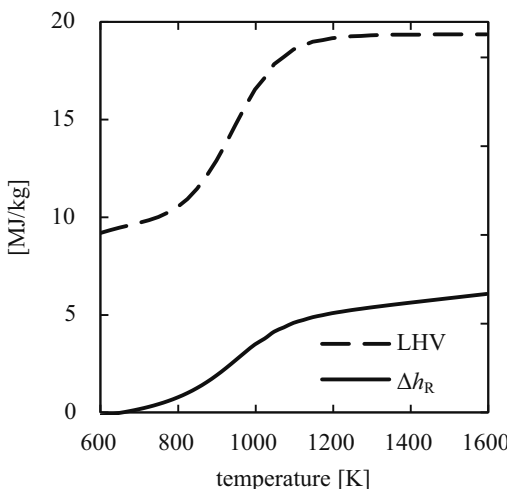
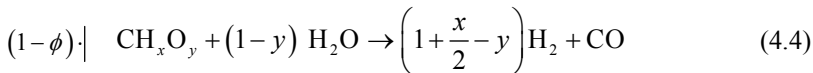
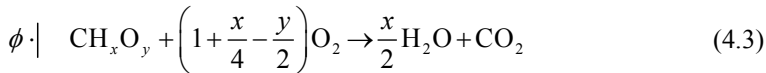


**Figure 4-3:** Reaction enthalpy  $\Delta h_R$  for the system CH<sub>x</sub>O<sub>y</sub> + (1-y) H<sub>2</sub>O (reactants fed at 298 K and 1 bar, products obtained at chemical equilibrium) and LHV of product gas as a function of temperature.

$$\Delta_f \bar{h}_{\text{CH}_x\text{O}_y}^0 = \frac{x}{2} \Delta_f \bar{h}_{\text{H}_2\text{O(gas)}}^0 + \Delta_f \bar{h}_{\text{CO}_2}^0 - \left( 2 + \frac{x-y}{2} \right) \Delta_f \bar{h}_{\text{O}_2}^0 + \text{LHV}_{\text{CH}_x\text{O}_y} M_{\text{CH}_x\text{O}_y} \quad (4.2)$$

The large increase in  $\Delta h_R$  and the LHV in the temperature range 800–1100 K is mainly attributed to the gasification of char and the steam-reforming of methane. At temperatures above 1350 K, the heating value of the product gas is nearly constant since the equilibrium composition approaches complete conversion. The reaction enthalpy increases solely due to the increase in the product temperature. Any increase in temperature above 1350 K is therefore worthwhile only if the reaction rates are accelerated and the thermal losses of the process can be reduced due to shorter residence time of the reactants in a reactor.

In autothermal gasification, a part of the feedstock  $\phi$ , also called equivalence ratio, is combusted (Eq. 4.3) to drive the endothermic gasification (Eq. 4.4), thereby reducing the amount of  $\text{H}_2\text{O}$  that is consumed in a stoichiometric gasification.



Varying the equivalence ratio  $\phi$  results in different adiabatic temperatures and equilibrium compositions as shown in Figure 4-4. For consistency with the first and second law analyses (discussed in Section 4.2), steam and oxygen are introduced at 1100 K and bagasse at 298 K.

The quality of syngas, characterized by the  $\text{H}_2/\text{CO}$  and  $\text{CO}_2/\text{CO}$  molar ratios, is shown in Figure 4-5 for both the solar-driven and autothermal gasification. For the autothermal gasification, significant amounts of  $\text{CO}_2$  originate from the additional oxygen needed for the internal combustion, lowering the ratio of  $\text{H}_2/\text{CO}$  and the calorific value of the syngas. In contrast, the solar-driven gasification produces a syngas of higher quality in terms of

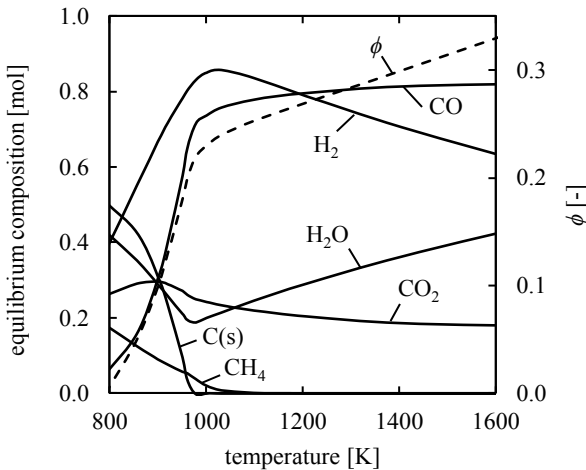


**Figure 4-4:** Equilibrium composition as a function of adiabatic temperature for the system in Eqs. 4.3 and 4.4 with  $0 \leq \phi \leq 0.33$ .

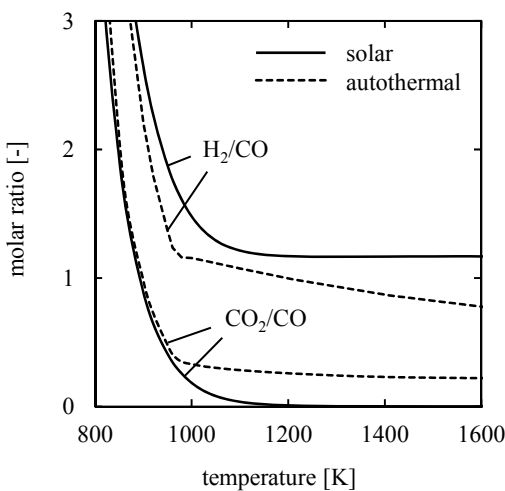


**Figure 4-5:** Molar ratios of H<sub>2</sub>/CO and CO<sub>2</sub>/CO at equilibrium over temperature for solar and autothermal gasification.

higher H<sub>2</sub>/CO and lower CO<sub>2</sub>/CO ratios than those obtained for the autothermal gasification. This reduces the need for water-gas shift reaction and the effort for separating CO<sub>2</sub> when producing Fischer-Tropsch fuels.

## 4.2 1<sup>st</sup> and 2<sup>nd</sup> Law Analyses

First and second law analyses were conducted to assess the performance of the solar and the autothermal gasification of bagasse as well by comparing the energy and exergy efficiencies and the major sources of irreversibility. The two investigated pathways are shown in Figure 4-6. Each includes a gasifier, an adiabatic heat exchanger, and a quencher.

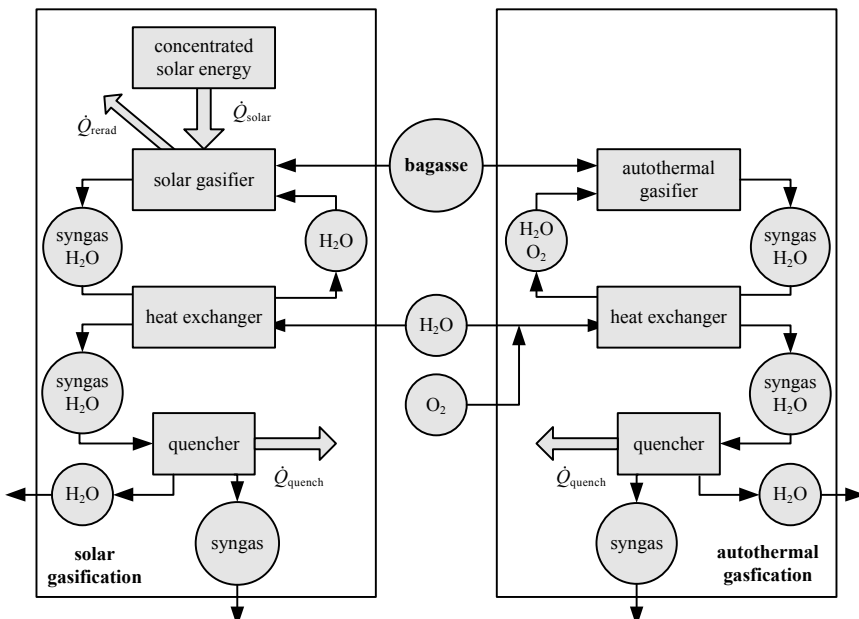


**Figure 4-6:** Flow diagram applied in the first and second law analyses for the solar (left) and autothermal gasification (right).

The gasifiers are considered as fed with H<sub>2</sub>O-, ash-, N-, and S-free bagasse (CH<sub>1.665</sub>O<sub>0.663</sub>) at an ambient temperature  $T_0 = 298$  K and a total pressure  $p_0 = 1$  bar at a biomass flow rate  $\dot{m}_{\text{CH}_x\text{O}_y} = 1$  g/s. Steam or a steam/oxygen mixture enters the solar or the autothermal gasifier, respectively, and is preheated in the heat exchanger to 100 K below  $T_{\text{reactor}}$  by the product gases leaving the reactor in thermodynamic equilibrium at  $T_{\text{reactor}}$ . After passing the heat exchanger, the product gases are quenched to  $T_0$ , rejecting the remaining heat  $\dot{Q}_{\text{quench}}$  to the environment. The thermal energy required for the endothermic solar gasification is provided by an industrial solar concentrating system such as a solar tower with a heliostat field. The solar reactor is of cavity-type configuration. It is assumed to behave like a blackbody ( $\alpha_{\text{eff}} = \varepsilon_{\text{eff}} = 1$ ) with adiabatic walls. Highly concentrated solar radiation  $\dot{Q}_{\text{solar}}$  enters the cavity through a small aperture to minimize reradiation losses  $\dot{Q}_{\text{rerad}}$  [60]. The absorption efficiency of the reactor is defined as [60, 61]

$$\eta_{\text{abs}} = \frac{\dot{Q}_{\text{reactor,net}}}{\dot{Q}_{\text{solar}}} = 1 - \frac{\sigma T_{\text{reactor}}^4}{IC} \quad (4.5)$$

where  $I$  denotes the DNI (direct normal insolation) and  $C$  is the solar concentration ratio. The net energy absorbed by the reactor matches the reaction enthalpy

$$\dot{Q}_{\text{reactor,net}} = \dot{m}_{\text{CH}_x\text{O}_y} \Delta \bar{h}_{\text{R}} \quad (4.6)$$

The exergy destruction and the exergy loss because of absorption and reradiation [62] are given by

$$\dot{Ex}_{\text{desir,abs}} = \dot{Q}_{\text{solar}} \left( 1 - \frac{T_0}{T_{\text{sun}}} \right) - \dot{Q}_{\text{solar}} \left( 1 - \frac{T_0}{T_{\text{reactor}}} \right) \quad (4.7)$$

$$\dot{Ex}_{\text{loss,rerad}} = \dot{Q}_{\text{rerad}} \left( 1 - \frac{T_0}{T_{\text{reactor}}} \right) \quad (4.8)$$

whereas the heat loss due to reradiation is derived from Eq. 4.5 as

$$\dot{Q}_{\text{rad}} = (1 - \eta_{\text{abs}}) \dot{Q}_{\text{solar}} \quad (4.9)$$

The exergy destruction within the reactor, the heat exchanger, and the quenching unit are given by

$$\dot{Ex}_{\text{destr}} = \dot{Q}_{\text{net}} \left( 1 - \frac{T_0}{T_b} \right) + \sum_i \dot{n}_{i,\text{in}} \bar{\varepsilon}_i - \sum_j \dot{n}_{j,\text{out}} \bar{\varepsilon}_j \quad (4.10)$$

where the base temperature  $T_b = T_{\text{reactor}}$  for the reactor and  $T_b = T_0$  for the quencher. For the adiabatic heat exchanger  $\dot{Q}_{\text{net}} = 0$ . The molar exergy of the flow is defined as the exergy of the ideal gas mixture [63], where  $\bar{\varepsilon}_i$  is the sum of the thermo-mechanical and chemical exergy of species  $i$  neglecting kinetic and potential effects [64].

$$\bar{\varepsilon} = \sum_i y_i \bar{\varepsilon}_i + \sum_i RT_0 y_i \ln y_i \quad (4.11)$$

$$\bar{\varepsilon}_i = (\bar{h}_i - \bar{h}_{i,0}) - T_0 (\bar{s}_i - \bar{s}_{i,0}) + \bar{\varepsilon}_{\text{ch},i} \quad (4.12)$$

Chemical exergy, enthalpy, and entropy values are taken from previous studies [65-67]. The chemical exergy of the bagasse is determined by an empirical correlation for solid C-H-O compounds [65].

$$\bar{\varepsilon}_{\text{ch}, \text{CH}_x \text{O}_y} = \beta LHV_{\text{CH}_x \text{O}_y} \quad (4.13)$$

$$\beta = \frac{1.0414 + 0.0177 \frac{H}{C} - 0.3328 \frac{O}{C} \left( 1 + 0.0537 \frac{H}{C} \right)}{1 - 0.4021 \frac{O}{C}} \quad \text{for } \frac{O}{C} \leq 2 \quad (4.14)$$

In the adiabatic autothermal gasifier the heat is supplied by the partial combustion of the feedstock with pure oxygen as described in the previous section. The oxygen is provided by a cryogenic air separation unit (ASU) at an energy expense of 0.245 kWh/kg<sub>O<sub>2</sub></sub> [68, 69]. The determination of the energy and the exergy losses for the autothermal gasifier follows the procedure described for the solar gasifier.

The energy and exergy efficiencies of the gasification processes are defined respectively as

$$\eta = \frac{\dot{m}_{\text{prod}} \text{LHV}_{\text{prod}}}{\dot{m}_{\text{CH}_x\text{O}_y} \text{LHV}_{\text{CH}_x\text{O}_y} + \dot{Q}_{\text{solar}} + \dot{W}_{\text{ASU}}} \quad (4.15)$$

$$\eta_{\text{ex}} = \frac{\sum_i \dot{n}_{i,\text{prod}} \bar{\epsilon}_{i,\text{prod}}}{\sum_j \dot{n}_{j,\text{reac}} \bar{\epsilon}_{j,\text{reac}} + \dot{Q}_{\text{solar}} \left( 1 - \frac{T_0}{T_{\text{reactor}}} \right) + \dot{W}_{\text{ASU}}} \quad (4.16)$$

where  $\dot{W}_{\text{ASU}} = 0$  for the solar process and  $\dot{Q}_{\text{solar}} = 0$  in the autothermal reactor. The upgrade factor  $U$  is defined as the ratio of the energy content of the syngas produced to that of the converted feedstock,

$$U = \frac{\dot{m}_{\text{prod}} \text{LHV}_{\text{prod}}}{\dot{m}_{\text{CH}_x\text{O}_y} \text{LHV}_{\text{CH}_x\text{O}_y}} \quad (4.17)$$

The performance of the solar gasifier is determined by the solar-to-chemical efficiency, defined as

$$\eta_{\text{sol-chem}} = \frac{\sum_i \dot{n}_{i,\text{prod}} \cdot \bar{h}_{i,\text{prod}} - \sum_j \dot{n}_{j,\text{reac}} \cdot \bar{h}_{j,\text{reac}}}{\dot{Q}_{\text{solar}}} \quad (4.18)$$

Table 4-1 shows a summary of the numerical results of the energy and exergy calculations based on the following baseline parameters: inlet biomass mass flow  $\dot{m}_{\text{CH}_x\text{O}_y} = 1 \text{ g/s}$ , total operating pressure  $p_{\text{tot}} = 1 \text{ bar}$ , DNI  $I = 1 \text{ kW/m}^2$ , solar concentration ratio  $C = 2000$ , and sun temperature  $T_{\text{sun}} = 5780 \text{ K}$ . Further, the gasifiers are operated at temperatures ( $T_{\text{reactor}}$ ) of 1350 and 1100 K for the solar and the autothermal case, respectively, yielding equilibrium concentrations of  $\text{CH}_4$  of less than 0.1%<sub>vol</sub> and high heating values of the product gas. Higher temperatures are only favorable if kinetics are accelerated and thermal losses of the reactor (not considered here) can be reduced as a result of the smaller reactor volume needed to perform the gasification.

The energy and exergy efficiencies were found to be  $\eta = 0.92$  and  $\eta_{\text{ex}} = 0.80$  for the solar, and  $\eta = 0.93$  and  $\eta_{\text{ex}} = 0.78$  for the autothermal gasification. The major energy loss occurs in the quencher for both pathways. The largest exergy loss/destruction occurs in the gasifier and accounts for 48% of the total exergy loss/destruction in the solar gasification and 73% of that in the autothermal gasification. In the case of autothermal gasification, around 25% of the feedstock ( $\phi = 0.253$ ) have to be combusted to achieve the desired  $T_{\text{reactor}} =$

**Table 4-1:** Energy and exergy analysis for solar and autothermal gasification. Values for power refer to a biomass feed rate of  $\dot{m}_{\text{CH}_3\text{O}_y} = 1 \text{ g/s}$ .

	units	solar gasification	autothermal gasification
$\dot{Q}_{\text{solar}}$	[kW]	7.12	–
$\dot{Q}_{\text{rerad}}$	[kW]	0.67	–
$\dot{Q}_{\text{reactor, net}}$	[kW]	6.45	0
$\dot{Q}_{\text{quench}}$	[kW]	1.78	1.74
$\dot{W}_{\text{ASU}}$	[kW]	–	0.32
$\eta_{\text{abs}}$	[–]	0.91	–
$\eta$	[–]	0.92	0.93
$\eta_{\text{ex}}$	[–]	0.80	0.78
$\eta_{\text{sol-chem}}$	[–]	0.66	–
$U$	[–]	1.26	0.95
$\dot{Ex}_{\text{destr, absorption}}$	[kW]	1.21	–
$\dot{Ex}_{\text{loss, rerad}}$	[kW]	0.52	–
$\dot{Ex}_{\text{destr, reactor}}$	[kW]	2.82	3.43
$\dot{Ex}_{\text{destr, HEX}}$	[kW]	0.42	0.32
$\dot{Ex}_{\text{destr, quench}}$	[kW]	0.85	0.98
LHV	[MJ/kg]	19.38	13.91
LHV	[MJ/Nm <sup>3</sup> ]	15.68	10.73
H <sub>2</sub>	[% <sub>vol</sub> ]	53.7	45.5
CO	[% <sub>vol</sub> ]	46.1	42.4
CO <sub>2</sub>	[% <sub>vol</sub> ]	0.2	12.0
CH <sub>4</sub>	[% <sub>vol</sub> ]	0.1	0.1

1100 K. This is the reason for the significantly higher exergy destruction in the autothermal gasifier and the resulting lower syngas quality. The solar gasifier, which requires around 7 kW of solar radiation ( $\dot{Q}_{\text{solar}} = 7.12 \text{ kW}$ ) to gasify 1 g/s of bagasse, loses more than 9% of incoming solar radiation through reradiation. To some extent, reradiation losses can be minimized by incorporating secondary non-imaging concentrators (CPC) [70], which increase the solar concentration ratio and reduce the aperture size. The exergy destruction that occurs when absorbing the solar radiation (Eq. 4.7) can be reduced by increasing  $T_{\text{reactor}}$ . Since full conversion is reached at  $T_{\text{reactor}} = 1350 \text{ K}$  (Figure 4-1), this would not affect the syngas quality and only increase the exergy losses elsewhere.

The syngas produced by the solar-driven process shows a more favorable composition with a higher H<sub>2</sub>/CO ratio (1.16 vs. 1.07) and less contamination with CO<sub>2</sub> (0.2%<sub>vol</sub> vs. 12%<sub>vol</sub>). This is also reflected in the LHV's of 19.38 vs. 13.91 MJ/kg and the upgrade factor  $U = 1.26$  vs. 0.98. Thus, the feedstock is solar-upgraded by 26%, chemically storing solar energy with  $\eta_{\text{sol-chem}} = 66\%$ ; in the autothermal case, the energy content of the feedstock is higher than that of the product gas.

This thermodynamic analysis of both routes is verified by performing an energy balance and by evaluating the maximum achievable Carnot efficiency from the total available exergy and from the total solar energy input. The energy balance confirms that

$$\dot{Q}_{\text{solar}} - \dot{Q}_{\text{rerad}} - \dot{Q}_{\text{quench}} = \sum_j \dot{n}_{j,\text{prod}} \cdot \bar{h}_{j,\text{prod}} - \sum_i \dot{n}_{i,\text{reac}} \cdot \bar{h}_{i,\text{reac}} \quad (4.19)$$

The available work is calculated as the sum of the available exergy and the exergy destruction and losses due to irreversibilities in the solar reactor, the heat exchanger, and the quenching unit. Thus,

$$\eta_{\text{max}} = \frac{\sum_j \dot{n}_{j,\text{prod}} \cdot \bar{\varepsilon}_{j,\text{prod}} - \sum_i \dot{n}_{i,\text{reac}} \cdot \bar{\varepsilon}_{i,\text{reac}} + \sum \dot{Ex}_{\text{dest}} + \sum \dot{Ex}_{\text{loss}}}{\dot{Q}_{\text{solar}}} \quad (4.20)$$

This maximum efficiency must be equal to that of a Carnot heat engine operating between  $T_{\text{sun}}$  and  $T_0$ , i.e.

$$\eta_{\max} = \eta_{\text{Carnot}} = 1 - \frac{T_0}{T_{\text{sun}}} = 0.948 \quad (4.21)$$

### 4.3 Conclusions

The thermodynamic equilibrium computations for the solar-driven gasification of a stoichiometric mixture of Brazilian sugarcane bagasse and steam showed an almost full conversion to H<sub>2</sub> and CO at 1 bar and 1350 K. Any further temperature increase is therefore justified only if the reaction rates are accelerated and the thermal losses of the process can be reduced due to shorter residence times of the reactants in the gasifier.

The thermodynamic analysis further indicated a superior syngas quality for the solar-driven over the autothermal gasification. The syngas produced by the solar-driven process showed a more favorable composition with a higher molar H<sub>2</sub>/CO ratio (1.16 vs. 1.07) and less contamination or dilution with CO<sub>2</sub> (0.2%<sub>vol</sub> vs. 12%<sub>vol</sub>).

First and second law analyses of the process showed theoretical upgrade factors of 1.26 vs. 0.95 and heating values of 19.4 vs. 13.9 MJ/kg for the solar and the autothermal gasification routes, respectively. For the autothermal gasification, around 25% of the feedstock needs to be combusted to provide the reaction enthalpy for the endothermic gasification reactions, thereby reducing the amount of H<sub>2</sub>O consumed by a stoichiometric gasification. In contrast, the solar gasification process allows the utilization of all feedstock. Moreover, the feedstock is upgraded by 26% while chemically storing the solar energy with a solar to chemical efficiency of 66%.

The exergy efficiencies for the solar and the autothermal gasification are with 80% and 78% in a similar range. The main difference in the distribution of the exergy losses and destruction is the location where they occur. In the solar

case, 21% occur where the solar energy is absorbed and 48% in the gasifier. In the autothermal case the gasifier contributes to 73% of the total exergy losses and destruction. This is due to the high exergy destruction of the combustion reaction.



# **Chapter 5**

## **Gasification Kinetics of Bagasse<sup>a</sup>**

### **5.1 Thermogravimetric Analysis**

A kinetic analysis of the steam gasification of pyrolyzed Brazilian sugarcane bagasse particles was performed using a thermogravimetric balance (Netzsch STA 409 CD). The thermogravimetric balance, schematically shown in Figure 5-1, consists of an electric furnace in which a sample is placed on a crucible. The crucible is mounted on a thermocouple that is connected to a balance recording the mass change of the sample. A reactive gas mixture of H<sub>2</sub>O and Ar enters the furnace from the bottom through an annulus where it is heated to the furnace temperature. Afterwards, the reactive gas flows downwards past the sample. A small purge flow of Ar not influencing the gas composition at the sample enters the furnace through the balance. The reactive gas mixture is provided by a steam generator unit (Bronkhorst Hitec CEM) that is connected to the furnace via a heated transfer line. The flows of Ar are controlled with flow controllers (Vögtlin Q-FLOW). The flow of H<sub>2</sub>O to the steam generator is controlled by electronic flow controllers (Bronkhorst LIQUI-FLOW).

Due to the strong influence of the pyrolysis conditions on the formation and reactivity of the char, discussed in Section 2.1.1, it is essential that the char used for investigating the kinetics of its gasification with steam is generated

---

<sup>a</sup> Material of this chapter has been published in: M. Kruesi, Z. R. Jovanovic, E. C. dos Santos, H. C. Yoon, and A. Steinfeld, "Solar-driven steam-based gasification of sugarcane bagasse in a combined drop-tube and fixed-bed reactor – Thermodynamic, kinetic, and experimental analyses", *Biomass and Bioenergy*, vol. 52, pp. 173-183, 2013.

under heating rates and temperatures that resemble those in a gasifier. Rapid pyrolysis of the biomass feedstock is preferred for a solar reactor because of the high release of volatiles and the low amounts of char with a high reactivity that are produced. The char samples used in the kinetic analysis were thus rapidly pyrolyzed bagasse particles. The rapid pyrolysis was achieved by entraining raw bagasse particles with Ar into an electrically heated tubular furnace that was preheated to 1373 K. During this rapid pyrolysis step, about 79%<sub>wt</sub> of the feedstock devolatilized yielding bagasse char with an ash content of 64%<sub>wt</sub> as product. An elemental analysis of the bagasse char is presented in Table 5-1.

The kinetic analysis in the thermogravimetric balance was performed under atmospheric pressure and isothermal conditions as done by previous investigators [71, 72]. Bagasse char samples of about 10 mg were preheated to the desired temperature in a non-reactive atmosphere at a heating rate of 30 K/min. The inert atmosphere was established by flowing Ar across the

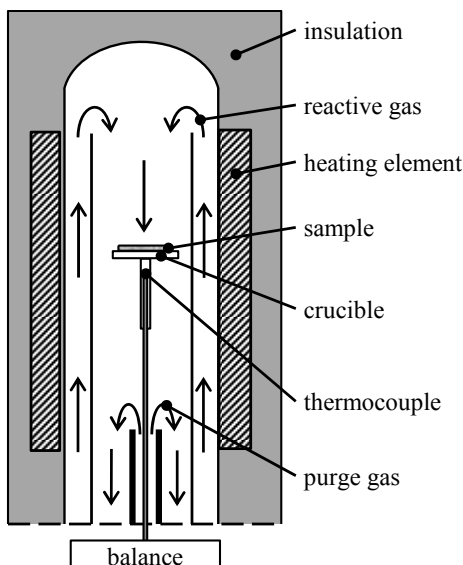


**Figure 5-1:** Thermogravimetric balance configuration.

**Table 5-1:** Elemental composition of raw and rapidly pyrolyzed bagasse particles; C, H, N determined with CHN-900, O with RO-478, and S with CHNS-932 (all LECO Corporation, St. Joseph, MI).

		raw bagasse	bagasse char (rapidly pyrolyzed)
carbon (C)	[% <sub>wt</sub> ]	42.51	29.50
hydrogen (H)	[% <sub>wt</sub> ]	5.94	0.60
oxygen (O)	[% <sub>wt</sub> ]	37.54	5.63
nitrogen (N)	[% <sub>wt</sub> ]	0.41	0.17
sulfur (S)	[% <sub>wt</sub> ]	0.09	0.12
ash (by difference)	[% <sub>wt</sub> ]	13.5	64.0

sample at a flow rate of 0.1 L<sub>N</sub>/min.<sup>b</sup> After temperature equilibration, the atmosphere was switched from Ar to a reactive H<sub>2</sub>O/Ar mixture while keeping the total flow rate across the sample constant (0.1 L<sub>N</sub>/min). The mass loss due to the reaction of the char with the steam was then measured by the balance. To eliminate the effect of buoyancy, a blank run with no sample on the crucible was done for each condition and the recorded mass was subtracted from the sample run.

Based on the measured mass change during the gasification of the sample, the conversion or reaction extent of the sample was defined as

$$X(t) = \frac{m_0 - m(t)}{m_0 - m_f} \quad (5.1)$$

where  $m(t)$ ,  $m_0$  and  $m_f$  are the instantaneous, initial, and final sample mass, respectively.

---

<sup>b</sup> L<sub>N</sub> designates normal liters at 273 K and 1 atm.

## 5.2 Rate Law

### 5.2.1 Reaction Mechanism

Two basic mechanisms, namely the oxygen exchange and the hydrogen inhibition mechanism, have been proposed for the steam gasification of char or carbon given by the overall net reaction [73, 74]



The proposed mechanisms involve several of the following elementary reaction steps occurring at the char surface;



where  $\text{C}\langle *\rangle$  designates an active carbon site, while  $\text{C}\langle \text{O} \rangle$ ,  $\text{C}\langle \text{H}_2 \rangle$ , and  $\text{C}\langle \text{H} \rangle$  are carbon-oxygen or carbon-hydrogen complexes on the char surface, respectively.

## Oxygen Exchange Mechanism

The oxygen exchange mechanism involves the elementary reaction steps R1–R3. After introducing  $\theta_{C(O)}$  and  $\theta_{C(*)}$  as the mole fractions of the surface species covering the effective char surface area,

$$\theta_{C(O)} = N_{C(O)} / N_{\text{tot}} = 1 - \theta_{C(*)} = 1 - N_{C(*)} / N_{\text{tot}} \quad (5.3)$$

Assuming that the ratio of the total number of sites  $N_{\text{tot}}$  to the effective char surface area  $S$  does not change with the progress of reaction, i.e.  $N_{\text{tot}} / S = \text{constant}$ , and relating the reaction rate to the char conversion  $X$  with respect to the initial number of moles of char  $N_{C,0}$  yields

$$r_C = r_{CO} = k_3 \theta_{C(O)} = -\frac{1}{S} \frac{dN_C}{dt} = \frac{N_{C,0}}{S} \frac{dX}{dt} \quad (5.4)$$

Assuming sorption equilibrium, i.e.

$$r_{C(O)} = k_1 p_{H_2O} \left(1 - \theta_{C(O)}\right) - k_2 p_{H_2} \theta_{C(O)} - k_3 \theta_{C(O)} = 0 \quad (5.5)$$

the net gasification rate may be expressed in dependence of the partial pressures of hydrogen  $p_{H_2}$  and steam  $p_{H_2O}$ .

$$r_C = \frac{k_1 p_{H_2O}}{1 + \frac{k_1}{k_3} p_{H_2O} + \frac{k_2}{k_3} p_{H_2}} \quad (5.6)$$

where  $k_i$  are Arrhenius type rate laws of the form

$$k_i = k_{i,0} \exp(-E_A / RT) \quad (5.7)$$

During the thermogravimetric experiments, the gaseous products were constantly swept away from the reaction site, justifying the simplification  $p_{H_2} = 0$ . Thus, the gasification rate depends only on the steam partial pressure and temperature as follows.

$$r_C = \frac{k_1 p_{H_2O}}{1 + (k_1 / k_3) p_{H_2O}} \quad (5.8)$$

### Hydrogen Inhibition Mechanism

The hydrogen inhibition mechanism consists of four steps that are either R1, R3, R4, and R5, or R1, R3, R6, and R7. Similarly to the oxygen mechanism we can derive the net gasification rates as

$$r_C = \frac{k_1 p_{H_2O}}{1 + \frac{k_1}{k_3} p_{H_2O} + \frac{k_4}{k_5} p_{H_2}} \quad (5.9)$$

or

$$r_C = \frac{k_1 p_{H_2O}}{1 + \frac{k_1}{k_3} p_{H_2O} + \frac{k_6}{k_7} p_{H_2}^{0.5}} \quad (5.10)$$

Again, the partial pressure of hydrogen can be set to  $p_{H_2} = 0$  as the product gases are swept away in the TG experiments. The resulting reaction rate is therefore for both cases

$$r_C = \frac{k_1 p_{H_2O}}{1 + (k_1 / k_3) p_{H_2O}} \quad (5.11)$$

This is identical to the net gasification rates derived for the oxygen exchange mechanism (Eq. 5.8).

#### 5.2.2 Surface Area Dependence

With Eq. 5.8 at hand, the only remaining information required to integrate Eq. 5.4 is the dependence of the effective char surface area on the char conversion  $S = S(X)$ . Kimura et al. [75] have pointed out that this relationship depends on the size distribution of solid particles reacting according to the shrinking core model with reaction control [76]. Furthermore, Jovanovic [77] has demonstrated that for wide particle size distributions a linear fit, which was also applied for the gasification of cellulose and lignin [17], may be a reasonable approximation. In the absence of information relative to the

effective size distribution of char particles, the latter was assumed as the initial guess, i.e.

$$S = S_0(1 - X) \quad (5.12)$$

Combining Eqs. 5.4, 5.8, and 5.12, the net gasification rate becomes

$$r_C = \frac{k_1 p_{H_2O}}{1 + (k_1 / k_3) p_{H_2O}} = \frac{N_{C,0}}{S_0} \frac{1}{1 - X} \frac{dX}{dt} \quad (5.13)$$

Because of the presence of ash and unknown ash-carbon structure, the initial effective surface area participating in the gasification per mole of char is unknown. Therefore,  $S_0$ ,  $N_{C,0}$  and  $r_C$  are lumped into apparent reaction rate  $r'_C$  with the apparent rate constants  $k'_1$  and  $k'_3$  as follows

$$r'_C = r_C \frac{S_0}{N_{C,0}} = \frac{k'_1 p_{H_2O}}{1 + (k'_1 / k'_3) p_{H_2O}} = \frac{1}{1 - X} \frac{dX}{dt} \quad (5.14)$$

where

$$k'_i = k_i S_0 / N_{C,0} \quad (5.15)$$

Finally, for constant temperature and steam partial pressure, Eq. 5.14 can be expressed in the integral form as

$$r'_C = \frac{k'_1 p_{H_2O}}{1 + (k'_1 / k'_3) p_{H_2O}} = -\frac{\ln(1 - X)}{t} \quad (5.16)$$

where  $k'_i$  are Arrhenius type rate constants with a pre-exponential factor  $k'_{0,i}$  and an activation energy  $E'_{A,i}$ .

$$k'_i = k'_{0,i} \exp(-E'_{A,i}/RT) \quad (5.17)$$

### 5.2.3 Evaluation of the Rate Constants

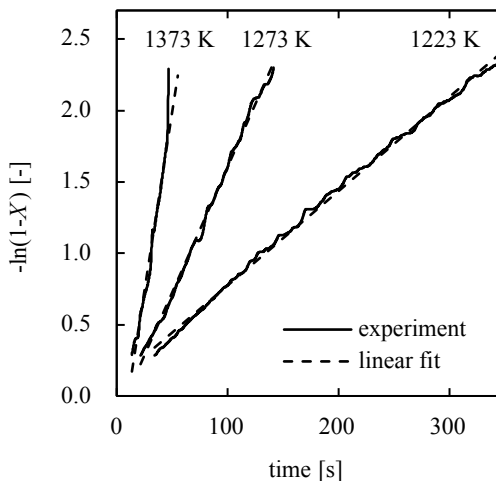
The temperature dependence of the reaction rate was investigated within the range of 1173–1473 K at a steam concentration fixed to 75%<sub>vol</sub>. The effect of the steam concentration was explored at a temperature fixed at 1273 K while varying the steam fraction in the reactive gas mixture between 25%<sub>vol</sub> and 75%<sub>vol</sub>.

Figure 5-3 presents a test of Eq. 5.16 against selected experimental results acquired in a 75%<sub>vol</sub> H<sub>2</sub>O/Ar mixture at three different reaction temperatures. The reasonable linearity allows for extracting the experimental reaction rates as slopes of the fitted straight lines. These were then used to determine the apparent reaction constants  $k'_{0,i}$  and  $E'_{A,i}$ , that are listed in Table 5-2 by least square fitting. The parity plot shown in Figure 5-2 demonstrates the good agreement between model and experimental results over the whole range investigated.

Using the rate law, the residence time required for attaining 90% char conversion with a steam concentration of 75%<sub>vol</sub> at temperatures of 1373 and 1573 K was calculated to be 43 and 16 s, respectively. Operating a solar reactor at temperatures of 1373 K would allow the use of metal alloys as material of construction. This is beneficial due to their better manufacturability, higher thermal shock resistance, and longer lifetimes. Further it has to be kept in mind, that the kinetic analysis was performed at  $p_{H_2} = 0$  thereby neglecting the inhibitive effect of hydrogen. In an actual solar reactor the partial pressure of hydrogen might not be  $p_{H_2} = 0$ , thus slowing down the reaction. Woodruff et al. [78] reported that a partial pressure of  $p_{H_2} = 0.15$  bar results in a reduction of the reaction rate by about 30% and therefore an increase of the required residence time by about 43%.

**Table 5-2:** Apparent kinetic parameters for Eq. 5.16 for the steam gasification of rapidly pyrolyzed bagasse.

	$k'_1$ [1/s-bar]	$k'_3$ [1/s]
$k'_{0,i}$ ( $k'_i$ )	55.8	$4.27 \cdot 10^{11}$
$E'_{A,i}$ [kJ/mol]	73.7	321



**Figure 5-3:** Typical experimental results and linear fits for  $-\ln(1-X)$  vs. time for selected experiments with a 75%<sub>vol</sub> steam/Ar mixture.

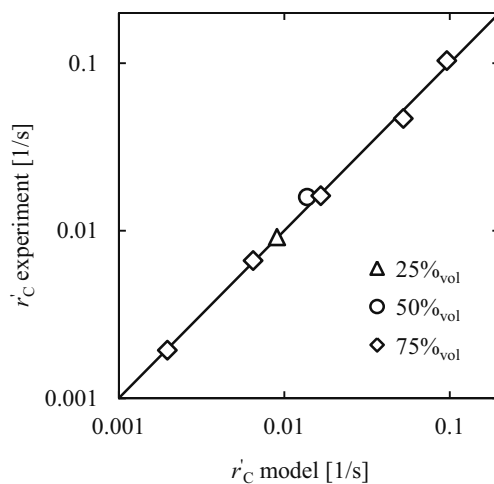


**Figure 5-2:** Apparent carbon conversion rate for the experimental measurements vs. the model for the temperature range 1173–1473 K and 25–75%<sub>vol</sub> steam concentration.

### 5.3 Conclusions

A thermogravimetric analysis of the steam-based gasification of bagasse char was performed in the temperature range of 1173–1473 K and steam concentrations between 25%<sub>vol</sub> and 75%<sub>vol</sub>. The kinetic rate law based on the oxygen exchange mechanism in conjunction with a linear decrease of the effective char surface area with conversion was found to fit the experimental data well.

The required residence times for 90% char conversion at a steam concentration of 75%<sub>vol</sub> and a hydrogen concentration of 0%<sub>vol</sub> at temperatures of 1373 and 1573 K were predicted to be 43 and 16 s, respectively. In an actual solar gasifier, the presence of hydrogen might lead to a moderate increase the required residence time. Therefore, while operating a reactor at 1373 K would expand the option for the material of construction to metal alloys that have much higher shock resistance and better cycle lifetimes than ceramic materials, it will require a reactor concept that provides a residence time in the order of a minute.

## **Chapter 6**

### **Drop-Tube Fixed-Bed Solar Gasifier Concept<sup>a</sup>**

This chapter presents a solar reactor concept that aims at providing pyrolysis and gasification conditions for high carbon conversion of the biomass feedstock into a syngas with low amounts of tar and gaseous hydrocarbons. The proposed laboratory-scale gasifier provides sufficient residence time and temperature for the char conversion and the decomposition of hydrocarbons by combining drop-tube and fixed-bed concepts. Experimental testing was performed with Brazilian sugarcane bagasse particles in an electrically heated furnace with the final aim to supply heat by concentrated solar radiation.

#### **6.1 Gasifier Concept**

As discussed in Section 2.1, the heating rate, gas temperature, and residence time have a strong influence on the release of tar and gases, as well as on the formation and reactivity of the char. Moreover, the kinetic investigation of the feedstock under consideration indicated that a residence time as high as 30–60 s is required for 90% char conversion. The most preferable gasifier concept would thus comprise two zones: a rapid, high-temperature pyrolysis zone yielding low amounts of tar and highly reactive char [17-20] followed by a

---

<sup>a</sup> Material of this chapter has been published in: M. Kruesi, Z. R. Jovanovic, E. C. dos Santos, H. C. Yoon, and A. Steinfeld, "Solar-driven steam-based gasification of sugarcane bagasse in a combined drop-tube and fixed-bed reactor – Thermodynamic, kinetic, and experimental analyses", *Biomass and Bioenergy*, vol. 52, pp. 173-183, 2013.

zone providing sufficient residence time and temperature for the slow char gasification and the decomposition of hydrocarbons.

In the solar reactor concept proposed here, the two zones are realized by incorporating a grate into a drop-tube reactor creating a fixed-bed that increases the residence time of the solids. Such a combined design retains the advantage of the efficient radiative heat transfer to the particles inherent to drop-tube reactors that is needed for fast pyrolysis, while, however, overcoming the drop-tube's residence time and particle size limitations that constrain cracking and reforming of hydrocarbons. Similarly to downdraft gasifiers that yield low amounts of tar, the pyrolysis products pass through hottest zone of the reactor where they are decomposed.

## 6.2 Gasifier Testing in an Electric Furnace

### 6.2.1 Experimental Setup and Procedures

Figure 6-1 shows a schematic of the laboratory-scale reactor used for the experimentation including the primary components and flows. The reactor was assembled from a heat-resistant alumina tube (1200 mm long having an inner diameter of 60 mm and a wall thickness of 5 mm) placed inside an electrical tube furnace (Carbolite) which simulates the conditions of an absorbing cavity-receiver that is heated by concentrated solar radiation. The tube was equipped with a reticulated porous ceramic (RPC) foam (10 ppi, thickness 10 mm, Erbisic, Erbicor S.A.) with a centered hole (diameter 10 mm) serving as a grate at the center of the hot zone.

Dried and sieved bagasse particles (described in Chapter 3) were fed from an Ar-purged hopper positioned above the tube via a calibrated screw feeder and mixed at the top of the tube with N<sub>2</sub>-entrained steam generated with an external evaporator (Bronkhorst). The flow rates of the inlet gases and water into the evaporator were controlled with electronic mass flow controllers (Bronkhorst). The product gas stream was cooled and filtered to remove condensable components and particulate matter and then purified from tar using dichloromethane (DMC) as solvent [79]. The resulting gas composition was

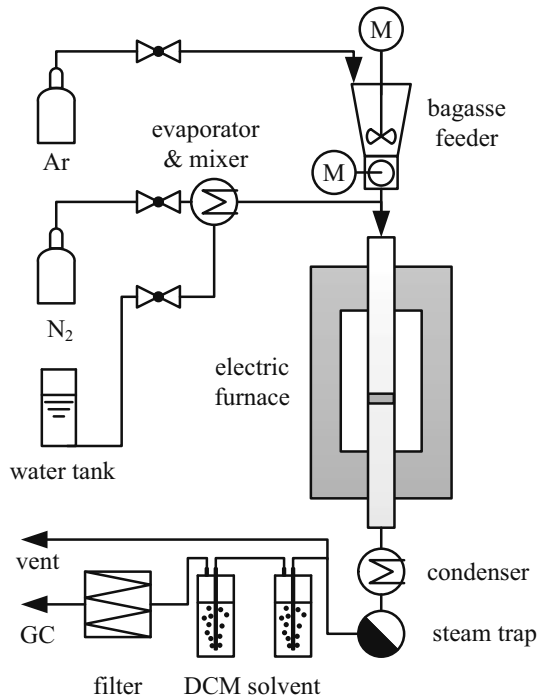


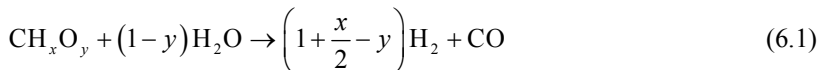
**Figure 6-1:** Schematic of the laboratory-scale biomass gasification apparatus including the primary components and flows.

analyzed by gas chromatography (GC) using a two-channel Varian Micro-GC, equipped with Molsieve-5A and Poraplot-U columns (1/120 Hz sampling frequency) capable of determining concentrations of dry H<sub>2</sub>, N<sub>2</sub>, CO, CH<sub>4</sub>, CO<sub>2</sub>, acetylene (C<sub>2</sub>H<sub>2</sub>), ethylene (C<sub>2</sub>H<sub>4</sub>), and ethane (C<sub>2</sub>H<sub>6</sub>). The nitrogen entraining the steam from the evaporator was used as tracer gas to calculate the total molar flow rate at the outlet of the reactor.

Prior to each experiment, the reactor was first purged with Ar. After reaching a negligible O<sub>2</sub> concentration in the system, the hopper purge Ar and N<sub>2</sub> flow rates were set to 0.5 and 0.1 L<sub>N</sub>/min<sup>b</sup>, respectively. The reactor was

<sup>b</sup> L<sub>N</sub> designates normal liters at 273 K and 1 atm.

then preheated to a desired set-point temperature in the range 1073–1573 K. After equilibration, a steady flow of 17 g/h of steam was established, resulting in an overall steam concentration of around 37%<sub>vol</sub>. At this point, the biomass feed commenced at an average rate of 2.8 g/s·m<sup>2</sup> or 0.48 g/min, leading to a molar steam to biomass ratios ( $\dot{n}_{\text{H}_2\text{O(g)}}/\dot{n}_{\text{CH}_x\text{O}_y}$ ) of about 0.94, corresponding to 2.8 times the stoichiometric amount of steam for the idealized net reaction represented by:



### 6.2.2 Results

The experimental values for composition and the corresponding heating values (LHV), carbon conversions ( $X_C$ ), and upgrade factors ( $U$ ) are reported in Table 6-1. The tabulated mole fractions were calculated considering only molar flow rates of the product gases integrated over 30 min; the flow rates of H<sub>2</sub>O, N<sub>2</sub>, and Ar were not considered. The mole fractions were then used to calculate the mass fractions  $w_k = y_k M_k / \sum(y_k M_k)$  and the reported LHV values as follows:

$$\text{LHV} = \sum w_k \text{ LHV}_k \quad (6.2)$$

The carbon conversion  $X_C$  is defined as the amount of carbon evolved with monitored product gases divided by the amount of carbon fed with bagasse.

$$X_C = m_{\text{C,product}} / m_{\text{C,reactant}} \quad (6.3)$$

For the interpretation of the experimental results, the definition of the upgrade factor  $U$  given in Eq. 4.17 is extended to account for the unconverted feedstock.

$$U = \frac{m_{\text{prod}} \text{ LHV}_{\text{prod}}}{m_{\text{CH}_x\text{O}_y} \text{ LHV}_{\text{CH}_x\text{O}_y} - m_{\text{C,in}} (1 - X_C) \text{ LHV}_{\text{char}}} \quad (6.4)$$

The unconverted feedstock (char) was assumed to be pure carbon with an LHV of 33.5 MJ/kg [80].

**Table 6-1:** Summary of the experimental results obtained for the gasification of bagasse in the electrically heated two-zone reactor

$T$	[K]	1073	1173	1273	1373	1473	1573
$y_{\text{H}_2}$	[%vol]	30	34.7	40.6	47.4	51.2	54.5
$y_{\text{CO}}$	[%vol]	34.3	32.0	33.5	30.7	33.7	34.0
$y_{\text{CH}_4}$	[%vol]	13.4	12.8	9.8	6.6	3.0	0.8
$y_{\text{CO}_2}$	[%vol]	16.7	17.6	15.4	15.1	11.9	10.6
$y_{\text{C}_2\text{H}_2}$	[%vol]	5.0	2.3	0.4	0.1	0.1	0.0
$y_{\text{C}_2\text{H}_4}$	[%vol]	0.3	0.1	0.0	0.0	0.0	0.0
$y_{\text{C}_2\text{H}_6}$	[%vol]	0.3	0.5	0.2	0.1	0.0	0.0
$y_{\text{H}_2}/y_{\text{CO}}$	[-]	0.88	1.08	1.21	1.55	1.52	1.6
$y_{\text{CO}}/y_{\text{CO}_2}$	[-]	2.05	1.82	2.17	2.03	2.83	3.2
LHV	[MJ/kg]	16.93	15.95	15.34	15.29	15.55	15.69
LHV	[MJ/m <sup>3</sup> ]	16.09	14.44	12.84	11.81	11.27	10.83
$X_{\text{C}}$	[-]	0.65	0.61	0.67	0.76	0.82	0.84
$U$	[-]	0.95	0.94	0.96	1.03	1.08	1.12

Figure 6-2 shows the experimentally measured mole fractions of the product gases as well as the equilibrium composition as a function of temperature. The production of H<sub>2</sub> gradually increased with temperature approaching the concentration predicted by equilibrium (Figure 4-1). The CO mole fraction remained relatively constant over the whole temperature range investigated. At 1073 K it was higher than that predicted by equilibrium. For all other experimental conditions, CO levels were over-predicted. The measured CO<sub>2</sub> concentrations decreased with an increase in temperature but were significantly higher than those predicted by equilibrium. Although the presence of CH<sub>4</sub> is not thermodynamically favored at above 1200 K, it was still observed (~1%vol) at temperatures as high as 1573 K. C<sub>2</sub>-gases, especially ethylene (C<sub>2</sub>H<sub>4</sub>) were detected in small amounts (> 0.1%vol) up to temperatures of about 1273 K. Increased temperatures yielded H<sub>2</sub>/CO ratios of up to 1.60 and CO<sub>2</sub>/CO ratios as low as 0.31.

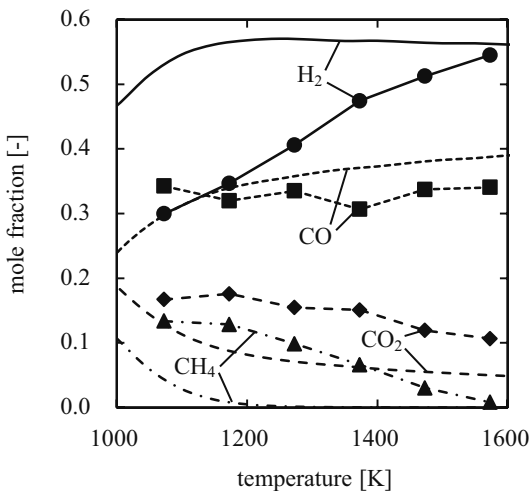


**Figure 6-2:** Relative mole fractions (dry,  $N_2$  and Ar free basis) of the product gases and the equilibrium composition (lines without markers)

The carbon conversion  $X_C$  increased with temperature from 65% to 84%. The reasons for the generally low carbon conversions may be partially attributed to the formation of tar which was observed mainly in the experiments at 1073 and 1173 K. Further, inadequate solids retention performance of the ceramic grate led to particles penetrating through the grate and ending up at the bottom of the reactor. Poor heat transfer to the packed bed of char and slow reaction kinetics at 1073 and 1173 K led also to an accumulation of partially reacted particle on the RPC. This could also be observed by a non-steady product gas composition. In the experiments from 1273 to 1573 K a steady product gas composition was observed.

All these findings imply that neither gas nor solids spent sufficient time at temperatures required for target conversion which is to be addressed by an improved version of this hybrid reactor concept, the solids retention grate in particular.

Upgrade factors were found to increase with temperature and a maximum of 112% could be achieved. This increase is partly due to the increased carbon conversion and partly due to the different composition. The heating values of

the syngas (LHV) were 15.3–16.9 MJ/kg or 10.8–16.1 MJ/Nm<sup>3</sup>. Due to the decrease of CH<sub>4</sub> and C<sub>2</sub>-gases with temperature, the heating value per volume was significantly reduced. The heating values found are significantly higher values than those generally obtained in conventional autothermal gasifiers. For example, the fluidized-bed air gasifier by Gómez et al. [7] delivers syngas with 3.3–5.1 MJ/Nm<sup>3</sup> at a cold gas efficiency of 29.2%, whereas the air blown cyclone gasifier by Gabra et al. [8] produces product gas with 2.8–4.5 MJ/Nm<sup>3</sup>.

Ash melting was observed at above 1473 K, which is consistent with ash fusion tests (ASTM, oxidizing atmosphere) of Indian [81] and Hawaiian bagasse [54] where initial deformation temperatures of 1473 and 1510 K were observed. For continuous operation it is thus necessary to stay below the ash melting temperature of about 1473 K.

### 6.3 Conclusions

An allothermal gasifier configuration based on a combination of drop-tube and fixed-bed concepts was proposed. The two-zone concept aims to provide pyrolysis and gasification conditions yielding high carbon conversion into syngas and low amounts of tar and gaseous hydrocarbons. In the upper drop-tube zone, high radiative heat flux to the dispersed particles induces their fast pyrolysis. In the lower zone, a fixed bed provides sufficient residence time and temperature for the char gasification and the decomposition of the hydrocarbons released during the pyrolysis.

A lab-scale prototype reactor was tested with bagasse particles at a biomass feed rate of 2.8 g/s·m<sup>2</sup> in the temperature range of 1073–1573 K. The reactor was exposed to infrared radiation from an electric furnace simulating the conditions present in an absorbing solar cavity receiver. The concentrations of the gaseous species were approaching the thermodynamic equilibrium as the reactor temperature was increased, i.e. H<sub>2</sub> concentrations went up whereas amounts of CO<sub>2</sub>, CH<sub>4</sub>, and C<sub>2</sub>-hydrocarbons decreased. Although the presence of CH<sub>4</sub> is not thermodynamically favored at above 1200 K, it was observed in significant amounts over the whole temperature range investigated. The syngas

produced had molar H<sub>2</sub>/CO ratios of up to 1.6 and CO<sub>2</sub>/CO ratios as low as 0.31. The lower heating values were from 15.3 to 16.9 MJ/kg. The carbon conversion of these preliminary experiments stayed behind the expectations, which implied that further development in terms of particle retention and heat transfer was necessary. Further, the observed ash melting occurring at temperatures above around 1473 K gave an upper limit for the operating temperature of this concept.

However, it could be confirmed that an upgrade factor of greater than 1 is achievable and that syngas yields per unit feedstock and heating values are significantly higher than those typically obtained in conventional gasifiers, supporting the potential benefits of solar-driven gasification over conventional autothermal gasification.

## **Chapter 7**

### **Drop-Tube Trickle-Bed Solar-Driven Gasifier<sup>a</sup>**

The externally heated gasifier concept presented in the previous chapter was further improved to deliver higher carbon conversion and a better decomposition of the gaseous hydrocarbons. The improved gasifier concept comprises a drop-tube zone for fast pyrolysis and a trickle bed for the rate limiting char gasification and the decomposition of the pyrolysis products. The trickle bed utilizes a structured packing to control the overall porosity of the gasification zone in order to increase the residence time of the char particles while still allowing the radiation to penetrate through. The structure packing thus enhances the heat transfer to both the particle and the gas phase. The drop-tube trickle-bed concept was tested in a solar reactor that was designed and built for operation at ETH's high flux solar simulator. Its performance was experimentally assessed with Brazilian sugarcane bagasse particles and compared to the performance of the drop-tube configuration.

#### **7.1 Gasifier Concept**

The solar-driven gasifier developed is shown in Figure 7-1. It is based on a vertical tubular reactor situated within a cavity-receiver in order to minimize reradiation losses and provide a homogeneous temperature distribution [3]. The tubular reactor comprises two zones (see inlay Figure 7-1): an upper drop-tube

---

<sup>a</sup> Material of this chapter has been published in: M. Kruesi, Z. R. Jovanovic, and A. Steinfeld, "A two-zone solar-driven gasifier concept: Reactor design and experimental evaluation with bagasse particles", *Fuel*, vol. 117, Part A, pp. 680-687, 2014.

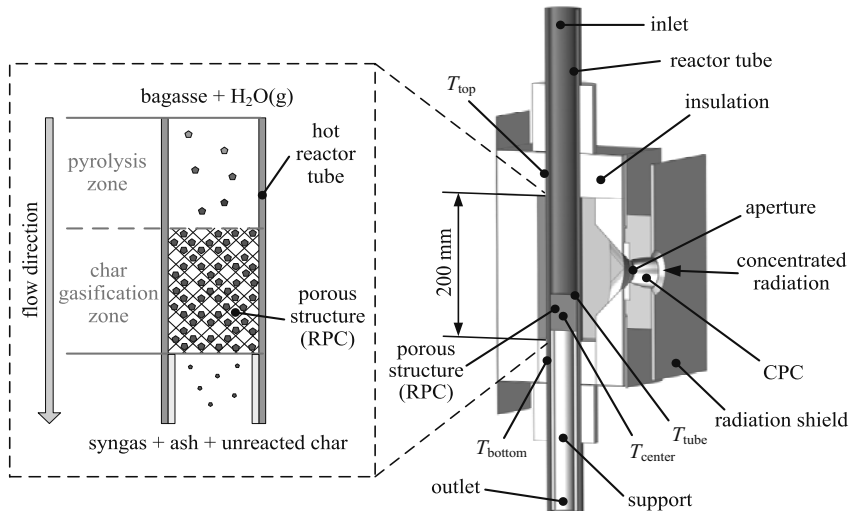


**Figure 7-1:** Schematic of the solar cavity-receiver/reactor configuration with thermocouple locations and blown up detail of the reactor tube showing the fast pyrolysis drop-tube zone and the trickle-bed char gasification zone (RPC = reticulate porous ceramic, CPC = compound parabolic concentrator).

pyrolysis zone and a lower trickle-bed char gasification zone consisting of a structure packing. Bagasse particles and steam are both introduced from the top. The raw bagasse particles are rapidly heated in the upper zone by infrared radiation from the tube wall to undergo fast pyrolysis. This zone provides sufficient residence time to ensure that the particles reaching the trickle bed are not sticky and prone to clogging the structure packing.

The structure packing, depicted in Figure 7-2, is a reticulate porous ceramic (RPC) foam. The pyrolyzed particles trickle through the RPC and undergo gasification with concurrently flowing steam. In comparison to the commonly used packings, such as spheres, Raschig rings, Pall rings, cylindrical screens, or regularly stacked packings [82-87], the RPC has a higher degree of solid connectivity and therefore higher effective thermal conductivity at the same porosity. This is of a great importance as the heat is provided externally.



**Figure 7-2:** Structure packing made of 10 ppi SiSiC reticulate porous ceramic (RPC) foam installed in the solar gasifier. Image from [88].

Moreover, the structure is less optically dense than a packed or a moving bed hence the radiation penetrates deeper. Therefore, by combining conductive and radiative heat-transfer modes, the structure is expected to enhance heat transfer to both gas [89] and solid phases. Finally, by providing a resistance to the flow of solids the structure not only increases the mean residence time of the trickling particles but it also aids their radial dispersion. All these enhancements are expected to provide a more homogeneous radial temperature distribution and decrease the temperature difference between the gas and the solids, thereby increasing reaction yields.

By transporting gas and solids downwards as done in downdraft gasifiers, the tar and gases evolved during the pyrolysis pass through the hottest zone of the reactor where they decompose via cracking and reforming reactions to H<sub>2</sub>, CO, CO<sub>2</sub>, lighter hydrocarbons, and coke.

Together with the potential advantages mentioned above, the concept proposed here introduces some limitations that need to be recognized. Although high temperatures are desirable for efficient heat transfer to gas and solids resulting in high reaction rates, the operating temperature of the trickle zone is

limited by the ash melting temperature of the feedstock. In addition, the throughput of the feedstock depends on how well the particle loading and residence time within the structured packing can be controlled.

## 7.2 Gasifier Testing on a High Flux Solar Simulator

### 7.2.1 Experimental Setup

The solar reactor (Figure 7-1) was made of a heat-resistant, well conducting (30 W/m·K at 1500 K) pressureless-sintered silicon carbide tube (Hexoloy SE SiC, Saint Gobain, L 700 mm, ID 41 mm, OD 51 mm) which was placed in a cavity (200 × 86 × 86 mm) made of a 60 mm thick (40 mm at the front) alumina/silica based insulation (65%  $\text{Al}_2\text{O}_3$ , 34%  $\text{SiO}_2$ , Insulform 1600). The insulation was fastened by a stainless steel case surrounding it. The cavity has a 30 mm-diameter aperture for the access of concentrated solar radiation. The reactor tube was placed slightly towards the back of the cavity to reduce thermal stress on the tube and minimize reradiation losses due to hotspots [46]. A 3-dimensional, water-cooled compound parabolic concentrator (CPC) [90] was mounted as a secondary concentrator at the reactor aperture to boost the concentration ratio, thereby allowing a smaller aperture size and thus further reducing reradiation losses. The CPC was made of polished aluminum and designed for a half acceptance angle of 45° with an exit diameter of 30 mm. It was truncated to a height of 32.2 mm resulting in an inlet diameter of 42.3 mm and a concentration ratio close to 2. To prevent overheating of the outer surface of the assembly by spilled radiation, a water-cooled shield (300 × 300 mm) was mounted around the CPC. The system was designed for 1.5 kW<sub>th</sub> solar radiative input power and operation at ambient pressure and temperatures up to 1850 K.

Figure 7-3 presents an overview of the experimental setup including the solar gasifier and auxiliary components. Bagasse particles were introduced by an Ar-purged drum feeder positioned above the reactor tube. N<sub>2</sub> and steam generated with an external evaporator (Bronkhorst) were injected through annularly distributed inlets positioned just below the feeder. The flow rates of the inlet gases and the water into the evaporator were controlled with electronic

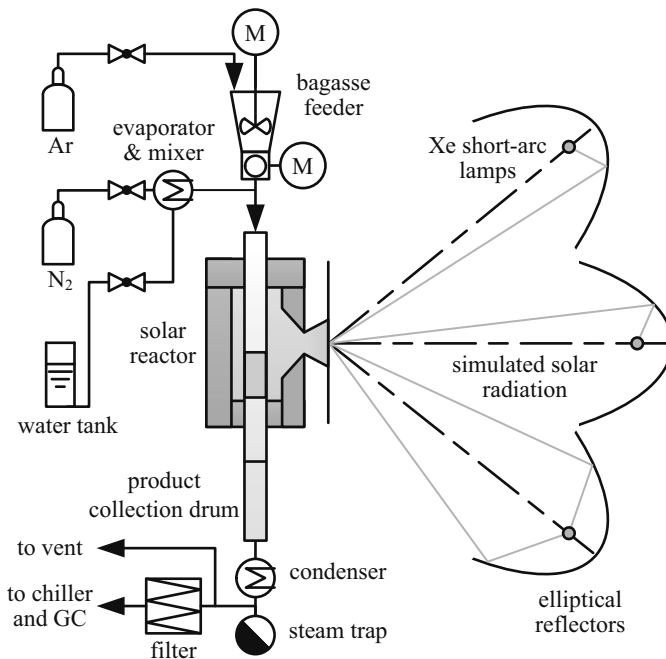


**Figure 7-3:** Schematic of the solar-driven biomass gasifier, including the high-flux solar simulator and the auxiliary components and flows.

mass flow controllers (Bronkhorst). The porous structure creating the trickle bed is shown in Figure 7-2. It was made of a 10 ppi (pores per inch) SiSiC (silicon infiltrated silicon carbide) reticulate porous ceramic foam (RPC, porosity > 87%), which was placed in the hot zone of the reactor tube. The RPC was supported by an alumina tube (Alsint 99.7, Haldenwanger, inner diameter 30 mm, outer diameter 38 mm). The temperatures of the cavity and of the reactor tube were measured with K-type thermocouples placed at multiple axial locations inside the assembly ( $T_{\text{inlet}}$ ,  $T_{\text{top}}$ ,  $T_{\text{tube}}$ ,  $T_{\text{bottom}}$ ,  $T_{\text{outlet}}$ ). One thermocouple,  $T_{\text{center}}$ , was inserted into the RPC with its tip at the centerline, 20 mm above the bottom of the RPC.

Ash and unreacted char were collected in the product collection drum located below the reactor just before a condenser and a steam trap. A slip-stream of the product gas was withdrawn after the condenser and analyzed by

gas chromatography (GC) after being filtered and chilled to remove particulate matter and condensable components. The two-channel Varian Micro-GC equipped with a Molsieve-5A and a Poraplot-U column (1/120 Hz sampling frequency) was calibrated to determine the concentrations of H<sub>2</sub>, N<sub>2</sub>, CO, CH<sub>4</sub>, CO<sub>2</sub>, C<sub>2</sub>H<sub>2</sub>, C<sub>2</sub>H<sub>4</sub>, and C<sub>2</sub>H<sub>6</sub>. A known flow rate of N<sub>2</sub> introduced with the steam was used as tracer gas to calculate the total molar flow rate of the product gas.

The experiments were carried out at the high-flux solar simulator (HFSS) of ETH Zürich. The HFSS is equipped with seven 6 kW<sub>el</sub> high-pressure Xe arcs close-coupled to truncated elliptical specular reflectors [91]. It is capable of delivering continuous thermal radiative power with a peak flux of up to 4500 kW/m<sup>2</sup> and a mean flux of 3620 kW/m<sup>2</sup> on a 30 mm aperture diameter. Thus, the solar reactor was tested under comparable heat-transfer characteristics of highly concentrating solar systems, such as solar dishes and solar towers. Radiative flux intensities were adjustable by the number of Xe arcs in operation, their power, and the position of the reactor aperture relative to the focal plane. The radiative power input at the reactor aperture ( $\dot{Q}_{\text{solar}}$ ) was determined optically with a calibrated CCD camera and verified by calorimetric measurements at the CPC outlet.

### 7.2.2 Experimental Procedure

The power input and the temperature traces recorded during a typical experiment are shown in Figure 7-4. At the beginning of all the experiments but one, the nominal Ar and N<sub>2</sub> flow rates were set to 0.5 L<sub>N</sub>/min: in the reference experiment with pure pyrolysis (no steam injection) the nominal flow rates of Ar and N<sub>2</sub> were set to 0.5 L<sub>N</sub>/min<sup>b</sup> and 2.2 L<sub>N</sub>/min, respectively. In order to achieve rapid heating, up to 5 arcs of the HFSS were then turned on simultaneously to irradiate the reactor at high power levels (1.65 kW<sub>th</sub>, 2333 kW/m<sup>2</sup>). After approximately 30 min, the input power was reduced to the levels ranging between 1.147 and 1.195 kW<sub>th</sub> (1622–1690 kW/m<sup>2</sup>) to

---

<sup>b</sup> L<sub>N</sub> designates normal liters at 273 K and 1 atm.

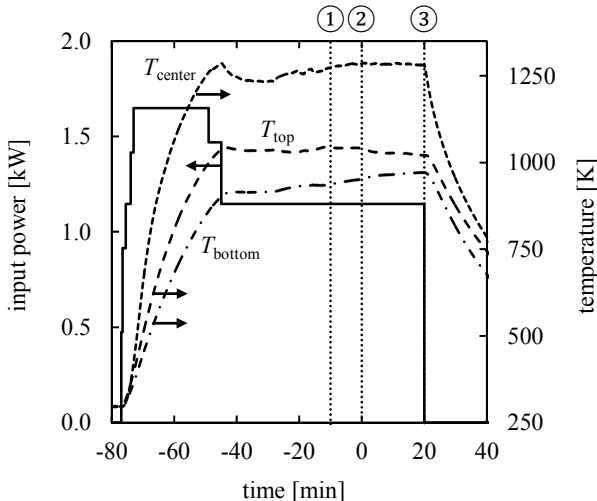
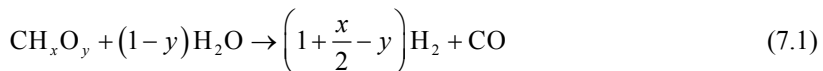


**Figure 7-4:** Input power ( $\dot{Q}_{\text{solar}}$ ) and reactor temperatures during a typical experiment: ① steam on, ② biomass feed on, and ③ biomass feed off.

equilibrate the reactor in a steady-state with the resulting temperature inside the RPC ( $T_{\text{center}}$ ) settling within 1256–1362 K range. The maximum temperature at the top of the RPC at the tube ( $T_{\text{tube}}$ ) was kept below 1428 K to avoid ash slagging that has been observed at temperatures above 1473 K [54, 81, 92]. After the thermal equilibration of the system, steam preheated to about 560 K was injected at a steady rate of 81.6 g/h resulting in a nominal inlet steam concentration of 62.9%<sub>vol</sub>. The injection of steam ① was reflected by a temperature drop in the upper part of the reactor ( $T_{\text{top}}$ ) and an increase towards the bottom ( $T_{\text{bottom}}$ ). After reaching another steady state, the biomass feed commenced ② at feeding rates between 61 and 94 g/h leading to molar steam to biomass ratios ( $n_{\text{H}_2\text{O(g)}}/n_{\text{CH}_3\text{O}_y}$ ) of 1.37–2.09. This corresponds to 2.06–3.15 times the stoichiometric amount of steam for the idealized net reaction represented by:



After another 20 min, biomass feed, steam flow, and irradiation were all turned off and the reactor was cooled down ③. Temporal gas composition, temperature, and pressure data were acquired during the course of the experiment. In addition, char samples were collected after the experiments and analyzed for their elemental composition (CHN-900, LECO Corporation, St. Joseph, MI).

### 7.3 Results and Discussion

Figure 7-5 shows the molar flow rates of the product gases as a function of time during a typical experimental run. A slight increase in H<sub>2</sub> and CO can be observed immediately after the commencement of steam ①. This has been attributed to the gasification of the carbon residue in the RPC originating from previous experiments. As the step changes in product flow rates could be correlated with turning the biomass feed on ② and off ③, the observed

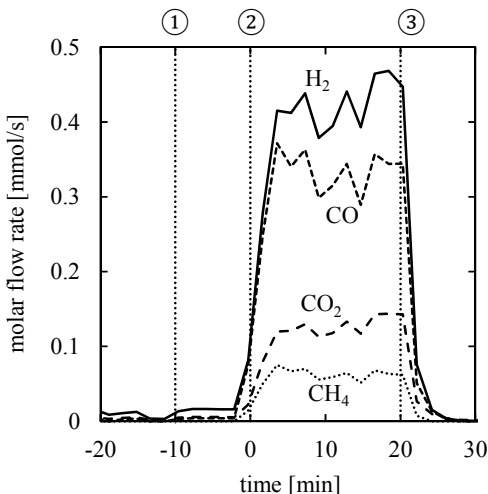


**Figure 7-5:** Molar flow rates of product gases as a function of time during a typical experimental run: ① steam on, ② biomass feed on, and ③ biomass feed off.

fluctuations in the data shown in Figure 7-5 reflect the intermittent feed rate. In addition, the data indicated an increase in the production of H<sub>2</sub> and CO<sub>2</sub> and a decrease in the production of CO, CH<sub>4</sub> and C<sub>2</sub>H<sub>4</sub> with time. This could be explained by two factors: (1) the gradual increase in the temperature at the bottom of the cavity as indicated by Figure 7-4 and (2) a suspected buildup of char within the RPC. As a result of the char buildup, more syngas was produced within the RPC that then underwent the water-gas shift and hydrocarbon cracking and reforming reactions favored by a higher temperature at the bottom of the cavity.

Experiments were carried out with different system configurations as summarized in Table 7-1. Two-zone experimental sets A1-A3 and B1-B3 were performed with RPCs that were 50 and 100 mm tall, respectively. As reference runs simulating the drop-tube concept alone, free-fall pure pyrolysis (PP) and free-fall steam-based gasification (SG) experiments were performed without

**Table 7-1:** Summary of the experimental results (A = 50 mm tall RPC, B = 100 mm tall RPC, PP = free-fall pure pyrolysis, SG = free-fall steam-based gasification, all values are on a H<sub>2</sub>O, N<sub>2</sub> and Ar free basis).

	A1	A2	A3	B1	B2	B3	SG	PP
$\bar{T}_{\text{center}}$ [K]	1344	1359	1362	1303	1284	1285	1343	1338
$\bar{T}_{\text{top}}$ [K]	1098	1105	1108	1045	1027	1028	1080	1110
$\bar{T}_{\text{bottom}}$ [K]	1024	1037	1040	980	965	980	1068	1053
$y_{\text{H}_2}$ [%vol]	45.8	46.0	46.5	45.0	43.7	45.0	37.2	35.1
$y_{\text{CO}}$ [%vol]	33.8	34.7	34.1	34.8	34.8	34.4	39.9	46.5
$y_{\text{CH}_4}$ [%vol]	5.9	5.7	5.4	6.2	6.6	6.3	8.7	7.0
$y_{\text{CO}_2}$ [%vol]	13.2	12.5	13.0	12.8	13.2	13.2	10.9	6.2
$y_{\text{C}_2\text{H}_2}$ [%vol]	1.0	0.8	0.8	0.8	1.1	0.6	2.0	3.7
$y_{\text{C}_2\text{H}_4}$ [%vol]	0.4	0.3	0.3	0.4	0.6	0.5	1.1	1.5
$y_{\text{C}_2\text{H}_6}$ [%vol]	0.0	0.0	0.0	0.0	0.0	0.0	0.0	0.0
LHV [MJ/kg]	15.9	15.9	15.7	15.9	15.9	15.8	17.0	18.5
$U$ [-]	1.06	1.04	1.06	1.05	1.04	1.05	0.99	1.00
$X_{\text{C}}$ [-]	0.89	0.80	0.90	0.89	0.90	0.88	0.69	0.64

any RPC in the system. Furthermore, the experiments were performed at two levels of  $T_{center}$ :  $\sim 1350$  K for set A, SG, and PP, and  $\sim 1290$  K for set B. The observed temperature variations within experimental sets A and B are the result of the physical limitations to strictly control the power input to the solar reactor.

The tabulated mole fractions were calculated considering only molar flow rates of the product gases integrated over the course of an experiment; the flow rates of H<sub>2</sub>O, N<sub>2</sub>, and Ar were not considered. LHV, upgrade factor ( $U$ ), and carbon conversion ( $X_C$ ) were calculated as defined in Eqs. 6.2–6.4.

The carbon mass balance showed that between 89% and 98% of the total carbon fed into the system could be accounted for by the gas phase evolved over the course of an experiment and the solids recovered from the RPC and the product collection drum. The remainder was attributed to deposits on the tube wall, carryover of fine particles or tar, and the overall measurement error. The fraction of the carbon retained within the RPCs was less than 2.3% and 5.3% for the configurations A and B, respectively.

The statistical significance of the differences between the responses of the investigated configurations has been assessed as follows:

- (a) The responses of configurations A and B were compared using two-sample *t*-tests at a significance level of 5% (MATLAB, The MathWorks, Inc.). The variances of the unpaired samples were considered to be equal as confirmed by two-sided F-tests at a 95% confidence level.
- (b) The single responses of configurations SG and PP were compared to the responses of configurations A and B by single-sided Grubb's outlier tests [93] at a 5% confidence level. These tests were used to decide with 95% confidence if the responses of configurations SG and PP do not belong to the same normal distributions as the corresponding responses of sets A1–A3 and B1–B3.

The results of the statistical analysis are summarized in Table 7-2. For a comparison X vs. Y, “>” or “<” designate statistically significant higher or

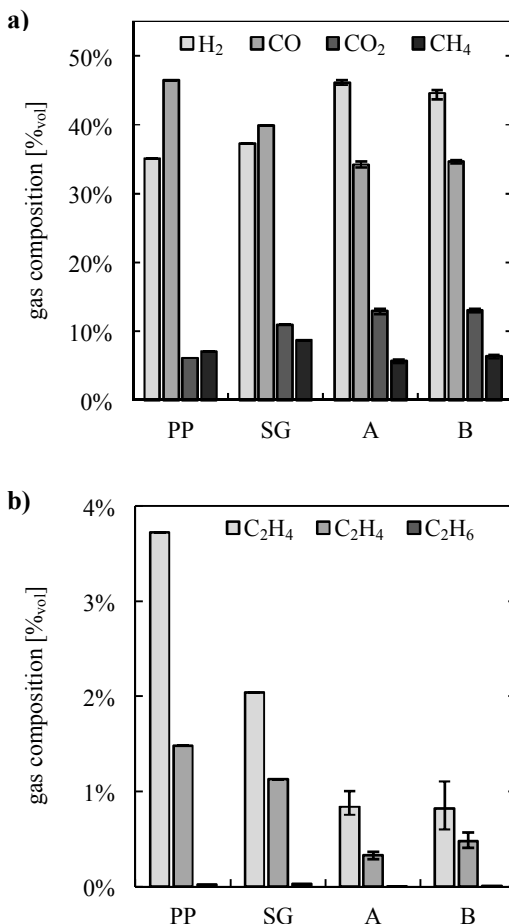
lower response value for configuration X; “~” designates no statistically significant difference.

Figure 7-6 presents a comparison of the gas compositions measured with the different system configurations. The average gas mole fractions calculated for the experiments A1–A3 and B1–B3 correspond to H<sub>2</sub>/CO ratios of 1.35 and 1.29, respectively, and the same CO<sub>2</sub>/CO ratios of 0.38. Although the temperatures ( $\bar{T}_{\text{center}}$ ,  $\bar{T}_{\text{top}}$ ,  $\bar{T}_{\text{bottom}}$ ) in set B were on average 59–70 K lower than in set A, according to Table 7-2 only the mole fractions of H<sub>2</sub> and CH<sub>4</sub> were found to be statistically different.

As shown in Table 7-2, the comparison of the two-zone configurations A and B to the free-fall pure pyrolysis (PP) indicates a significant decrease in CO, C<sub>2</sub>H<sub>2</sub>, and C<sub>2</sub>H<sub>4</sub> as well as an increase in H<sub>2</sub> and CO<sub>2</sub>. The comparison to the free-fall steam-based gasification experiment (SG) indicated the following:

- The amounts of CO and CH<sub>4</sub> obtained with either of the two-zone configurations (A, B) were lower and the amount of H<sub>2</sub> higher.
- The amounts of C<sub>2</sub>H<sub>2</sub> and C<sub>2</sub>H<sub>4</sub> obtained with configuration A were lower but those obtained with configuration B showed no significant difference.
- The amounts of CO<sub>2</sub> obtained with configuration B were higher but the ones obtained with configuration A showed no significant difference.

The above observations imply that the two-zone reactor concept allows for more efficient decomposition of CH<sub>4</sub> and C<sub>2</sub>-hydrocarbons compared to the drop-tube gasifier operating at comparable reactor tube temperatures. At present, it is not clear whether this should be attributed to a higher gas temperature, an increased residence time of the gas, or both. In addition, it appears that the two-zone reactor facilitates the water-gas shift reaction (CO + H<sub>2</sub>O  $\leftrightarrow$  H<sub>2</sub> + CO<sub>2</sub>) which may be attributed to the higher gas temperatures as no effort has been made to quench the product gas. The higher extent of the exothermic water-gas shift reaction with increased gas temperatures is to be attributed merely to faster kinetics as the measured concentrations of H<sub>2</sub> and



**Figure 7-6:** Average gas concentrations for a)  $\text{H}_2$ ,  $\text{CO}$ ,  $\text{CO}_2$ , and  $\text{CH}_4$ , and b)  $\text{C}_2\text{H}_2$ ,  $\text{C}_2\text{H}_4$ , and  $\text{C}_2\text{H}_6$  calculated on  $\text{H}_2\text{O}$ ,  $\text{N}_2$ , and  $\text{Ar}$  free basis for the investigated configurations: A = 50 mm tall RPC, B = 100 mm tall RPC, PP = free-fall pure pyrolysis, and SG = free-fall steam-based gasification. Error bars indicate the span between the minimum and maximum values.

$\text{CO}_2$  were still below the values expected from thermodynamic equilibrium [59].

The LHV<sub>s</sub> of the syngas were 15.9 MJ/kg (12.5 MJ/Nm<sup>3</sup>) for configurations A and B, and 18.5 and 17.0 MJ/kg (15.6 and 14.4 MJ/Nm<sup>3</sup>) for PP and SG, respectively. The statistically higher values for PP and SG originate from the higher content of light hydrocarbons. For all cases, however, the heating values achieved in this work were substantially higher than those obtained in conventional autothermal bagasse gasification. For example, the air-blown cyclone particle-gasifier by Gabra et al. [8] and the air-blown downdraft gasifier for bagasse pellets by Erlich and Fransson [94] produced syngas with an LHV of 4.8–8.1 MJ/Nm<sup>3</sup> and 9.5 MJ/Nm<sup>3</sup>, respectively. For comparison reasons, all LHV<sub>s</sub> are reported on a H<sub>2</sub>O and N<sub>2</sub> free basis. The higher values obtained in the solar gasification were mainly due to the lower content of CO<sub>2</sub>.

**Table 7-2:** Summary of the statistical analysis for the effects of reactor configurations: for comparison X vs. Y “>” or “<” designate statistically higher or lower mean of a response for the configuration X; “~” designates no statistically significant difference.

response	A vs. B <sup>*</sup>	A vs. SG <sup>†</sup>	B vs. SG <sup>†</sup>	A vs. PP <sup>†</sup>	B vs. PP <sup>†</sup>
$y_{\text{H}_2}$	>	>	>	>	>
$y_{\text{CO}}$	~	<	<	<	<
$y_{\text{CH}_4}$	<	<	<	~	~
$y_{\text{CO}_2}$	~	~	>	>	>
$y_{\text{C}_2\text{H}_2}$	~	<	~	<	<
$y_{\text{C}_2\text{H}_4}$	~	<	~	<	<
$y_{\text{C}_2\text{H}_6}$	-	-	-	-	-
LHV	~	<	<	<	<
$U$	~	~	>	~	>
$X_{\text{C}}$	~	~	>	~	>

\* two-sample *t*-tests at a significance level of 5% with equal variances of the unpaired samples

† single-sided Grubb’s outlier tests [40] at a 5% confidence level

Carbon conversions  $X_C$  and upgrade factors  $U$  are presented in Figure 7-7. The carbon conversions for configurations A and B were calculated to be around 87% and 89%, respectively. For B, this is a statistically significant improvement over both PP (64%) and SG (69%), in spite of the considerably lower reactor temperatures. Remarkably, the improvement for configuration A could not be shown to be significant by the Grubbs test due to the scatter in the data and a small sample size. The reasons for the generally low carbon conversion may be attributed to insufficient solids retention or particle build up on top of the RPC that was observed in some experiments.

The upgrade factor calculated was found to be  $\sim 1.05$  for cases A and B, and less than 1 for PP and SG. This means that the biomass could be energetically upgraded by 5% effectively storing solar energy in the syngas.

Figure 7-8 shows the RPC after one of the A experiments. The easily removable char particles were quite uniformly distributed throughout the entire structure, thereby implying rather volumetric char gasification. It was possible to feed up to 77 g/h bagasse without a significant increase in the pressure drop

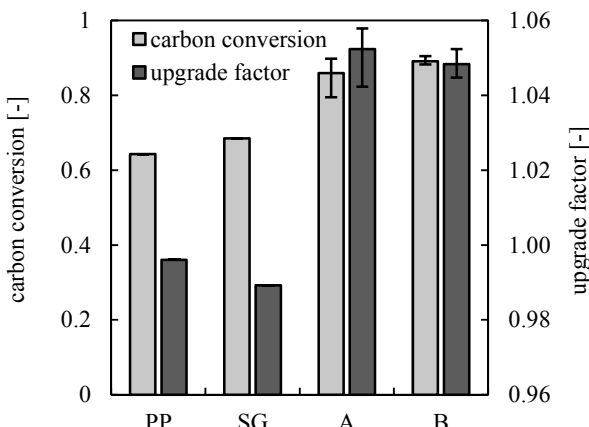


**Figure 7-7:** Carbon conversion and upgrade factors for investigated configurations: A = 50 mm tall RPC, B = 100 mm tall RPC, PP = free-fall pure pyrolysis, SG = free-fall steam gasification. Error bars illustrate the span between the minimum and maximum values.

over the RPC. This corresponds to a particle flux per cross-sectional area of 16 g/s·m<sup>2</sup>. At higher feeding rates char started to deposit on top of the RPC. The elemental analysis of the solid residue showed lower carbon conversion for particles collected in the product collection drum than for the particles retrieved from the RPC. This implies that the retention of the particles by the RPC and/or their interaction with the RPC surface is the key for increasing the overall carbon conversion.

The energy conversion efficiency is defined as

$$\eta = \frac{m_{\text{syngas}} \text{LHV}_{\text{syngas}}}{\int_{t_0}^{t_{\text{end}}} \dot{Q}_{\text{solar}} dt + m_{\text{bagasse}} \text{LHV}_{\text{bagasse}} - m_{\text{C,in}} (1 - X_{\text{C}}) \text{LHV}_{\text{char}}} \quad (7.2)$$

$\eta$  strongly depends on the feeding rate. For reporting the maximum  $\eta$  it is thus important to consider only the experiments in which no particle build-up was



**Figure 7-8:** The 50 mm tall RPC after one of the A experiments. The particles are uniformly distributed throughout the entire RPC.

observed. Under this constraint, the highest efficiency of  $\eta = 21.6\%$  was achieved at a feeding rate of 73 g/h (experiment A3). To overcome the throughput constraints and increase  $\eta$  it is necessary to develop a method for on-line ash removal from the RPC and improve the control of the solids residence time. Since the particles deposited on the RPC were easy to remove, vibration and/or occasional pulse-flow of purge gas (inert or syngas) could serve as means for achieving both of these tasks that should be addressed by future research.

## 7.4 Energy Balance and Heat Losses

To gain an insight to the energy flows in the solar reactor and to understand where energetic improvements to the reactor design are possible, an energy balance across the reactor has been applied. The energy flows considered

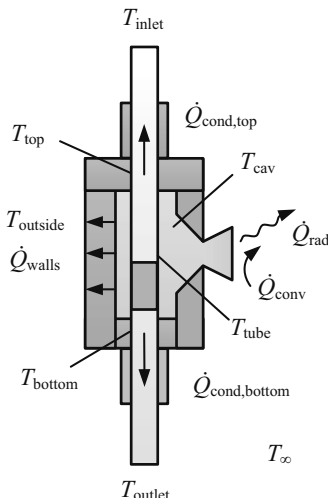


**Figure 7-9:** Overview temperature measurements and heat losses: radiation and convection through the aperture  $\dot{Q}_{\text{rad}}$  and  $\dot{Q}_{\text{conv}}$ , conduction through the cavity walls  $\dot{Q}_{\text{walls}}$  and along the reactor tube towards the top  $\dot{Q}_{\text{cond,top}}$  and the bottom  $\dot{Q}_{\text{cond,bottom}}$ .

include the heat transferred to the reactants  $\dot{Q}_{\text{net}}$  as well as the major heat losses, namely radiation and convection through the aperture of the cavity  $\dot{Q}_{\text{rad}}$  and  $\dot{Q}_{\text{conv}}$ , conduction through the insulation at the cavity walls  $\dot{Q}_{\text{walls}}$ , and conduction along the reactor tube towards the top  $\dot{Q}_{\text{cond,top}}$  and the bottom  $\dot{Q}_{\text{cond,bottom}}$ . An overview of the location of the heat losses and the temperature measurements that were used for their determination is given in Figure 7-9.

#### 7.4.1 Heat Transfer to Reactants

The net heat transfer to the reactants  $\dot{Q}_{\text{net}}$  was determined by an energy balance across the reactor tube.

$$\dot{Q}_{\text{net}} = \dot{H}_{\text{out}} - \dot{H}_{\text{in}} \quad (7.3)$$

where  $\dot{H}_{\text{in}}$  and  $\dot{H}_{\text{out}}$  are the enthalpy flows entering the reactor tube at the top and leaving it at the bottom. Steam and N<sub>2</sub> enter the reactor at the measured  $T_{\text{in}}$ , Ar and bagasse enter at ambient temperature  $T_{\infty} = 298$  K. The product gases leave the reactor at  $T_{\text{out}}$ , which was measured at the bottom seal. The unreacted char was assumed to be pure carbon and to leave the reactor at  $T_{\infty}$ .

$$\dot{H}_{\text{in}} = \dot{n}_{\text{H}_2\text{O}} \bar{h}_{\text{H}_2\text{O}}(T_{\text{steam}}) + \dot{n}_{\text{N}_2} \bar{h}_{\text{N}_2}(T_{\text{steam}}) + \dot{n}_{\text{Ar}} \bar{h}_{\text{Ar}}(T_0) + \dot{n}_{\text{CH}_x\text{O}_y} \bar{h}_{\text{CH}_x\text{O}_y} \quad (7.4)$$

$$\dot{H}_{\text{out}} = \sum_i \dot{n}_{i,\text{out}} \bar{h}_i(T_{\text{out}}) + \dot{n}_{\text{C}} \bar{h}_{\text{C}} \quad (7.5)$$

where  $i = \text{N}_2, \text{Ar}, \text{H}_2\text{O}, \text{H}_2, \text{CO}, \text{CO}_2, \text{CH}_4, \text{C}_2\text{H}_2, \text{C}_2\text{H}_4$ , and  $\text{C}_2\text{H}_6$ . The enthalpy of species  $i$  is defined as

$$\bar{h}_i(T) = \bar{h}_{f,i}^0 + \int_{T_0}^T \bar{C}_{p,i} dT \quad (7.6)$$

The enthalpies of the bagasse  $\bar{h}_{\text{CH}_x\text{O}_y}$  and the char  $\bar{h}_{\text{C}}$  are based on their LHV and composition.

$$\bar{h}_{\text{CH}_x\text{O}_y} = \frac{x}{2} \bar{h}_{\text{H}_2\text{O(g)}} + \bar{h}_{\text{CO}_2} + \text{LHV}_{\text{CH}_x\text{O}_y} M_{\text{CH}_x\text{O}_y} \quad (7.7)$$

$$\bar{h}_C = \bar{h}_{CO_2} + LHV_{char} M_{char} \quad (7.8)$$

### 7.4.2 Radiation Losses

The radiation losses through the aperture were computed using the net-radiation method for enclosures [95] with the following assumptions: (a) all surfaces are opaque-gray-diffuse, (b) uniform temperature, flux, and optical properties over each element, and (c) non-participating medium/gas in the cavity space. The net radiative flux  $q_j$  leaving surface  $j$  was computed by solving the following system of equations

$$\sum_{j=1}^N \left( \frac{\delta_{ij}}{\varepsilon_j} - F_{i-j} \frac{1-\varepsilon_j}{\varepsilon_j} \right) \cdot q_j = \sum_{j=1}^N (\delta_{ij} - F_{i-j}) \cdot \sigma T_j^4 \quad (7.9)$$

for the surfaces  $i = 1, 2, \dots, N$ .  $\delta_{ij}$  is the Kronecker delta defined as:

$$\delta_{ij} = \begin{cases} 1 & \text{when } i = j \\ 0 & \text{when } i \neq j \end{cases} \quad (7.10)$$

The cavity was treated as an enclosure of three discrete internal surfaces ( $N = 3$ ), cavity wall, reactor tube and aperture. The view factors  $F_{ij}$  were calculated by Monte-Carlo ray tracing of  $10^9$  rays using the in-house code Vegas [96]. Emissivities of  $\varepsilon = 1$  for the aperture,  $\varepsilon = 0.86$  for the SiC tube [97], and  $\varepsilon = 0.58$  for the cavity insulation [98] were applied. The temperature of the aperture and the reactor tube were  $T_{apt} = 0$  K and the measured  $T_{tube}$ , respectively. The cavity temperature  $T_{cav,rad}$  was defined as the quartic mean of all  $n$  measured cavity temperatures  $T_{cav,i}$ .

$$T_{cav,rad} = \sqrt[4]{\frac{1}{n} \sum_{i=1}^n T_{cav,i}^4} \quad (7.11)$$

### 7.4.3 Convective Losses

The convective heat losses from the cavity through the aperture were estimated by solving the steady state mass, momentum, and thermal energy conservation equations using the commercial computational fluid dynamics (CFD) tool Ansys CFX [99]. The domain was divided into: 1) a cavity, 2) a cone representing the CPC, and 3) a rectangular volume extending outwards 150 mm from the shield representing the surroundings. No-slip conditions and uniform temperatures were applied to the wall boundaries:  $\bar{T}_{\text{cav}}$  (arithmetic average of all  $T_{\text{cav},i}$ ) for the cavity and  $T_0 = 298$  K for the cone and the shield, which were both water cooled. The remaining boundaries on the rectangular volume were modeled as openings with the fluid temperature  $T_0$  and a pressure  $p_0 = 1$  atm. The buoyancy driven flow was assumed to be laminar. This is appropriate along the cavity walls because [100]

$$\text{Gr} = g \left( \frac{\bar{T}_{\text{cav}}}{T_0} - 1 \right) \frac{L^3}{v^2} < 10^9 \quad (7.12)$$

where  $L$  is the distance from the top edge of aperture to the bottom of cavity [101] and  $v$  is the kinematic viscosity evaluated at  $(\bar{T}_{\text{cav}} - T_0)/2$ . Furthermore, it is appropriate through the aperture because

$$\text{Re} = \frac{\rho L u}{\mu} < 10^3 \quad (7.13)$$

where  $L = d_{\text{apt}}/2$ ,  $\rho$  and  $\mu$  are the fluid density and the dynamic viscosity evaluated at  $T_0$ , and  $u$  is the maximum computed velocity. The fluid (air) was modeled as ideal gas neglecting viscous dissipation. The values of thermal conductivity, dynamic viscosity, and specific heat were taken from correlations [102]. The governing equations were solved on a mesh that was refined around the aperture and the top of the CPC inlet. A grid refinement study was performed and it was found that the solution is grid-independent for a mesh with ~2.2 million tetrahedron cells.

Figure 7-10 shows a contour plot of the temperature distribution in the domain for a selected  $\bar{T}_{\text{cav}}$ . The fluid temperature is almost uniform within the

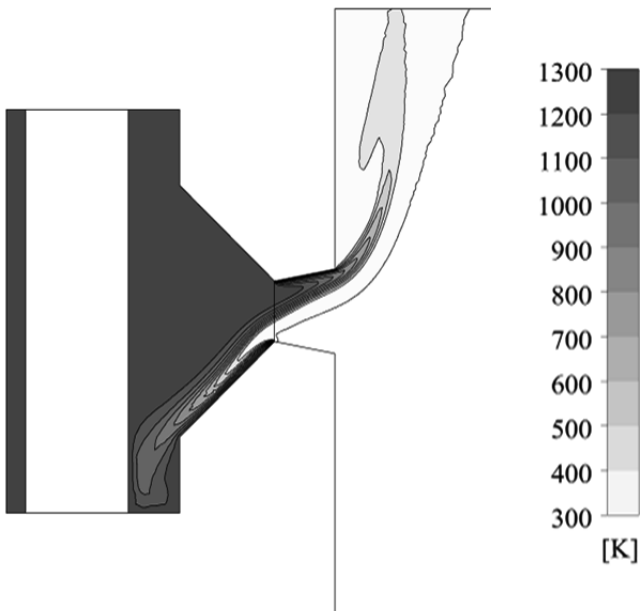


**Figure 7-10:** Convection losses through aperture: Air temperature distribution in cavity, aperture, and surrounding.

cavity except below the aperture. Cold air from the outside of the cavity flows through the aperture towards the bottom of the reactor. The cold air is then heated and flows out of the reactor at the top of the aperture rising towards the top after leaving the cavity.

The convective heat loss computed for cavity temperatures  $\bar{T}_{\text{cav}}$  between 500 and 1500 K, and was found to be well represented by the following correlation.

$$\dot{Q}_{\text{conv}} = -1.13 \cdot 10^{-5} (\bar{T}_{\text{cav}} - T_0)^2 + 6.19 \cdot 10^{-2} (\bar{T}_{\text{cav}} - T_0) - 2.66 \text{ [W]} \quad (7.14)$$

#### 7.4.4 Conduction through the Cavity Walls

For the estimate of the conduction losses through the cavity walls it was assumed that the inside and outside surfaces of the cavity are at a uniform temperature allowing the use of shape factors for the estimate of the heat transfer.

$$\dot{Q}_{\text{walls}} = k_{\text{eff,ins}} \cdot S \cdot (\bar{T}_{\text{cav}} - T_{\text{outside}}) \quad (7.15)$$

where  $k_{\text{eff,ins}}$  is the effective thermal conductivity of the insulation,  $S$  the total shape factor and  $T_{\text{outside}}$  is the temperature measured at the outer wall of the cavity. The total shape factor  $S$  is the sum of all individual shape factors  $S_i$ .  $S_{\text{wall}} = A/D$ ,  $S_{\text{edge}} = 0.54L$ ,  $S_{\text{corner}} = 0.15D$  with the surface area of wall  $A$ , the wall thickness  $D$ , and the length of edge  $L$  [103]. The effective thermal conductivity of the insulation is computed as

$$k_{\text{eff,ins}} = \frac{\int_1^2 k_{\text{ins}}(T) dT}{T_2 - T_1} \quad (7.16)$$

#### 7.4.5 Conduction along Reactor Tube

The conduction losses along the reactor tube ( $\dot{Q}_{\text{tube}}$ ) were estimated by numerically solving the steady heat conduction equation with a 1D finite volume model. Convective and radiative heat fluxes ( $\dot{Q}_{\text{conv},i}$  and  $\dot{Q}_{\text{rad},i}$ ) were determined based on the surface temperature of each cell ( $T_{\text{surf},i}$ ).

$$\dot{Q}_{\text{rad},i} = P \cdot \Delta x \cdot \sigma \cdot \varepsilon_{\text{SiC}} \cdot T_{\text{surf},i}^4 \quad (7.17)$$

$$\dot{Q}_{\text{conv},i} = P \cdot \Delta x \cdot h_{\text{sf}} \cdot (T_{\text{surf},i} - T_0) \quad (7.18)$$

where  $P$  is the perimeter of the tube,  $\Delta x$  is the element length, and  $\sigma$  is the Stefan-Boltzmann constant.  $\varepsilon_{\text{SiC}} = 0.86$  is the emissivity of the SiC tube [97],  $h_{\text{sf}}$  the convective heat transfer coefficient, and  $T_{\text{surf},i}$  the surface temperature of the

element  $i$ . For the non-insulated parts of the reactor tube the surface temperature is equal to the cell temperature ( $T_{\text{surf},i} = T_i$ ). For the insulated parts, the surface temperature was determined by setting the heat flux through the insulation to

$$\dot{Q}_{\text{ins},i} = \frac{2\pi k_{\text{eff,ins}} (T_i - T_{\text{surf},i}) \Delta x}{\ln(d_{\text{ins}} / d_{\text{tube}})} = \dot{Q}_{\text{rad},i} + \dot{Q}_{\text{conv},i} \quad (7.19)$$

The temperature dependent thermal conductivity of the insulation  $k_{\text{eff,ins}}$  was evaluated at each finite volume. The convective heat transfer coefficient  $h_{\text{sf}}$  was determined by a Nusselt correlation for vertical cylinders with diameter  $d$  and length  $L$  [104].

$$\text{Nu} = \left\{ 0.825 + 0.387 \left[ \text{Ra} \cdot f_1(\text{Pr}) \right]^{1/6} \right\}^2 + 0.435 \frac{L}{d} \quad (7.20)$$

where

$$f_1(\text{Pr}) = \left[ 1 + \left( \frac{0.492}{\text{Pr}} \right)^{9/16} \right]^{-16/9} \quad (7.21)$$

$\text{Pr}$  is the Prandtl number, and  $\text{Ra}$  the Rayleigh number.

At both ends of each domain, fixed temperature boundary conditions were applied representing the temperatures measured at the carbon seals and where the reactor tube passes through the cavity walls.

#### 7.4.6 Interpretation

The resulting heat losses as well as the heat transferred to the reactants are illustrated in Figure 7-11 and summarized in Table 7-3. The power input calculated from the sum of all losses and the heat transfer to the reactants was within 10% of the experimentally measured power input. It was found that the radiative and convective heat losses through the aperture are in the order of  $\dot{Q}_{\text{rad}} = 126 \text{ W}$  and  $\dot{Q}_{\text{conv}} = 47 \text{ W}$ , accounting for only 10% and 4% of the total calculated power input. The major heat losses occur by conduction. The

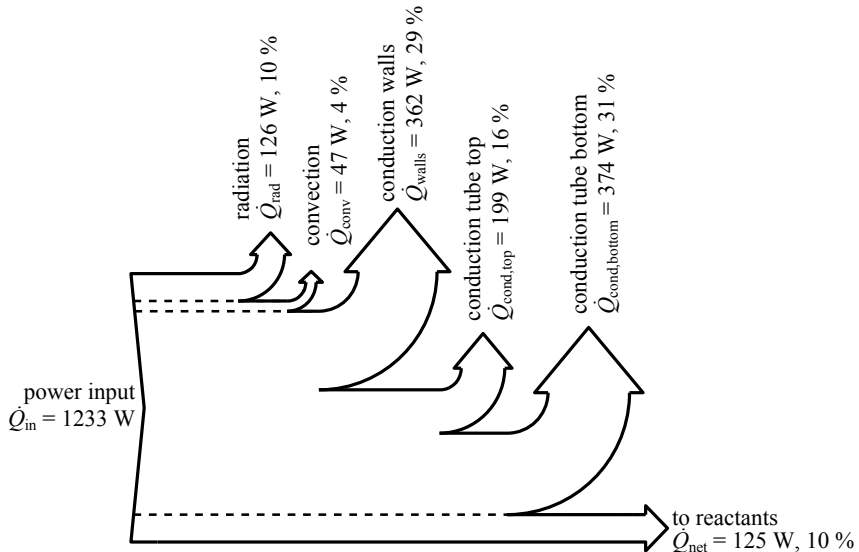


**Figure 7-11:** Energy losses of solar reactor via radiation and convection through the aperture  $\dot{Q}_{rad}$  and  $\dot{Q}_{conv}$ , conduction through the walls  $\dot{Q}_{walls}$  and along the tube  $\dot{Q}_{cond,top}$  and  $\dot{Q}_{cond,bottom}$ .

conduction losses through the cavity walls and along the reactor tube are 29% and 47% of the input power ( $\dot{Q}_{walls} = 362 \text{ W}$  and  $\dot{Q}_{tube} = \dot{Q}_{cond,top} + \dot{Q}_{cond,bottom} = 573 \text{ W}$ ). The heat transferred to the reactants is around  $\dot{Q}_{net} = 125 \text{ W}$  or 10% of the input power.

The energy flows calculated suggest first of all better insulation to reduce conduction losses. The losses through the walls can easily be reduced by applying thicker insulation. A reduction of the conduction losses along the tube imposes a more difficult task as the preferably well conducting reactor tube needs to be sealed at colder temperatures. More importantly they suggest improving the heat utilization of the process by increasing the throughput and heat transfer to the reactants. Such an improvement has a much bigger effect on the overall performance of the reactor.

**Table 7-3:** Energy flows in the solar reactor.

radiation through aperture, $\dot{Q}_{\text{rad}}$	126 W	10.2%
convection through aperture, $\dot{Q}_{\text{conv}}$	47 W	3.8%
conduction		
- through walls, $\dot{Q}_{\text{walls}}$	362 W	29.3%
- along tube (top / bottom), $\dot{Q}_{\text{tube}}$	573 W	46.6% (16.2% / 30.4%)
heat to reactants, $\dot{Q}_{\text{net}}$	125 W	10.2%
calculated power input, $\dot{Q}_{\text{in}}$	1233 W	
(sum of the above)		
measured power input	1174 W	

## 7.5 Conclusions

A two-zone solar-driven biomass gasifier concept has been proposed and evaluated at a 1.5 kW<sub>th</sub> solar radiative power input with bagasse particles. Its first zone operates in a drop-tube mode which ensures efficient radiative heat transfer to dispersed biomass particles that is required for fast pyrolysis. Its second zone is designed to operate as a trickle bed consisting of a structured packing that increases solids holdup in the hot zone, thereby providing residence time and temperature needed for the rate limiting char gasification and the decomposition of the pyrolysis products.

A series of 20 min gasification experiments with bagasse particles and steam were performed on a high-flux solar simulator to compare the drop-tube trickle-bed reactor with a drop-tube reactor. It was demonstrated that the two-zone reactor concept decomposes CH<sub>4</sub> and C<sub>2</sub>-hydrocarbons more efficiently than the drop-tube gasifier operating at comparable reactor tube temperatures. The concentrations of H<sub>2</sub> and CO<sub>2</sub> were higher than in the drop tube reactor, whereas the concentrations of CO were lower, which has been attributed to a higher extent of the water-gas shift reaction due to a higher gas temperature.

The LHV of the syngas produced by the two-zone reactor was around 15.9 MJ/kg, which is substantially higher than those typically obtained in

conventional autothermal bagasse gasification [8, 94]. The biomass was energetically upgraded by 5%, effectively storing solar energy in the syngas. The maximum energy conversion efficiency was 21%.

An energy balance applied to the solar reactor indicated the highest losses are due conduction through the cavity walls and along the reactor tube accounting for 29% and 47% of the total input power. As only 10% of the input power was transferred to the reactants the largest efficiency gains can be achieved by increasing the throughput and improving the heat transfer to the reactants.

It is important to note that the concept has only been evaluated under the very limited conditions of both short-term operation (20 min) and light particle loadings (a maximum particle flux of up to  $16 \text{ g/s-m}^2$  was achieved without particle build-up on the structure packing). Future research should address on-line ash removal from the structure packing to increase the throughput and ensure longer term operability.



## **Chapter 8**

### **Heat- and Mass-Transfer Analysis of a Trickle-Bed Gasifier<sup>a</sup>**

The previously introduced drop-tube trickle-bed solar reactor concept that aims at providing high heat transfer rates to the gas and solid phase showed favorable results in terms of carbon conversion and selectivity towards H<sub>2</sub> and CO in comparison to a pure drop-tube design. To understand the mass and heat-transfer phenomena leading to the more favorable performance a numerical heat transfer model of an allothermal tubular reactor gasifying beech char particles with steam was developed. The model considers steady-state, two-dimensional finite-volume material and energy balances and accounts for all three modes of heat transfer: conduction and radiation from the wall through the RPC and convection from the RPC surface to the flowing gas. The contribution of the chemical reaction was evaluated based on an apparent first-order rate law after adopting a suitable value of the activation energy from the literature and optimizing the pre-exponential factor for the best agreement between the model predictions and experimental results obtained in a laboratory-scale electrically heated reactor prototype. The model was then used to assess the sensitivity of the gasification rate and the reactor temperatures to the particle loading and the RPC properties such as pore diameter, porosity, and thermal conductivity. In addition, the performance of the trickle-bed reactor was numerically compared to the performance of a moving bed as an alternative concept for increasing the residence time of the char particles.

---

<sup>a</sup> Material of this chapter is published in: M. Kruesi, Z. R. Jovanovic, A. Haselbacher, and A. Steinfeld, "Analysis of Solar-Driven Gasification of Biochar Trickling through an Interconnected Porous Structure", *submitted*

## 8.1 Experimental Investigation

### 8.1.1 Experimental Setup

A schematic of the experimental ambient-pressure concurrent gas-solid trickle-bed reactor setup is shown in Figure 8-1. A 1.2 m long alumina reactor tube having an inner diameter of 0.06 m and a wall thickness of 5 mm was situated inside an electrical tube furnace (Carbolite) to simulate the conditions of absorbing cavity-receivers that are heated by concentrated solar radiation [41, 105]. Two 0.1 m tall RPC pieces, as the one shown in Figure 8-2 , were stacked and inserted into the alumina tube with the stack's top at the middle of the hot zone and held in place by another smaller diameter supporting alumina tube. The RPC was made of SiSiC (silicon-infiltrated silicon carbide) with a high thermal conductivity ( $k_{\text{SiC}} = 36 \text{ W/m-K}$  at 1273 K) and an overall porosity of

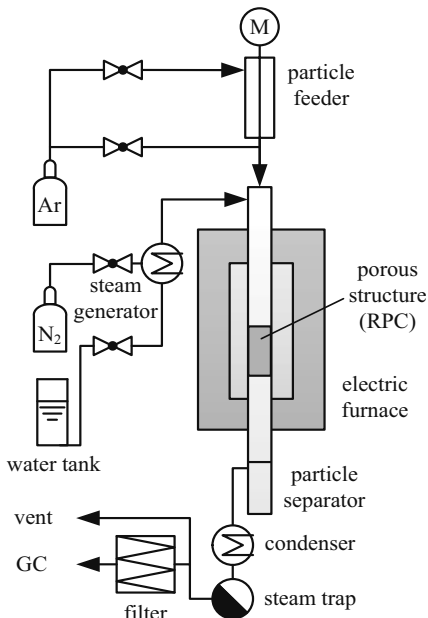


**Figure 8-1:** Schematic of the experimental setup.

$\varphi_{RPC} = 89\%$  with a nominal pore diameter of  $d_{nom} = 2.54$  mm corresponding to 10 ppi (pores per inch).

Temperatures were measured with seven K-type thermocouples positioned as illustrated in Figure 8-3: four along the centerline of the RPC (C1–C4) and five along at the tube/RPC interface (W1–W5). Two movable thermocouples (W6, W7) were used to measure the wall temperature above and below the RPC. The  $z$ -coordinates of the thermocouples are listed in Table 8-1.

The particles were fed via a calibrated feeding system (LAMBDA Laboratory Instruments) from an Ar-purged hopper positioned above the tube. A sweep Ar flow was introduced through a side port below the feeding system to prevent the steam from back-flowing and condensing in the hopper. The  $N_2$ -entrained steam generated with an external evaporator (Bronkhorst) was introduced at the top of the alumina tube. The flow rates of the gases and water

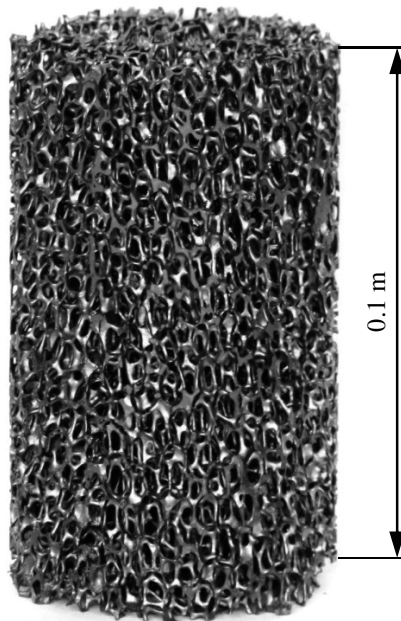


**Figure 8-2:** Photograph of the SiSiC reticulate porous ceramic (RPC) with 10 pores per inch (ppi) used as packing in the tubular gasifier.

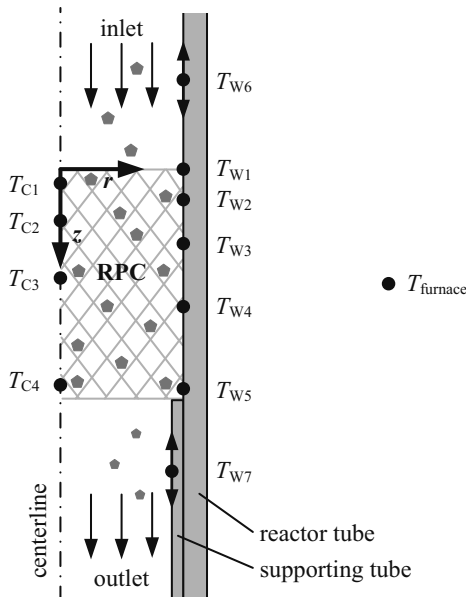


**Figure 8-3:** Schematic (not to scale) of the main reactor tube, RPC, and supporting tube assembly indicating thermocouple locations. Thermocouples  $T_{W6}$  and  $T_{W7}$  were movable along the tube wall.

**Table 8-1:** Thermocouple positions: W = wall, C = centerline.

thermocouple	$z$ -coordinate [m]
W1	0.00
W2	0.02
W3	0.05
W4	0.12
W5	0.18
W6	-0.60–0.00
W7	0.20–0.60
C1	0.02
C2	0.05
C3	0.10
C4	0.18

into the evaporator were controlled with Bronkhorst mass flow controllers pre-calibrated by Bios Definer 220.

Ash and unreacted char were removed from the gaseous product stream in the particle separator located below the reactor just before a condenser and a steam trap. A slip-stream of the product gas was withdrawn after the condenser and analyzed by gas chromatography (GC) after being filtered and chilled to remove particulate matter and condensable components. The two-channel Varian Micro-GC was equipped with Molsieve-5A and Poraplot-U columns (~1/120 Hz sampling frequency) and was capable of determining concentrations of H<sub>2</sub>, N<sub>2</sub>, CO, CH<sub>4</sub>, CO<sub>2</sub>, C<sub>2</sub>H<sub>2</sub>, C<sub>2</sub>H<sub>4</sub>, and C<sub>2</sub>H<sub>6</sub>. The flow rate of N<sub>2</sub> used to entrain the steam was used as reference to calculate the total molar flow rate at the outlet of the reactor.

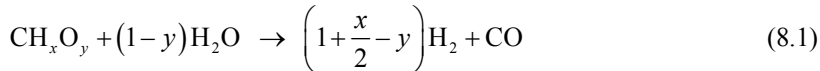
### 8.1.2 Experimental Procedure

Experiments were completed to test four sets of input conditions: a steam concentration of 15%<sub>vol</sub> at nominal furnace temperatures  $T_{\text{furnace}} = 1173, 1223,$  and 1273 K and a steam concentration of 20%<sub>vol</sub> at  $T_{\text{furnace}} = 1223$  K. Each experimental condition was tested twice to ensure repeatability. Additionally, a free-fall drop-tube reference experiment with no RPC in place was completed with an inlet steam concentration of 15%<sub>vol</sub> at  $T_{\text{furnace}} = 1273$  K.

After being purged with Ar and leak-tested, the reactor was preheated to the desired furnace temperature. The flows of Ar, N<sub>2</sub>, and steam were set to provide a total inlet gas flow rate of 12.12 L<sub>N</sub>/min<sup>b</sup> (9 mmol/s) to the reactor. After the temperature equilibrated, the biomass feed commenced at a nominal rate of 1.10 g/min corresponding to a mass flux of 6.5 g/s-m<sup>2</sup>. The resulting molar steam to biomass ratios ( $\dot{n}_{\text{H}_2\text{O(g)}}/\dot{n}_{\text{CH}_3\text{O}_y}$ ) were 1.03 or 1.36, corresponding to 1.11 or 1.47 times the stoichiometric amount of steam for the idealized net reaction represented by

---

<sup>b</sup> L<sub>N</sub> designates normal liters at 273 K and 1 atm.



Temporal gas compositions, temperature, and pressure data were recorded over the course of each experiment (43–51 min). The reactor was operated without any interruptions and without clogging of the RPC or increase in pressure drop across the reactor. Ash and char deposited on the RPC were easily removed after the experiments.

### 8.1.3 Experimental Results

The temporal flow rates of H<sub>2</sub>, CO, CO<sub>2</sub>, and CH<sub>4</sub> over the duration of a typical experiment are shown in Figure 8-4. The concentrations of C<sub>2</sub>H<sub>2</sub>, C<sub>2</sub>H<sub>4</sub>, and C<sub>2</sub>H<sub>6</sub> were below the detection limit of the GC. After a rapid increase following the introduction of the particles into the hot zone ①, the product flow rates slowly approached asymptotic values towards the end of the experiment ②.

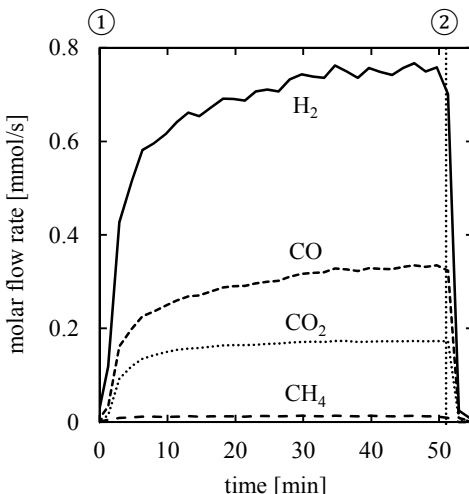


**Figure 8-4:** Temporal product gas flow rates over the course of a typical experiment.

The product flow rates were averaged over the final 10 min of each experiment to obtain representative steady-state test conditions.

The carbon conversion ( $X_C$ ) was defined as the average molar flow rate of carbon leaving the reactor with the monitored product gases ( $\dot{n}_{C,\text{syngas}}$ ) divided by the average molar flow rate of carbon introduced into the reactor with the char particles ( $\dot{n}_{C,\text{char}}$ ), i.e.,

$$X_C = \dot{n}_{C,\text{syngas}} / \dot{n}_{C,\text{char}} \quad (8.2)$$

As shown by Figure 8-5, the carbon conversion in any of the experiments with the RPC was significantly higher than in the reference free-fall drop-tube experiment where the conversion was negligible (less than 1%). Furthermore, the carbon conversion responded well to the furnace temperature: increasing the furnace temperature from 1173 to 1273 K resulted in an increase in carbon conversion from 32% to 52%.

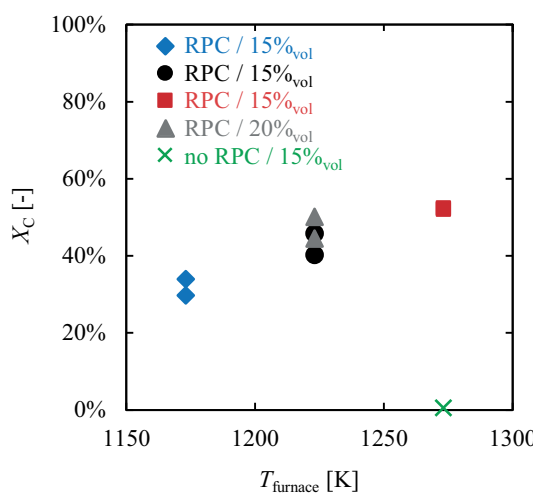


**Figure 8-5:** Carbon conversion ( $X_C$ ) as function of furnace set-point temperature ( $T_{\text{furnace}}$ ), steam concentration, and gasifier configuration (RPC versus no RPC).

## 8.2 Numerical Model

To understand the origin of the experimentally observed enhancing effect of the trickle-bed zone on char gasification, a steady-state two-dimensional numerical model of the reactor was developed. The model provides information on the spatial variations of temperature, steam concentration, and reaction rate within the trickle bed as well as on the relative contribution of the heat transfer by conduction, convection, and radiation. The model is based on a two-dimensional axisymmetric finite-volume representation of a domain encompassing the RPC and its pores that are considered to be filled with gas and particles. A two-dimensional representation is imposed by the fluid flow and heat flux entering the domain in different directions: fluid flow axially from the top and the heat flux radially from the tube wall. The domain is treated as a porous medium with separate solid and fluid phases. The char particles are assigned to the solid phase and gasified according to the overall stoichiometry given by Eq. 8.1. The mass balance for the solid phase was not solved explicitly. Instead, a constant mass of char per unit volume was assigned to the whole domain. With this simplification, the thermal inertia of the particles amounting to about 10% of its gasification enthalpy is neglected.

### 8.2.1 Governing Equations

The mass balance of the fluid phase is

$$\frac{1}{r} \frac{\partial}{\partial r} (r \rho u_r) + \frac{\partial}{\partial z} \rho u_z = \sum_k S_k \quad (8.3)$$

where  $u_z$  and  $u_r$  are the superficial velocities in the axial and radial directions, and  $\rho$  is the density of the gas mixture. The mass source terms  $S_k$  account for the mass of each species  $k$  generated by the chemical reaction.

The fluid-phase conservation equation for species  $k = 1, 2, \dots, N-1$  are given by

$$\begin{aligned} & \frac{1}{r} \frac{\partial}{\partial r} \left[ r \rho (u_r + v_r^c) w_k \right] + \frac{\partial}{\partial z} \left[ \rho (u_z + v_z^c) w_k \right] \\ &= \frac{1}{r} \frac{\partial}{\partial r} \left( r \rho D_{k,\perp} \frac{M_k}{\bar{M}} \frac{\partial y_k}{\partial r} \right) + \frac{\partial}{\partial z} \left( \rho D_{k,\parallel} \frac{M_k}{\bar{M}} \frac{\partial y_k}{\partial z} \right) + S_k \end{aligned} \quad (8.4)$$

where  $w_k$  and  $y_k$  are the mass and mole fractions of species  $k$ ,  $D_{\text{eff},k,\perp}$  and  $D_{\text{eff},k,\parallel}$  are the effective diffusion coefficients within the porous media perpendicular and parallel to the main flow direction, and  $v_r^c$  and  $v_z^c$  are correction velocities to ensure global mass conservation [106].

$$v_r^c = \sum_k D_{\text{eff},k,\perp} \frac{M_k}{\bar{M}} \frac{\partial y_k}{\partial r} \quad (8.5)$$

$$v_z^c = \sum_k D_{\text{eff},k,\parallel} \frac{M_k}{\bar{M}} \frac{\partial y_k}{\partial z} \quad (8.6)$$

The fluid-phase energy equation based on the sensible internal energy of the fluid  $e_s$  can be written as

$$\begin{aligned} & \frac{1}{r} \frac{\partial}{\partial r} (r \rho u_r e_s) + \frac{\partial}{\partial z} (\rho u_z e_s) \\ &= \frac{1}{r} \frac{\partial}{\partial r} \left[ r \rho \sum_k \left( h_{s,k} D_{\text{eff},k,\perp} \frac{M_k}{\bar{M}} \frac{\partial y_k}{\partial r} \right) \right] \\ &+ \frac{\partial}{\partial z} \left[ \rho \sum_k \left( h_{s,k} D_{\text{eff},k,\parallel} \frac{M_k}{\bar{M}} \frac{\partial y_k}{\partial z} \right) \right] + h_{sf} A_0 (T_s - T_f) \end{aligned} \quad (8.7)$$

where  $T_f$  and  $T_s$  are the temperatures of the fluid and solid phases, respectively,  $h_{s,k}$  is the sensible enthalpy,  $M_k$  is the molar mass of species  $k$ , and  $\bar{M}$  is the average molar mass of the fluid. The heat transfer between fluid and solid is expressed by an interfacial heat transfer coefficient  $h_{sf}$  with  $A_0$  being the interfacial area between the two phases. Finally, as all the heat consumed by the chemical reaction  $\dot{Q}_{\text{react}}$  is withdrawn from the solid phase, there is no source term contributing to the fluid-phase energy balance. The terms for fluid-phase heat conduction, viscous dissipation, and pressure work were neglected because  $k_s \gg k_f$ ,  $M^2/\text{Re} \ll 1$ , and  $M^2 \ll 1$ , respectively. ( $M$  and  $\text{Re}$  were estimated for N<sub>2</sub> at  $T_f = 1173$  K,  $u_z = 0.31$  m/s,  $\gamma = 1.33$ ,  $d_{\text{tube}} = 0.06$  m, and  $\mu = 4.7 \cdot 10^{-5}$  Pa·s.)

The energy balance for the solid phase is expressed as

$$0 = \frac{1}{r} \frac{\partial}{\partial r} \left( r k_{\text{eff}} \frac{\partial T_s}{\partial r} \right) + \frac{\partial}{\partial z} \left( k_{\text{eff}} \frac{\partial T_s}{\partial z} \right) + h_{\text{sf}} A_0 (T_f - T_s) - \dot{Q}_{\text{react}} \quad (8.8)$$

where  $k_{\text{eff}}$  is the effective thermal conductivity. The radiative heat transfer within the RPC, an optically thick medium ( $\kappa \gg 1$ ), is modeled with the Rosseland diffusion approximation [95]. An additional term accounting for the radiative contribution  $k_{\text{rad}}$  is thus included in the definition of the effective thermal conductivity,

$$k_{\text{eff}} = k_{\text{cond}} + k_{\text{rad}} \quad (8.9)$$

where  $k_{\text{cond}}$  is the thermal conductivity through the RPC. The heat sink due to the heterogeneous chemical reaction (Eq. 8.1) is given by

$$\dot{Q}_{\text{react}} = \Delta \bar{h}_R \cdot \frac{x_{C,\text{char}} \cdot \rho_{\text{char,bulk}} \cdot l}{M_C} \cdot r_C \quad (8.10)$$

where  $\Delta \bar{h}_R$  is the heat of reaction,  $x_{C,\text{char}}$  the carbon mass fraction of the char,  $\rho_{\text{char,bulk}}$  the bulk density of the char,  $l$  the particle loading, and  $r_C$  the reaction rate. The heat of reaction was computed based on the LHV and heat capacity of the char and the enthalpy of the gaseous species. The particle loading was defined as

$$l = \frac{m_{\text{char, domain}}}{\rho_{\text{char,bulk}} V_{\text{domain}}} \quad (8.11)$$

where  $m_{\text{char, domain}}$  is the mass of char in the domain and  $V_{\text{domain}}$  is the volume of the domain. The reaction rate was represented by a first-order Arrhenius-type rate law given by

$$r_C = -\frac{1}{N_C} \frac{dN_C}{dt} = k_0 \exp\left(-\frac{E_A}{RT}\right) p_{\text{H}_2\text{O}} \quad (8.12)$$

where  $r_C$  is the molar gasification rate of carbon per total number of moles of carbon present ( $N_C$ ),  $E_A$  and  $k_0$  are the apparent activation energy and frequency

factor, respectively,  $R$  is the gas constant, and  $p_{\text{H}_2\text{O}}$  is the partial pressure of steam. This rate law originates from the standard definition of the gasification rate per surface area of char particles

$$\dot{r}_{\text{C}} = -\frac{1}{S_{\text{C}}} \frac{dN_{\text{C}}}{dt} = k_0'' \exp\left(-\frac{E_{\text{A}}}{RT}\right) p_{\text{H}_2\text{O}} \quad (8.13)$$

and the assumption that the carbon surface area  $S_{\text{C}}$  decreases linearly with the conversion [92],

$$S_{\text{C}} = S_{\text{C},0} (1 - X_{\text{C}}) \quad (8.14)$$

Thus, recalling that

$$N_{\text{C}} = N_{\text{C},0} (1 - X_{\text{C}}) \quad (8.15)$$

we have

$$\dot{r}_{\text{C}} = r_{\text{C}}' \frac{S_{\text{C}}}{N_{\text{C}}} = r_{\text{C}}' \frac{S_{\text{C},0}}{N_{\text{C},0}} \quad (8.16)$$

and

$$k_0 = k_0'' \frac{S_{\text{C},0}}{N_{\text{C},0}} \quad (8.17)$$

The apparent activation energy was set to  $E_{\text{A}} = 196$  kJ/mol, a typical value for wood chars reported in the literature [107]. The pre-exponential factor  $k_0$ , however, varies strongly with the feedstock source, size, and morphology. For the purpose of this study,  $k_0$  was set to  $3.3 \cdot 10^6 \text{ s}^{-1} \text{ bar}^{-1}$ , which provided good agreement between the simulated and measured overall gasification rates ( $\dot{n}_{\text{C,syngas}}$ ) and RPC temperatures ( $T_s$ ).

The mass source terms  $S_k$  applied in Eqs. 8.3 and 8.4 are given by

$$S_k = \psi_k M_k \cdot \frac{x_{\text{C,char}} \cdot \rho_{\text{char,bulk}} \cdot l}{M_{\text{C}}} \cdot r_{\text{C}} \quad (8.18)$$

with

$$\psi_k = \begin{cases} -(1-y) & \text{for H}_2\text{O} \\ 1+x/2-y & \text{for H}_2 \\ 1 & \text{for CO} \\ 0 & \text{for N}_2 \\ 0 & \text{for Ar} \end{cases} \quad (8.19)$$

The bulk density of the beech char was  $\rho_{\text{char,bulk}} = 280 \text{ kg/m}^3$  [31].

The momentum equations were not solved. Instead, a profile for the axial velocity was prescribed. Because the boundary layer of the flow through a porous medium is rather thin, a uniform axial velocity at any cross-section perpendicular to the axis, i.e.,  $u_z(r,z) = u_z(z)$ , was considered to be a reasonable assumption. At the operating pressure of 1 bar, the pressure drop across the RPC is small and was thus neglected.

### 8.2.2 Boundary Conditions

On the tube wall, the temperatures of fluid  $T_f$  and solid  $T_s$  were set by linear interpolation of the measured wall temperatures and the species mass fluxes were set to zero. At the centerline, symmetry boundary conditions were applied for all the conservation equations. The inlet conditions for the fluid were set by the total mass flow rate  $\dot{m}_{f,\text{in}}$ , the fluid temperature  $T_{f,\text{in}}$ , and the inlet mass fractions of the species  $w_{k,\text{in}}$ . At the outlet, i.e., at the bottom of the RPC, the diffusive fluxes of mass and energy were set to zero. The net heat fluxes across the inlet and outlet boundaries of the solid phase were computed using the radiosity method for enclosures [95] to account for the radiative heat exchange of the RPC with the reactor tube and tube ends. As shown in Figure 8-6, the tube and RPC surfaces above and below the RPC were each discretized into 100 segments and 64 rings, respectively; the tube ends were considered as single surfaces. Assuming a non-participating medium in the void space, opaque-gray-diffuse surfaces, and uniform temperature, flux, and optical

properties over each surface element, the radiative fluxes  $q_i$  between the  $N_{\text{surf}} = 165$  surface elements were determined from the following system of equations

$$\sum_{j=1}^{N_{\text{surf}}} \left( \frac{\delta_{ij}}{\varepsilon_j} - F_{i-j} \frac{1-\varepsilon_j}{\varepsilon_j} \right) \cdot q_j = \sum_{j=1}^{N_{\text{surf}}} (\delta_{ij} - F_{i-j}) \cdot \sigma T_j^4 \quad i = 1, 2, \dots, N_{\text{surf}} \quad (8.20)$$

where  $\delta_{kj}$  is the Kronecker delta,  $\varepsilon_j$  is the emissivity of surface  $j$ ,  $\sigma$  is the Stefan-Boltzmann constant, and  $F_{i-j}$  are the configuration factors that were determined analytically [108, 109]. The temperatures of the tube elements were based on linear interpolation of the experimentally measured temperatures. The

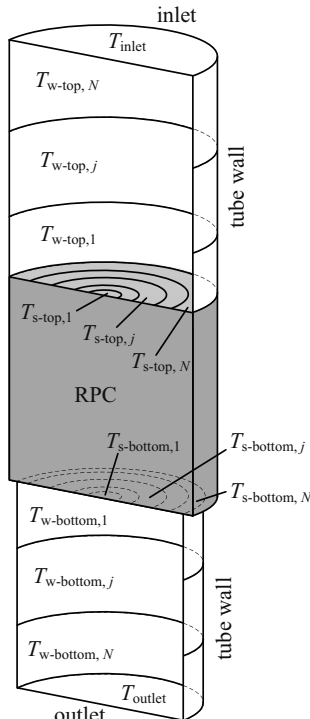


**Figure 8-6:** Discretization for the radiative exchange between the RPC's top and bottom surfaces to their surroundings. Tube sections above and below RPC: 100 segments each, RPC surfaces: 64 rings, flanges: individual surfaces. The smaller tube diameter below the RPC is due to the supporting tube.

emissivities of the top and bottom surfaces of the RPC were set to  $\varepsilon_{\text{RPC,eff}} = 0.82$  so that the radiative flux

$$q_{i,\text{RPC}} = \varepsilon_{\text{eff, RPC}} \sigma T_{i,\text{RPC}}^4 \quad (8.21)$$

corresponds to the emission of an isotropic scattering participating media with emissivity  $\varepsilon_{\text{SiC}} = 0.85$  [97] at a uniform temperature  $T_{i,\text{RPC}}$  [110]. The emissivity of the alumina wall was set to  $\varepsilon_{\text{Al}_2\text{O}_3} = 0.28$  [97].

### 8.2.3 Domain Properties

The effective transport properties of the RPC such as thermal conductivity, interfacial heat transfer coefficient, and extinction coefficient have been studied with pore-level Monte-Carlo ray-tracing and finite-volume heat-transfer simulations based on tomographic scans [111, 112]. An overview of the correlations that were used in the simulations is given in Table 8-2. The

**Table 8-2:** Heat- and mass-transfer property correlations.

quantity	symbol	source
RPC specific surface	$A_0$	Suter and Haussener [111], Eq. 14
RPC tortuosity	$\tau$	Suter and Haussener [111], Table I
RPC interfacial heat transfer coeff. $h_{\text{sf}}$		Suter and Haussener [111], Eq. 17
binary diffusion coefficients	$D_{ij}$	Fuller et al. [113], Eq. 4
diffusion coefficients	$D_k$	Fairbanks and Wilke [114], Eq. 3
dispersion coefficients	$D_L, D_T$	Petrasch [112], Eqs. C.3 and C.4
extinction coefficient	$K$	Petrasch [112], Eq. 4.24
solid thermal conductivity SiC	$k_s$	Munro [115], Eq. 14a
gas viscosity	$\mu$	Yaws [116]
gas-phase thermal conductivity	$k_f$	Yaws [116]
gas-phase sensible enthalpy	$h_s$	Chase [117]
gas isobaric heat capacity	$C_p$	Chase [117]
heat capacity of the char	$C_{p,\text{char}}$	Merrick [118], Eq. 8

radiative contribution to the effective thermal conductivity  $k_{\text{eff}}$  (Eq. 8.9) was defined as

$$k_{\text{rad}} = \frac{16}{3K} \sigma T_s^3 \quad (8.22)$$

where the extinction coefficient was defined as [112]

$$K = \frac{5.5173}{d_{\text{nom}}} (1 - \varphi_{\text{rad}}) \quad (8.23)$$

with a nominal pore diameter of  $d_{\text{nom}} = 2.54$  mm for the 10 ppi RPC. The char particles deposited on the struts of the RPC were accounted for by adjusting the RPC porosity ( $\varphi_{\text{RPC}}$ ) by the particle loading

$$\varphi_{\text{rad}} = \varphi_{\text{RPC}} - l \quad (8.24)$$

The conductive contribution to  $k_{\text{eff}}$  was based on a combination of parallel and serial slabs [112]. In the present case where  $k_s \gg k_f$  the correlation reduces to

$$k_{\text{cond}} = k_s f_{\text{opt}} (1 - \varphi_{\text{RPC}}) \quad (8.25)$$

where  $f_{\text{opt}} = 0.3823$ .

The effective diffusion coefficients  $D_{\text{eff},k,\perp}$  and  $D_{\text{eff},k,\parallel}$  take into account the molecular diffusion through a porous medium and the dispersion induced by the flow through the porous structure,

$$D_{\text{eff},k,\perp} = D_{m,k} \varphi_{\text{eff}} / \tau^2 + D_{d,\perp} \quad (8.26)$$

$$D_{\text{eff},k,\parallel} = D_{m,k} \varphi_{\text{eff}} / \tau^2 + D_{d,\parallel} \quad (8.27)$$

where  $D_{m,k}$  is the molecular diffusion coefficient of species  $k$ ,  $\tau$  is the tortuosity, and  $D_{d,\perp}$  and  $D_{d,\parallel}$  are the dispersion coefficients perpendicular and parallel to the main flow direction, respectively.

### 8.2.4 Numerical Implementation

The governing equations were iteratively solved with a cell-centered finite-volume method. The RPC section of the tube, represented as a cylinder having diameter  $d_{\text{tube}} = 0.06 \text{ m}$  and height  $h_{\text{tube}} = 0.2 \text{ m}$  was discretized into  $N_z$  by  $N_r$  cells in the axial and radial directions, respectively. The discretization in the axial direction was uniform with cell heights  $\Delta z$ . In the radial direction, the mesh was refined towards the wall to resolve the large temperature and concentration gradients. The radial cell sizes were given by

$$\Delta r_i = 1.2^{16/N_r} \Delta r_{i+1} \quad (8.28)$$

The mass balance equation for the fluid phase (Eq. 8.3) was used to compute the velocity field. After integrating Eq. 8.3 over each control volume, the resulting equations were summed in the radial direction, thereby eliminating the radial velocity component. In combination with the axial velocity at the domain boundary and the prescribed velocity profile, this allowed sequentially solving for the axial velocity leaving the control volumes at each axial coordinate. Once the axial velocities were known for the whole domain, the integrated mass balance equations could be sequentially solved for the radial velocity in all control volumes.

The governing equations for the  $N-1$  species, the energy of the fluid phase, and the solid energy were discretized using the hybrid scheme [119] and written into individual linear systems. The solutions of the sparse linear systems were found using MATLAB, either by permutation and forward solving or by the unsymmetric-pattern multifrontal method [120].

At a given iteration step, the velocity field is computed and the species and the fluid and solid phase energy equations are solved sequentially, updating the material properties after each equation. The iteration was terminated if the convergence criterion for the residuals of  $R_i < 10^{-7}$  was reached for all dependent variables ( $u_r, u_z, T_s, w_k, e_s$ ). The residuals  $R_i$  were defined as the root mean square error over all cells of the  $i$ -th iteration normalized by the first iteration. A detailed description of the numerical implementation can be found in Appendix C.

### 8.2.5 Code Verification

An order-verification study was performed using the Method of Manufactured Solutions (MMS) [121] to ensure that the implemented numerical method solves the governing equations correctly [122]. In the MMS, a solution is first assumed (or “manufactured”) and inserted into the governing equations. Unless the manufactured solution happens to be an exact solution of the governing equations, the left- and right-hand sides of the equation will differ. This difference is then added to the right-hand side of the governing equations as a source term to make the manufactured solution an exact solution of the modified governing equations. By solving the modified governing equations numerically, the order of accuracy of the numerical method can be determined even for complicated governing equations that include variable physical properties, for example.

In the present study, the manufactured solution was of the form

$$\Phi_{\text{man}} = A_1 + A_2 \cdot \cos(A_3 \pi r) \cdot \cos(A_4 \pi z) \quad (8.29)$$

where  $\Phi$  is a generic dependent variable. Physical properties such as thermal conductivity, density, and diffusion coefficients were represented in the same form as the dependent variable. All governing equations and their individual terms were verified using the MMS. For brevity, only the results of the order verification of the diffusive terms in the species equation (Eq. 8.4) are reported. The modified equation reads

$$0 = \frac{1}{r} \frac{\partial}{\partial r} \left( r \rho D_{\text{eff},k,\perp} \frac{M_k}{\bar{M}} \frac{\partial y_k}{\partial r} \right) + \frac{\partial}{\partial z} \left( \rho D_{\text{eff},k,\parallel} \frac{M_k}{\bar{M}} \frac{\partial y_k}{\partial z} \right) + L_k \quad (8.30)$$

where  $L_k$  is the source term to fulfill the governing equation for the manufactured solution. The coefficients in Eq. 8.29, the dependent variable, and the properties  $D_{\text{eff},k,\perp}$ ,  $D_{\text{eff},k,\parallel}$ , and  $\rho$  are listed in Table 8-3. Dirichlet boundary conditions were applied on all boundaries.

Figure 8-7a shows the evolution of  $E_2$ , defined as the  $L_2$ -norm of the relative errors in each cell, as a function of the radial mesh spacing. The actual

order of accuracy  $q_a$ , shown in Figure 8-7b, was calculated as the slope of  $E_2$  of successive data points. When using the hybrid scheme, the expected order of accuracy depends on the Péclet (Pe) number. For Eq. 8.30  $\text{Pe} = 0$  and the nominal order of accuracy is 2. In the asymptotic range, the actual order of accuracy  $q_a$  is very close to the nominal order of accuracy, indicating that the numerical implementation is correct. The numerical implementation of all the other terms in the governing equations was also verified to be correct.

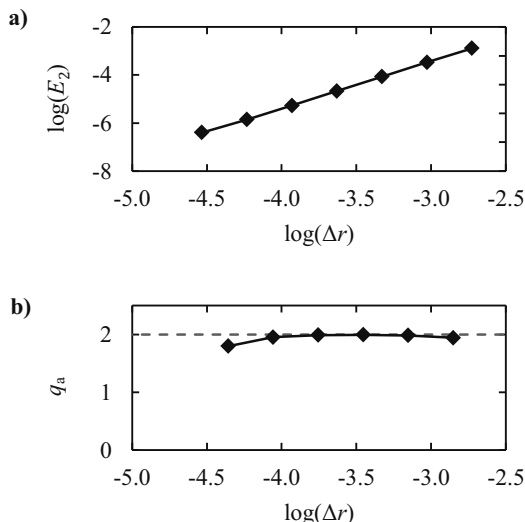


**Figure 8-7:** Results from code verification of the diffusion terms in the species equation, a) error norm  $E_2$  and b) actual order of accuracy  $q_a$ .

**Table 8-3:** Parameters used in order verification study (all in SI units).

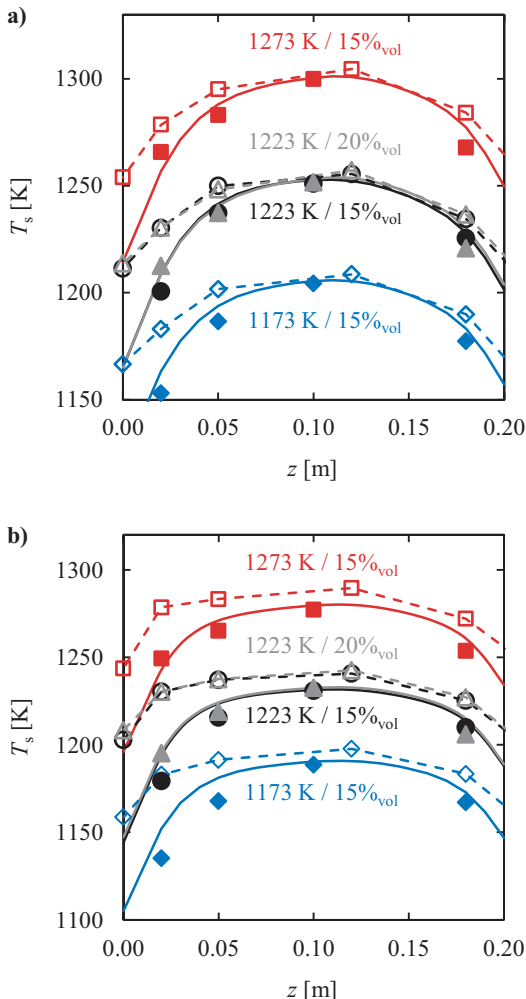
variable	$A_1$	$A_2$	$A_3$	$A_4$
$\rho$	0.1804	0.05	$2.5/r_{\max}$	$3.7/z_{\max}$
$D_{\text{H}_2\text{O}}$	$2.8 \cdot 10^{-4}$	$8.0 \cdot 10^{-3}$	$5/r_{\max}$	$3/z_{\max}$
$w_{\text{H}_2\text{O}}$	0.3	0.2	$0.7/r_{\max}$	$0.8/z_{\max}$
$w_{\text{N}_2}$	0.7	-0.2	$0.7/r_{\max}$	$0.8/z_{\max}$

## 8.3 Simulation Results

### 8.3.1 Model Predictions versus Experimental Results

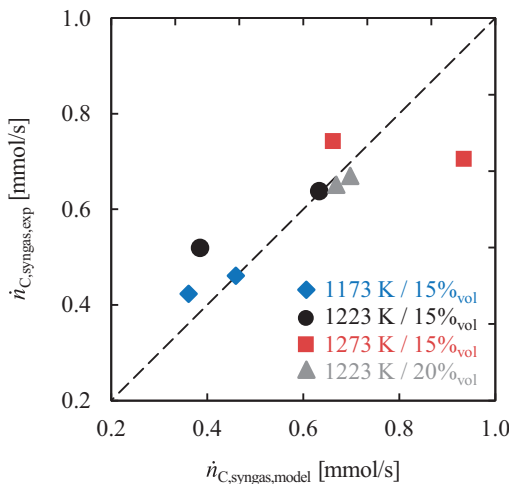
The experiments were simulated using a  $64 \times 64$  cell mesh that provided grid-independent solutions. The experimentally determined particle loadings were used as inputs for the simulations of the reactive case. As the fluid temperature at the inlet to the RPC ( $T_{f,in}$ ) was not measured, it was set to the measured wall temperature 0.25 m above the RPC. This was justified by the relative insensitivity of the carbon conversion and the solid temperatures to changes in  $T_{f,in}$ . (Changing  $T_{f,in}$  by  $\pm 100$  K influenced the gasification rates by less than 1% and the solid centerline temperature at  $z > 0.05$  m by less than 1 K.)

Figure 8-8 compares the measured and simulated solid centerline temperatures for the non-reactive (Figure 8-8a) and the reactive cases (Figure 8-8b). The open and filled symbols indicate the thermocouple measurements at the wall ( $T_{wall,exp}$ ) and at the centerline ( $T_{s,center,exp}$ ), respectively. The dashed lines indicate the wall temperatures ( $T_{wall,bc}$ ) that were set as boundary conditions in the model. The solid lines are the centerline temperatures ( $T_{s,center,sim}$ ) obtained from the numerical model. The simulations of the non-reactive conditions shown in Figure 8-8a were used to assess the model performance in terms of heat transfer only. The predicted centerline temperatures are seen to be in good agreement with experimental measurements. Furthermore, the model is capable of predicting the lower centerline temperatures at both upper and lower boundaries of the RPC that reflect the radiation losses to the surroundings. Figure 8-8b indicates that good agreement between the model and the experiment is also obtained for the reactive cases. The predicted differences between solid and fluid temperatures were in all cases smaller than 1 K for  $z > 0.02$  m; larger differences were observed only in the first rows of cells close to the inlet ( $z < 0.02$  m).



**Figure 8-8:** Comparison between experimental ( $T_{s,\text{center,exp}}$  - filled markers) and simulated centerline solid temperature profiles ( $T_{s,\text{center,sim}}$  - solid lines) for a) non-reacting conditions, and b) reacting conditions. The open markers indicate the experimental wall temperatures ( $T_{\text{wall,exp}}$ ); the dashed lines represent the boundary temperatures ( $T_{\text{wall,bc}}$ ) applied in the simulations.

The parity plot in Figure 8-9 indicates reasonably good agreement between the simulated and experimentally determined molar flow rates of gasified carbon ( $\dot{n}_{C,\text{syngas}}$ ) leaving the reactor. The scatter of the model results for a given furnace temperature and steam concentration are due to differences in the experimentally determined particle loadings.



**Figure 8-9:** Comparison of experimentally determined and simulated molar flow rates of gasified carbon.

### 8.3.2 Sensitivity Analysis

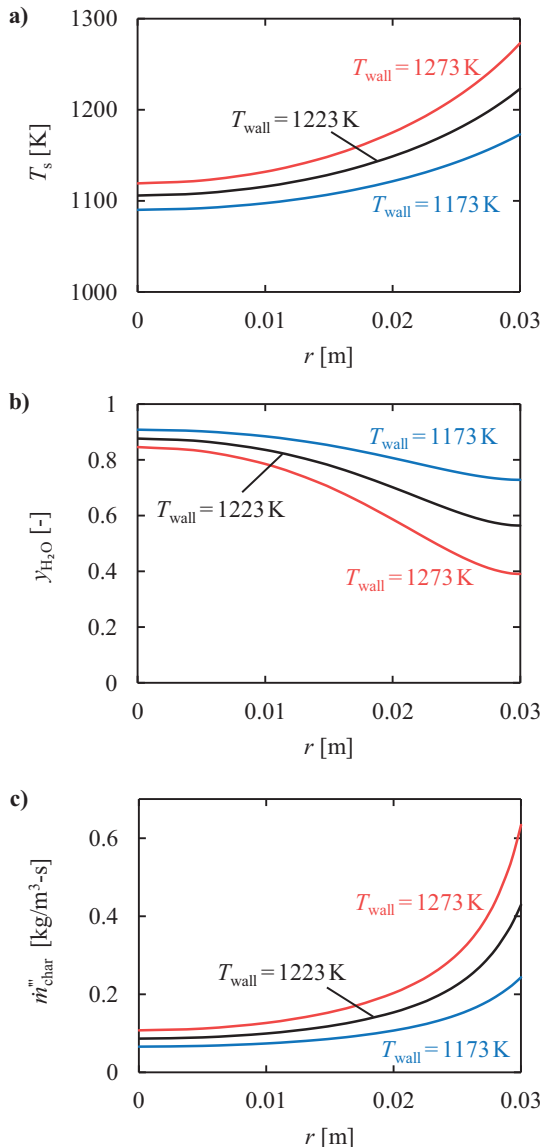
Having demonstrated good agreement with the experimental data, the numerical model was used to conduct a sensitivity analysis of the reactor performance with respect to the reactor wall temperature, particle loading, and RPC properties. The analysis was based on a 1 m tall / 0.06 m inner-diameter domain that is considered a reasonable scale for a pilot-scale reactor on a solar tower. The simulations were carried out on a grid with 64 and 128 cells in radial and axial direction, respectively, yielding grid-independent solutions for the extended domain.

Simulations performed with uniform wall temperatures of  $T_{\text{wall}} = 1173$ , 1223, and 1273 K, a particle loading of  $l = 0.2$ , and pure steam entering the domain at  $\dot{m}_{\text{f,in}} = 2 \text{ g/s}$  and  $T_{\text{f,in}} = 873 \text{ K}$  were adopted as reference conditions. The reference conditions were chosen to provide excess steam for all gasification conditions, i.e. the maximum steam utilization was around 50%. As the key performance indicators reflecting the reactor productivity and syngas quality, the molar flow rates of the gasified carbon leaving the trickle bed ( $\dot{n}_{\text{C,syngas,RPC}}$ ) and solid centerline temperatures at the outlet ( $T_{\text{s,center,outlet}}$ ) are presented in Table 8-4. As shown by this table, increasing the wall temperature from 1173 to 1273 K leads to more than doubled  $\dot{n}_{\text{C,syngas,RPC}}$  at the corresponding change in  $T_{\text{s,center,outlet}}$  of only ~40 K.

Figure 8-10 presents simulated radial profiles of temperature, steam mole fraction, and gasification rate at the mid-plane of the domain ( $z = 0.5 \text{ m}$ ) for  $T_{\text{wall}} = 1173$ , 1223, and 1273 K. As shown in Figure 8-10a, the solid temperature and its slope are highest at the tube wall and are seen to increase with an increase in wall temperature as expected. Conversely, the steam mole fraction, plotted in Figure 8-10b, is the highest in the tube center and decreases with an increase in wall temperature. These observations can be attributed to the exponential temperature dependence of the gasification rate and the slow radial dispersion of steam leading to the steep profiles of the gasification rate per unit volume ( $\dot{m}_{\text{C}}$ ) with the highest rates near the wall, see Figure 8-10c.

**Table 8-4:** Simulation results for a 1 m tall / 0.06 m inner diameter domain with  $d_{\text{nom}} = 2.54 \text{ mm}$ ,  $k_s = k_{\text{SiC}}$ ,  $\varphi_{\text{RPC}} = 89\%$ ,  $\dot{m}_{\text{f,in}} = 2 \text{ g/s}$ ,  $T_{\text{f,in}} = 873 \text{ K}$ , and  $l = 0.2$ .

wall temperature $T_{\text{wall}} [\text{K}]$	overall gasification rate $\dot{n}_{\text{C,syngas,RPC}} [\text{mmol/s}]$	average centerline temperature $\bar{T}_{\text{s,center}} [\text{K}]$
1173	27.0	1067
1223	42.0	1083
1273	58.9	1097



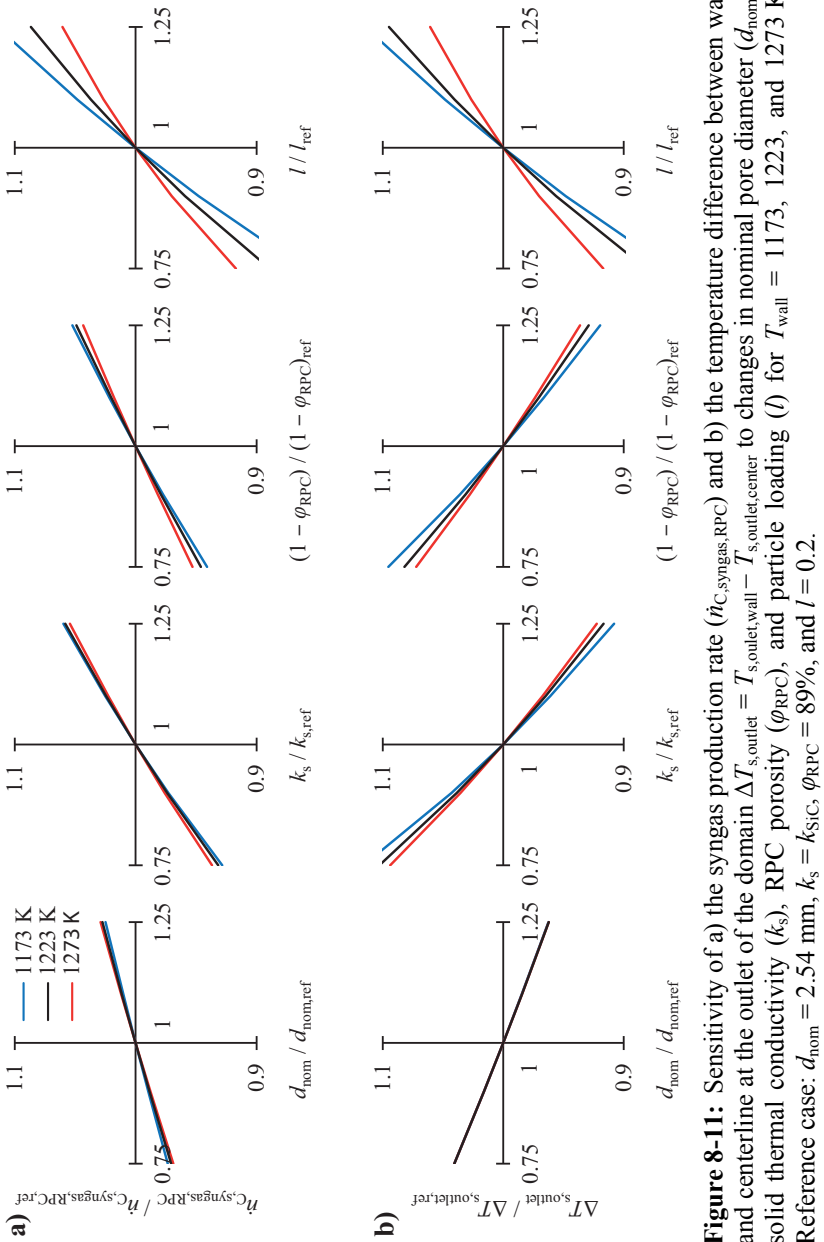
**Figure 8-10:** Simulated radial profiles of a) solid temperature, b) steam mole fraction, and c) gasification rate at  $z = 0.5$  m for  $l = 0.2$  and  $T_{\text{wall}} = 1173, 1223, \text{ and } 1273 \text{ K}$ .

Figure 8-11 shows the responses of the syngas production rate ( $\dot{n}_{C,\text{syngas,RPC}}$ ) and the temperatures at the outlet to changes in the particle loading ( $l$ ) and the RPC properties (pore diameter, solid thermal conductivity, and porosity) for three wall temperatures ( $T_{\text{wall}} = 1173, 1223, \text{ and } 1273 \text{ K}$ ). The changes are reported with respect to the reference conditions discussed above. Based on the results summarized in Figure 8-11a one could draw the following inferences relative to the responses of syngas production rate:

1. Increasing  $d_{\text{nom}}$  or  $k_s$  at fixed  $\varphi_{\text{RPC}}$  results in an increase in the effective thermal conductivity of the RPC ( $k_{\text{eff}}$ ) and thus an increase in the overall gasification rate. An increase in  $d_{\text{nom}}$  leads to an increase in the radiative contribution due to a decrease in the extinction coefficient, thus its effect is more pronounced at higher temperatures. Conversely, the changes in  $k_s$  have a larger influence at lower temperatures due to the larger contribution of the conduction heat transfer to the effective thermal conductivity of the structure.
2. An increase in the volume fraction of the RPC solid  $1-\varphi_{\text{RPC}}$  is reflected by an increase in  $k_{\text{cond}}$  (see Eq. 8.25) but impaired radiative heat transfer due to a higher extinction of radiation. The increase in  $1-\varphi_{\text{RPC}}$  is thus less beneficial at higher temperatures.
3. Of all the investigated parameters, the particle loading has the largest effect: a 25% increase in the particle loading leads to an increase in the overall gasification rate by 6%–11%. The increase is especially pronounced at lower temperatures where the temperatures and gasification rates are more uniform.

Figure 8-11b shows the responses of the temperatures at the outlet of the domain as the difference between wall and centerline temperatures  $\Delta T_{s,\text{outlet}} = T_{s,\text{outlet,wall}} - T_{s,\text{outlet,center}}$ . It can be observed that:

1. An increase in  $d_{\text{nom}}$ ,  $k_s$ , or  $1-\varphi_{\text{RPC}}$  results in a higher effective thermal conductivity and thus a decrease in  $\Delta T_{s,\text{outlet}}$ . As for the overall



gasification rate (Figure 8-11a), the sensitivity of  $\Delta T_{s,outlet}$  is lower to  $k_s$  and  $1-\varphi_{RPC}$  as the wall temperature increases. No wall-temperature dependence was observed for the sensitivity to  $d_{nom}$ .

2. An increase in the particle loading leads to an increase in  $\Delta T_{s,outlet}$  due to the reduced effective thermal conductivity and the increased consumption of heat of the gasification reaction. The sensitivity is larger at lower wall temperatures as the increase of the gasification rate is higher and more heat is consumed.

### 8.3.3 Numerical Comparison of the Trickle Bed to a Moving Bed

An alternative to the incorporation of a trickle bed into a drop tube for increasing the residence time of char would be to operate the gasifier as a moving bed of char particles (no RPC,  $l = 1$ ). To compare the performance of the trickle bed and the moving bed in terms of temperature profiles and overall char gasification rates, simulations were carried out for the same flow rates, domain size, grid density, and boundary conditions described in the previous section.

For simulation purposes, the moving bed was assumed to consist of uniformly sized char particles (mean particle size = 0.81 mm) and to have a porosity of  $\varphi_{MB} = 0.56$  [31]. As the temperature differences between the solid and fluid phase are expected to be even smaller than in the RPC trickle bed, the model has been reduced to a pseudo-homogeneous case, requiring only one energy equation to be solved. The effective thermal conductivity ( $k_{eff}$ ) was based on a Yagi and Kunii model [123] with fitting parameters from Piatkowski [31] and adjusted for the smaller particle size. The contribution of ash to the thermal conductivity was neglected. A more detailed description of the effective thermal conductivity model applied can be found in Appendix B.

The correlations for the diffusion and dispersion applied for the moving bed are the following [124, 125]:

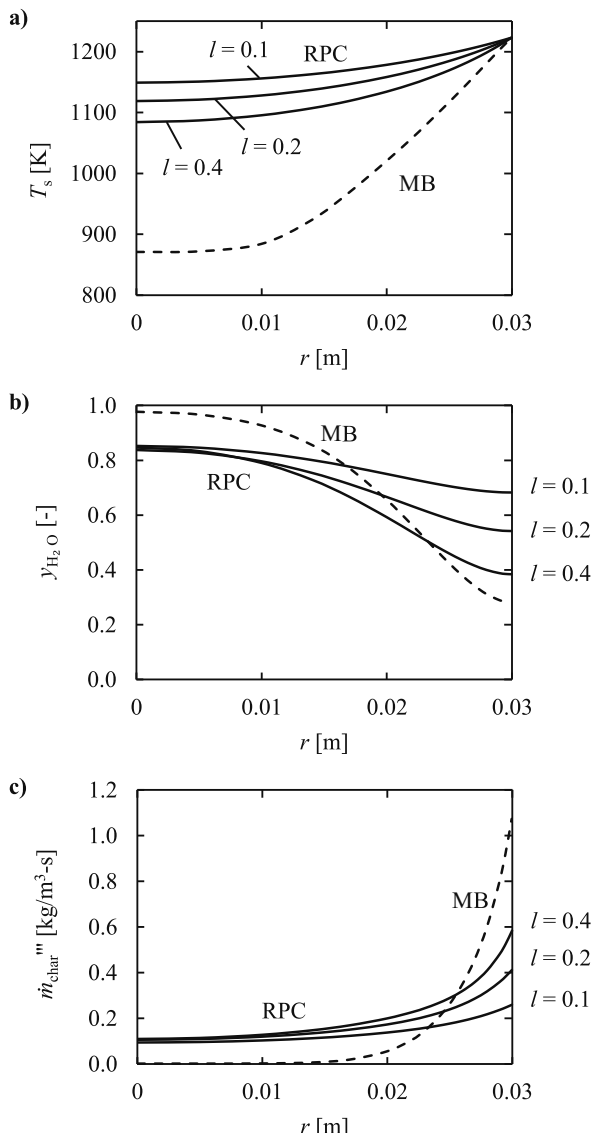
$$D_{\text{eff},k,\perp} = \frac{D_{m,k}\varphi}{\tau^2} + \frac{u_z d_p}{\text{Pe}_T(\infty)} \quad (8.31)$$

$$D_{\text{eff},k,\parallel} = \frac{D_{m,k}\varphi}{\tau^2} + \frac{u_z d_p}{\text{Pe}_L(\infty)} \quad (8.32)$$

where  $\text{Pe}_T(\infty) \approx 12$  and  $\text{Pe}_L(\infty) \approx 2$ . The tortuosity  $\tau$  of a randomly packed bed can be described by [126]

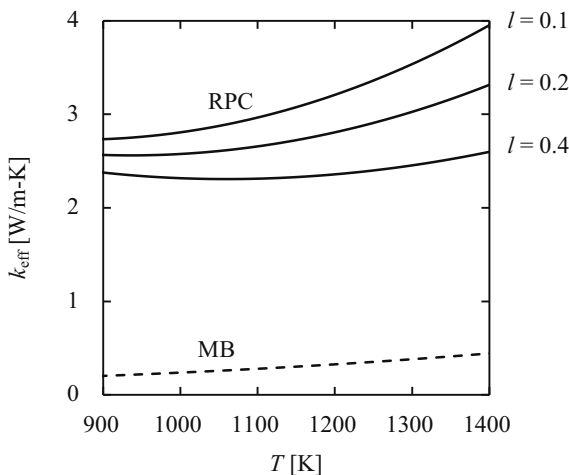
$$\tau^2 = \sqrt{2} \quad (8.33)$$

Figure 8-12 compares the moving bed (MB) and trickle bed (RPC) in terms of radial profiles of temperature, steam mole fraction, and gasification rate simulated for  $T_{\text{wall}} = 1223$  K at  $z = 0.5$  m. As compared to the moving bed, both the temperature and steam concentration profiles are more uniform across the RPC configurations operating at particle loadings  $l = 0.1\text{--}0.4$ , see Figures 8-12a and 8-12b. The steep temperature gradient in the moving bed close to the wall is also consistent with previously discussed effect of particle loading. The steam mole fraction at the wall decreases with an increase in the particle loading thus it is the lowest for the moving bed. At the centerline of the moving bed, the steam concentration does not differ considerably from the one at the inlet. Due to the low core temperatures in the moving bed, the gasification rate, plotted in Figure 8-12c, approaches zero at about one third of the radius from the wall ( $\sim 0.01$  m) so the steam passes through unreacted. Conversely, the reaction within the RPC is more uniformly distributed and proceeds at a noticeable rate even in the center. The gasification rates in the regions closer to the wall increase with particle loading as more char is exposed to the highest temperatures. Therefore, the moving bed exhibited higher gasification rates at the wall than the trickle bed.



**Figure 8-12:** Simulated radial profiles of a) solid temperature ( $T_s$ ), b) steam mole fraction ( $y_{H_2O}$ ), and c) gasification rate ( $\dot{m}_{char}'''$ ) in moving bed (MB) and RPC ( $l = 0.1, 0.2$ , and  $0.4$ ) at  $z = 0.5$  m for  $T_{wall} = 1223$  K.

The higher core temperatures and reaction rates of the RPC configuration can be attributed to the heat transfer enhancement brought in by the conduction through the RPC material and deeper penetration of radiation through the RPC pores. Figure 8-13 compares the effective thermal conductivities of the moving bed with N<sub>2</sub>-filled voids and the RPC with different particle loadings. The presence of the RPC is seen to significantly increase the effective thermal conductivity of the domain. At lower temperatures and a particle loading of 0.4, a decrease in the effective thermal conductivity with increasing temperature is observed. This is due to a decrease of the conductivity of the RPC material ( $k_s$ ). At lower particle loadings and higher temperatures the radiative contribution dominates resulting in a higher effective thermal conductivity. At higher temperatures the radiative contribution increases which leads to a higher effective thermal conductivity. This is illustrated in Figure 8-14. The contribution of the radiation increases from about 20% at 900 K to around 60% at 1400 K. Increased loadings result in a lower contribution of radiation as the voids get smaller and thus lower effective thermal conductivity.



**Figure 8-13:** Effective thermal conductivity ( $k_{\text{eff}}$ ) over temperature for the moving bed (MB) with N<sub>2</sub> filled voids and the RPC configuration at various loadings ( $l$ ).

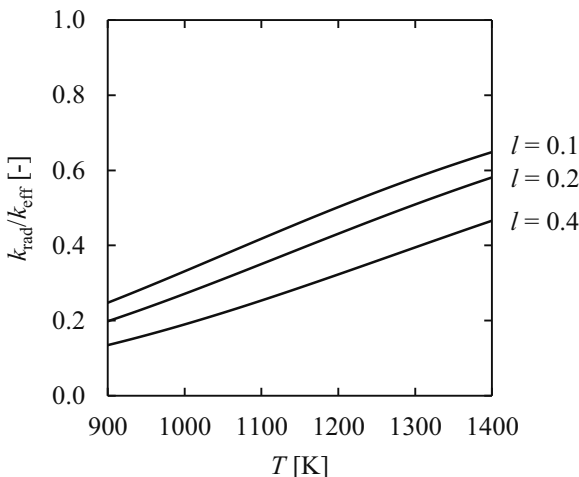


**Figure 8-14:** Contribution of radiation term  $k_{\text{rad}}$  on the effective thermal conductivity  $k_{\text{eff}}$  for RPC configuration.

Figure 8-15 compares the overall gasification rates at  $T_{\text{wall}} = 1173$ ,  $1223$ , and  $1273$  K calculated for the moving bed ( $\dot{n}_{\text{C,syngas,MB}}$ ) and the trickle bed ( $\dot{n}_{\text{C,syngas,RPC}}$ ) operating at various particle loadings ( $l$ ). At low particle loadings, the overall gasification rate of the trickle bed is lower than in the moving bed, as less reacting material is present in the reactor. With an increase in the particle loading in the RPC, the ratio of trickle-bed to moving-bed gasification rates increases rapidly at first and then flattens. The steep increase at low particle loadings is almost linear with the particle loading. The flattening at higher particle loadings occurs due to the reduction in radiative contribution and reduced steam concentrations close to the wall. At wall temperatures of  $1173$  and  $1273$  K, the trickle bed outperforms the moving bed above particle loadings of  $0.18$  and  $0.32$ , respectively. At  $T_{\text{wall}} = 1273$  K, the trickle bed with  $l = 0.5$  gasifies  $\sim 25\%$  more carbon than the moving bed containing twice as much char.

Even though the gasification rates at low particle loadings are lower than in the moving bed, an RPC might be preferred as the higher core temperatures favor the decomposition of volatile hydrocarbons passing through this zone,

thereby improving the syngas quality. This is especially important when using feedstocks that release high amounts of hydrocarbons and tars.

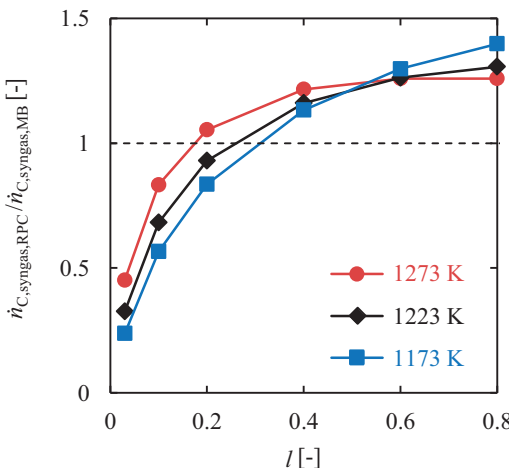


**Figure 8-15:** Simulation results for ratio of trickle-bed to moving-bed gasification rates as function of the particle loading in the RPC ( $l$ ) and wall temperatures of  $T_{\text{wall}} = 1173, 1223$ , and  $1273$  K.

## 8.4 Conclusions

A gas-solid trickle-bed reactor for the gasification of beech char particles was evaluated experimentally and numerically. Efficient delivery of externally supplied concentrated solar heat to the reaction site was achieved by incorporating a high conductivity RPC as packing into a drop-tube reactor that increased the residence time of the solids and enhanced the heat transfer to the gas phase. A series of 43–51 min gasification experiments in the temperature range 1173–1273 K with a mass flux of  $6.5 \text{ g/s}\cdot\text{m}^2$  was conducted with no pressure increase or clogging over the duration of the experiments. Compared to the drop-tube configuration, the carbon conversions attained under same conditions in the trickle-bed were significantly higher (< 1% versus 52%).

A two-dimensional finite-volume model of the trickle-bed reactor including chemical reaction coupled with conduction, convection, and radiation of heat within the porous structure was developed. Its predictions were in good agreement with measured reactor temperatures and gasification rates. A sensitivity analysis of the overall gasification rate and the core temperature, the key parameters for the capacity and gas phase selectivity, indicated that any effort to increase the effective thermal conductivity is beneficial. Reduced particle loadings increase the core temperatures but result in lower gasification rates.

A numerical comparison with a moving bed of char particles showed a more uniform temperature distribution over the cross-section of the trickle-bed. This is attributed to both high conductivity of the RPC and suppressed extinction of the radiation due to higher open porosity of the trickle-bed. The more uniform temperatures and thus the higher core temperatures are expected to improve gas-phase selectivity towards the desired product gas. Furthermore, it was shown that the gasification rates of the proposed configuration exceed those of a moving bed for particle loadings higher than 32% for a wall temperature of 1173 K and 18% for 1273 K, respectively.

# **Chapter 9**

## **Overall Conclusions and Outlook**

This thesis was performed in the framework of a joint project of the Universidade de São Paulo, Brazil and ETH Zürich, Switzerland. It investigates the thermochemical steam-gasification of biomass using concentrated solar energy for process heat. The product of the gasification is carbon neutral synthesis gas, a mixture of hydrogen and carbon monoxide. The synthesis gas produced can be catalytically converted to gaseous or liquid hydrocarbon fuels, e.g. to H<sub>2</sub> via water-gas shift reaction, to diesel or kerosene via Fischer-Tropsch synthesis, or to methanol and then gasoline via the methanol-to-gasoline process (Mobil). The syngas may also be used directly for power generation by combusting it in a turbine or an internal combustion engine. Further uses include the production of valuable chemicals.

### **9.1 Thermodynamics and Kinetics**

Thermodynamic equilibrium compositions were calculated for the autothermal oxygen/steam gasification and the solar-driven steam gasification of Brazilian sugarcane bagasse to assess the differences in the syngas quality. For the solar gasification, an almost full conversion to H<sub>2</sub> and CO is achieved at 1 bar and 1350 K. Higher temperatures are therefore worthwhile only if the reaction rates are accelerated and the thermal losses of the process can be reduced. Compared to the autothermal gasification, the solar syngas shows a superior quality with a higher H<sub>2</sub>/CO ratio (1.16 vs. 1.07) and less dilution with CO<sub>2</sub> (0.2%<sub>vol</sub> vs. 12%<sub>vol</sub>).

First and second law analyses were conducted comparing the autothermal to the solar gasification in order to determine their performance, to find the maximum energy and exergy conversion efficiencies, and to identify the major sources of irreversibility. Theoretical upgrade factors (ratio of heating value of syngas produced over that of the feedstock) of 1.26 and lower heating values of 19.4 MJ/kg can be achieved by the solar gasification, whereas the autothermal pathway achieves only an upgrade factor of 0.95 and a lower heating value of 13.9 MJ/kg. The autothermal gasification requires about 25% of the bagasse to be combusted to provide the reaction enthalpy for the endothermic gasification reactions. Thereby, the amount of H<sub>2</sub>O consumed per unit feedstock in a stoichiometric gasification is also reduced by 25% compared to the solar-driven process. In the solar-driven process all feedstock is utilized. Moreover, the feedstock is upgraded by 26% while chemically storing the solar energy at a solar to chemical efficiency of 66%. In comparison to autothermal gasification, the syngas composition is more suitable for the synthesis of liquid fuels. Further, the possible treatment of feedstock with higher moisture content and the elimination of the air separation unit, support the potential benefits of solar-driven gasification.

The gasification rates of the biomass with steam and the resulting residence time requirements play an important role in terms of efficiency of a solar reactor and are crucial its design. Therefore, the kinetics of the rate limiting steam gasification step of pyrolyzed bagasse particles were experimentally studied by thermogravimetric analysis in the temperature range of 1173–1473 K and steam concentrations of 25–75%<sub>vol</sub>. A kinetic rate law based on the oxygen exchange mechanism and a linear decrease of the effective char surface area with conversion was found to fit the experimental data well. The required residence time for 90% char conversion at a steam concentration of 75%<sub>vol</sub> was predicted to be 16 s at a reactor temperature of 1573 K and 43 s at 1373 K, a temperature that would allow the use of thermal shock resistant metal alloys for the construction of a solar reactor.

## 9.2 Reactor Design and Testing

In a next step, a two-zone solar reactor concept for the gasification of the highly volatile bagasse was proposed. By combining drop-tube with fixed-bed concepts, the proposed two-zone laboratory-scale reactor provided sufficient solids residence time for adequate char conversion and temperatures high enough for the decomposition of the other pyrolysis products such as tar and gaseous hydrocarbons.

Experimental testing in the temperature range of 1073–1573 K was done by exposing the tubular reactor to infrared radiation from an electric furnace, thereby simulating the conditions present in an absorbing solar cavity receiver. The preliminary results, in particular the carbon conversion and the decomposition of CH<sub>4</sub>, stayed behind the expectations, which implied that further development was necessary. CH<sub>4</sub> was detected in significant amounts over the whole temperature range investigated even though its presence was not predicted by thermodynamic equilibrium at above 1200 K. Further, it was seen that ash melting, which occurred at temperatures above 1473 K, gives an upper limit to the operating temperatures of the reactor concept. It could however be confirmed that an upgrade factor of greater than 1 is attainable and that syngas yields per unit feedstock as well as the heating values of the syngas are significantly higher than those typically obtained in autothermal gasifiers.

Based on the experience gained with the prototype reactor, the concept was further developed to achieve higher the carbon conversion and a better decomposition of the gaseous hydrocarbons. Moreover, a 1.5 kW<sub>th</sub> solar-driven biomass gasifier consisting of a cavity-type receiver housing a tubular reactor has been developed and evaluated with bagasse particles under simulated high flux solar radiation. The two-zone reactor comprises a drop-tube for fast pyrolysis and a trickle bed for the char gasification and decomposition of the pyrolysis products. The drop-tube zone ensures efficient radiative heat transfer to the dispersed biomass particles that is required for their fast pyrolysis. The trickle-bed zone consists of a structured packing made of reticulate porous ceramic (RPC), that allows controlling the overall porosity of the gasification zone in order to increase the residence time of the char particles while still

allowing the radiation to penetrate through. Thereby, it provides residence time and temperature needed for the rate limiting char gasification and the decomposition of the pyrolysis products.

The comparison with a drop-tube configuration demonstrated that the two-zone reactor concept decomposes CH<sub>4</sub> and C<sub>2</sub>-hydrocarbons more efficiently. Again, the syngas produced showed higher LHV's than common in autothermal gasification. Moreover, the carbon conversion was significantly higher than in the drop-tube configuration. The biomass was energetically upgraded by 5%, effectively storing solar energy in the syngas. The maximum energy conversion efficiency was 21%.

An energy flow analysis of the solar reactor identified the largest losses as conduction through the cavity walls and along the reactor tube. Only 10% of the input power was transferred to the reactants. The largest efficiency gains are thus expected by increasing the throughput of the gasifier.

### 9.3 Modeling

The heat transfer in the trickle-bed zone of the two-zone solar reactor was studied using an externally heated gas-solid trickle-bed reactor with a RPC packing. Experimental testing with beech char particles was performed in the temperature range 1173–1273 K with a mass flux of 6.5 g/s·m<sup>2</sup>. In the 43–51 min long experiments neither a pressure increase nor clogging of the RPC were observed. The achieved carbon conversions were significantly higher than for the drop-tube configuration (< 1% vs. 52%).

The predictions of reactor temperatures and gasification rates of a two-dimensional finite volume heat and mass transfer model of the reactor including chemical reaction and heat transfer within the porous structure agreed well with the experimental measurements. A sensitivity analysis indicated that any effort to increase the effective thermal conductivity of the trickle bed is beneficial for the reactor temperature and the gasification capacity. Furthermore, a numerical comparison with a moving-bed reactor demonstrated that the increased heat transfer via combined radiation and conduction through the porous RPC leads

to a more uniform temperature distribution and more uniform steam concentrations across the reactor. As a result, higher core temperatures and gasification rates than in a moving bed are achieved, the higher temperatures being beneficial for the decomposition of pyrolysis products.

## 9.4 Outlook

Future research should focus on the following main experimental and numerical topics:

- long term operation
- online ash removal strategies
- increase of throughput
- heat and mass transfer of various packings
- feeding of moist feedstock
- chemical processes that could use the same reactor concept

So far the steam gasification experiments were only conducted under the very limited conditions of both short-term operation (less than an hour) and at light particle loadings. As the goal for solar reactors is operate continuously, daily at least from sunrise to sunset, long term experiments should be performed to study the industrial feasibility of the concept. Testing should be done with a variety of feedstocks, particle sizes, and feedstock preparation methods.

In conjunction with the long term experiments, the deposition of ash will become a more pronounced issue. Therefore, the feedstocks investigated should preferably have a high ash slagging temperature as this gives an upper limit to the allowable operating temperatures. Moreover, time should be dedicated on investigating online ash removal options, such as periodic inert or product gas purge, gas pulses, or vibration of the packing.

It was seen that the throughput of the solar reactor is critical to its efficiency. An increase in the throughput requires the knowledge and control of the solids residence time distribution. Therefore, the maximum solids feeding

rates should be found for the different feedstocks, particle sizes, and preparation methods. Further, methods to increase the feeding rates should be explored. These may include the previously mentioned gas pulses or the vibration of the packing but should also include alternative packing properties and designs that go beyond ceramic foams. As the heat and mass transfer are critical for the throughput of the reactor, alternative packings should therefore be designed with that in mind.

The two zones of the gasifier concept should be studied in more depth. This is best achieved by individually studying the pyrolysis and the gasification zone. By doing so, experimental measurements are not impaired by the presence of the other zone. Prior to scaling-up to a multi-tube design, it is important to test and improve the throughput of a single tube by using a taller reactor with a larger hot zone. The current solar reactor has a roughly 120 mm long high temperature pyrolysis zone and an 80 mm tall trickle bed zone. An extension of the pyrolysis zone might allow the operation with moist feedstock as there would be sufficient residence time to evaporate the water and pyrolyze the particles before reaching the trickle bed. The operation with wet feedstock would reduce the effort and energy needed for the feedstock preparation and might thus be beneficial for the economics of a solar gasification system. Further, an increase in the height of the trickle-bed zone would increase the gas and solid residence times and is thus expected to improve the char conversion and the decomposition of the other pyrolysis products.

The reactor concept that has been developed is not only applicable for the gasification of biomass and other carbonaceous feedstock. It is thus important to also consider different high temperature gas-solid reactions that might benefit from the proposed designs and conclusions of this work.

## **Appendix A:**

### **Solar Gasification of Microalgae in a Drop-Tube**

This chapter is an excursion from the previously described two-zone reactor concept. The feedstock under consideration is microalgae (*chlorella vulgaris*). Microalgae are unicellular photosynthetic micro-organisms that can grow in practically any aquatic environment, from freshwater, sea water to even waste water. They need a carbon source, which is usually CO<sub>2</sub>, nutrients, and light, and grow 10 to 100 times faster than terrestrial plants [127], and are thus considered as a potential feedstock for the large scale production of biofuels. They can be cultivated on land that is unsuitable for agriculture or forestry and therefore do not compromise production of food, fodder and other crop-derived products. Further, the production yield per unit area is higher than for other biofuel sources.

Microalgae are commonly grown in open pond or closed photobioreactors, both of which have their merits. Open pond systems are shallow round or raceway-style ponds that are mixed with gas bubbling through the growth medium or with paddle wheels, respectively. They are relatively cheap to build and to operate but suffer from high water consumption due to uncontrolled evaporation, the risk of contamination and changes in the environment (wind, rain, temperature fluctuations). Tubular or flat plate photobioreactors have high productivities due to their well-controlled and easy to maintain operational conditions. The requirements for make-up water are small. As there is no evaporative cooling, temperature control is necessary. Gas exchange is the limiting factor for their scalability. [128]

Apart from the growth of the microalgae, harvesting and dewatering are the main challenges as they are very energy intensive due to the microalgae's high water content. One liter of ready to harvest growth medium contains only about 1–2 g (dry weight) microalgae. Commonly suggested harvesting methods, such

as sedimentation (~98.5%<sub>wt</sub> water), centrifugation (~80%<sub>wt</sub> water), filtration (~80%<sub>wt</sub> water), and flocculation, do not reduce the water content significantly and are often highly energy- or chemical-intensive. Further reducing the water content requires thermal drying, e.g. flash drying, spray drying, sun drying, or drying in rotary dryers. [129, 130]

Several routes for the conversion of microalgae into valuable products such as chemicals and versatile fuels are considered in the US DOE's algal biofuels roadmap [131]. One of them is the gasification of microalgae. Most conventional autothermal gasification systems use dry biomass with a moisture content of 10%<sub>wt</sub> to 20%<sub>wt</sub>. Higher moisture contents are feasible in certain reactor types but result in significantly reduced energy efficiency as for every kilogram of moisture in the feedstock, a minimum of 2260 kJ of additional non-recoverable energy from the gasifier has to be provided to vaporize the water [14]. Thermal drying of the feedstock prior to gasifying it is often times preferred as this is more efficient than evaporating the moisture in the gasifier and can simplify its handling. For solar-driven gasification a moisture content of about 25%<sub>wt</sub> represents the stoichiometric amount of water for the steam gasification of microalgae to H<sub>2</sub> and CO. A slight over-stoichiometry might be beneficial for the reaction kinetics. Larger amounts of excess moisture reduce the efficiency in the same way as in the conventional gasification.

In this work, the steam gasification of dry microalgae was investigated in a 1.5 kW indirectly-heated solar entrained flow gasifier consisting of an absorbing cavity receiver housing a tubular reactor was experimentally examined at ETH's high flux solar simulator. The influence of different steam concentrations on the composition and the heating value of the syngas, the carbon conversion, the energetic upgrade, and on the reactor efficiency was evaluated.

## A.1 Materials



**Figure A-1:** Spray dried microalgae (*chlorella vulgaris*).

The microalgae used in this work are depicted in Figure A-1. They are a *chlorella vulgaris* species that were produced in a tubular photobioreactor and then spray-dried (Roquette, Klötze GmbH & Co. KG). The physical and chemical properties given in Table A-1 were determined as described for the bagasse and beech char in Section 3.3. Before all experiments and analyses the microalgae were dried in a convection oven for at least 4 h at 378 K.

**Table A-1:** Physical and chemical properties of dry microalgae: Ultimate and proximate analyses, heating value and mean particle size.

microalgae ( <i>chlorella vulgaris</i> )		
carbon (C)	[% <sub>wt</sub> ]	48.8
hydrogen (H)	[% <sub>wt</sub> ]	6.5
oxygen (O)	[% <sub>wt</sub> ]	30.7
nitrogen (N)	[% <sub>wt</sub> ]	8.0
sulfur (S)	[% <sub>wt</sub> ]	0.6
H/C = $x$	[mol/mol]	1.597
O/C = $y$	[mol/mol]	0.472
volatiles	[% <sub>wt</sub> ]	76.2
fixed carbon	[% <sub>wt</sub> ]	19.5
ash	[% <sub>wt</sub> ]	4.3
LHV	[MJ/kg]	19.71
$\bar{d}_p$	[μm]	59

The elemental analysis revealed an average chemical formula of  $\text{CH}_{1.597}\text{O}_{0.472}$  on a dry and ash free basis. The nitrogen content was 8%<sub>wt</sub>, which is significantly higher than in the bagasse or the beech char and should therefore not be neglected when analyzing the product gas as the release of the nitrogen during gasification might be measurable.

The particle size distribution of the microalgae is shown in Figure A-2. They had a mean particle size of 59  $\mu\text{m}$ , which is about an order of magnitude smaller than for the previously investigated feedstocks.

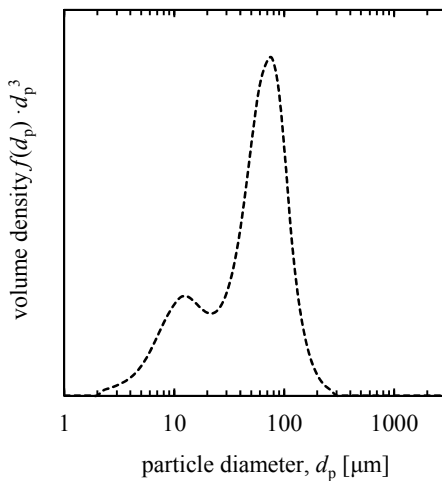


**Figure A-2:** Particle size distribution of spray-dried microalgae analyzed with LA-950 analyzer (HORIBA).

## A.2 Experimental Setup

The smaller particle size of the microalgae compared to the bagasse previously investigated was expected to reduce the required residence times for high carbon conversions significantly. This might allow achieving high conversions even without the built-in RPC. Moreover, the ash melting temperature of the microalgae was found to be around 1273 K, so about 200 K lower than for the bagasse, making them unsuitable for gasification using the RPC packing.

The existing 1.5 kW solar gasifier used for the bagasse gasification experiments was thus modified to an indirectly-irradiated solar drop-tube gasifier, similar to the concept investigated by Lichy et al. [38]. The solar reactor and the peripheral components used for the gasification of microalgae are schematically shown in Figure A-3. The solar reactor is identical to the one

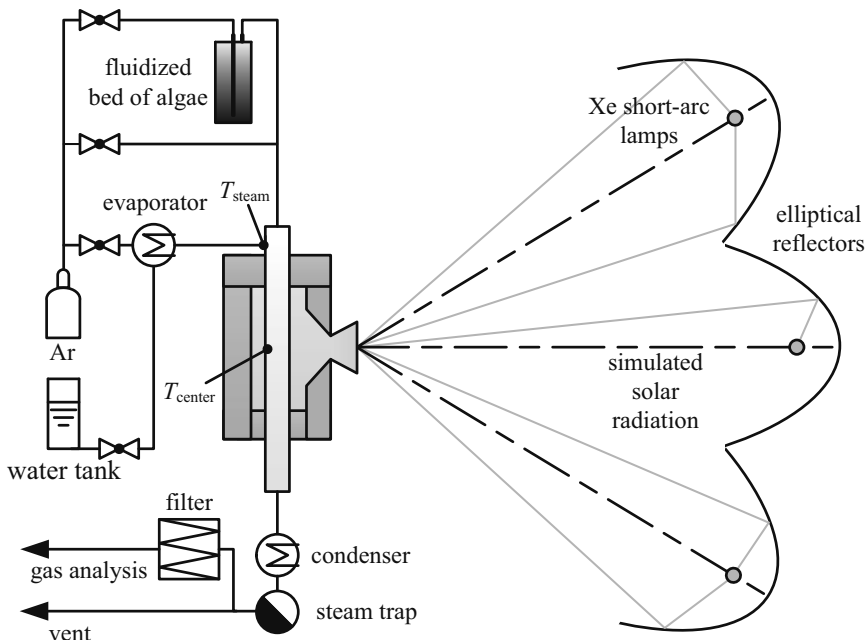


**Figure A-3:** Schematic of the solar entrained flow gasifier including solar simulator and the primary components and flows.

described in Section 7.2.1 except that no RPC and no supporting tube were installed in the reactor tube.

At the top of the reactor tube, dry microalgae are introduced as an aerosol flow from an Ar fluidized bed feeder. Microalgae feeding rates are controlled by adjusting the bypass flow of the fluidized bed keeping the total flow rate through the aerosol inlet constant. Below the aerosol inlet Ar and steam are injected through annularly distributed inlets. The steam is generated with an external evaporator (Bronkhorst) and is superheated in an electrically heated tube connecting the evaporator with the inlet. The flow rates of the inlet gases and water into the evaporator are controlled with electronic mass flow controllers (Bronkhorst). Temperature measurements were done with K-type thermocouples placed at the steam inlet ( $T_{\text{steam}}$ ) and inside the reactor tube at the back side at the height of the aperture ( $T_{\text{center}}$ ).

The particles entrained in the flow travel down the hot reactor tube, absorb radiation from the tube, undergo rapid pyrolysis, and gasify in the steam. Tar and gases released during the pyrolysis pass through the hottest zone of the reactor and get at least partially decomposed. At the bottom of the reactor a stream of the product gas is withdrawn, chilled, and filtered to remove condensable components and particulate matter. The stream is then analyzed by gas chromatography (Micro-GC, Varian 490 with Molsieve-5A and Poraplot-U columns, 1/120 Hz sampling frequency, calibrated for H<sub>2</sub>, N<sub>2</sub>, CO, CH<sub>4</sub>, CO<sub>2</sub>, C<sub>2</sub>H<sub>2</sub>, C<sub>2</sub>H<sub>4</sub>, and C<sub>2</sub>H<sub>6</sub>), infrared-based detectors for CO, CO<sub>2</sub> and CH<sub>4</sub> (Ultramat, Siemens), and a thermal conductivity based detector for H<sub>2</sub> (Calomat 6, Siemens).

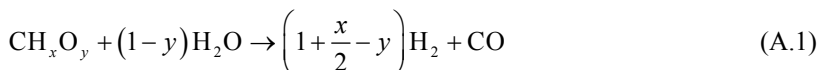
Experimentation was done on ETH's high-flux solar simulator using up to 6 out of the 7 high-pressure Xe arcs lamps installed in elliptical reflectors. A detailed description is given in Section 7.2.1.

### A.3 Experimental Procedures

Before starting an experiment, the reactor was purged with Ar and tested for leaks to ensure an O<sub>2</sub> free environment. Up to 6 lamps of the solar simulator

were then turned on to irradiate the reactor at power levels of up to approximately  $\dot{Q}_{\text{solar}} = 2 \text{ kW}$  (at the cavity aperture) to achieve rapid heating. Once the desired reactor temperatures were reached the flow rates of the different gas streams were set and the power level was reduced to approximately  $\dot{Q}_{\text{solar}} = 1.2 \text{ kW}$  to equilibrate the temperatures in the reactor. The reactor temperature ( $T_{\text{center}}$ ) was controlled to around 1430 K for all experiments. Three different inlet gas compositions were investigated keeping total volumetric flow rate of Ar and steam entering the reactor constant in all experiments. The Ar flow through the aerosol inlet was set to 2.5 L<sub>N</sub>/min<sup>a</sup> and the combined steam and Ar flow through steam inlet to 2.3 L<sub>N</sub>/min. The steam flow rate was 0, 61 and 86 g/h resulting in an overall steam concentration of 0%<sub>vol</sub>, 27%<sub>vol</sub>, and 37%<sub>vol</sub>. The temperature of the gas entering through the steam inlet  $T_{\text{steam}}$  was around 510 K.

After temperature equilibration, microalgae (CH<sub>1.597</sub>O<sub>0.472</sub>) were fed for 15 min at an average feeding rate of 0.33 g/min (0.24–0.40 g/min) or a mass flux of 4.2 g/s·m<sup>2</sup>. This led to molar steam to biomass ratios ( $\dot{n}_{\text{H}_2\text{O(g)}}/\dot{n}_{\text{CH}_x\text{O}}$ ) for the three different steam concentrations of 0, 4.5, and 6.3. This corresponded to 0, 8.5, and 12 times the stoichiometric amount of steam for the overall net reaction given by



Based on the gas composition measured the total outlet flow rates were determined and integrated over time. To capture also the product gas that is still in the reactor after switching off the feeding the integration included an additional 5 min after shutdown. The instantaneous concentrations of the C<sub>2</sub>-gases, only measured by GC, are computed based on the C<sub>2</sub>H<sub>x</sub>/CO ratio measured by the GC and the CO concentration measured by the infrared-based detectors. This is justified due to the rather constant C<sub>2</sub>H<sub>x</sub>/CO ratio over the duration of the individual experimental runs.

---

<sup>a</sup> L<sub>N</sub> designates normal liters at 273 K and 1 atm.

#### A.4 Results

A typical experimental run is depicted in Figure A-4 showing the molar flow rates of the major product gases. Shortly after the biomass feed is turned on (0 min), a steep rise in the syngas production was observed. The lag between the start of the feeding and the observed increase in the product gas flow rates was caused by the distance the gas had to travel to reach the measurement unit. At the end of the experiment the syngas flow rates dropped steeply. The variations of the flow rates originated from unintended fluctuations of the microalgae feeding rate.

A total of 10 experiments under the three previously specified conditions were carried out. A summary of the experimental results is given in Table A-2. The reported mole fractions are averages over all replicates that were calculated considering only molar flow rates of the product gases integrated over the course of each individual experiment; the flow rates of  $H_2O$  and Ar were not considered. LHV, upgrade factor ( $U$ ), and the carbon conversion ( $X_C$ ) were calculated as defined in Eqs. 6.2–6.4 for each individual experiment and then averaged over all replicates.

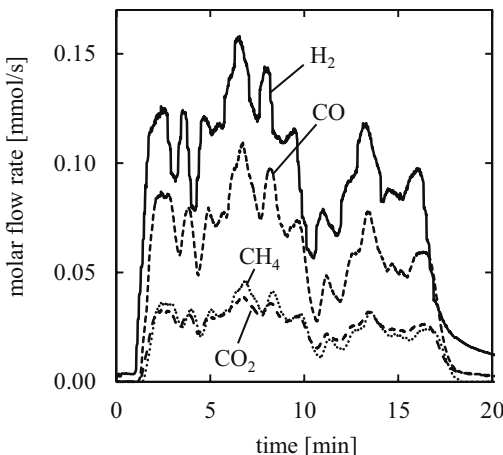


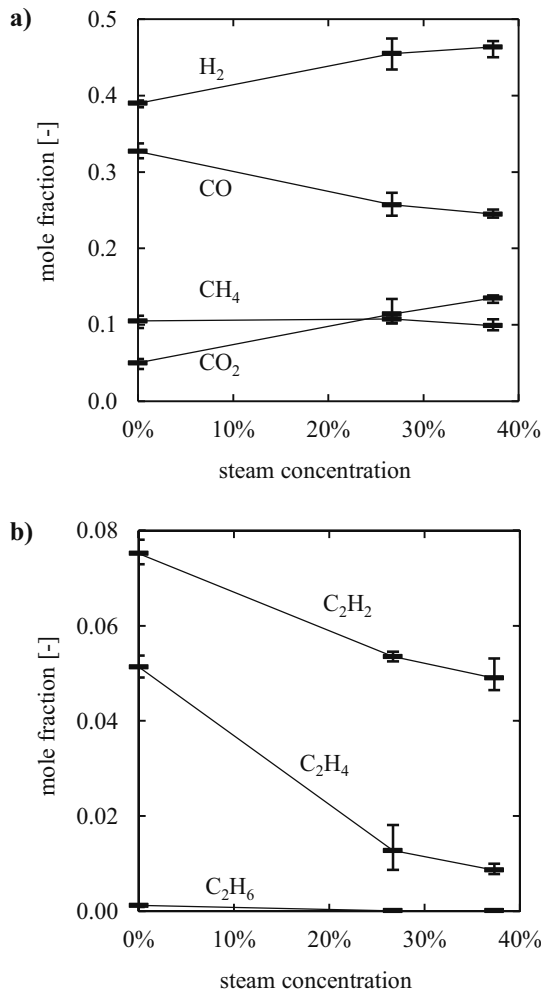
**Figure A-4:** Molar flow rate of the product gases during a typical experiment.

**Table A-2:** Summary of the experimental results (integral values averaged over all replicates).

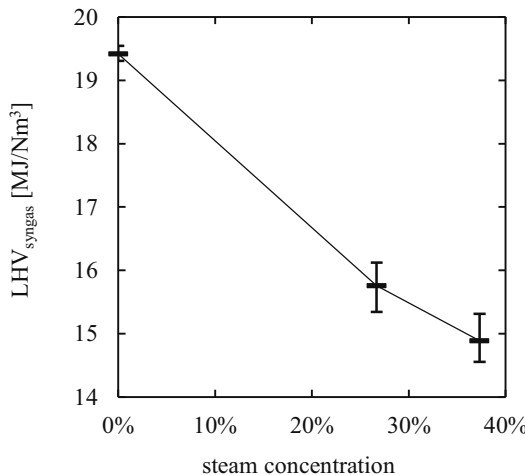
number of experiments		pure pyrolysis (0% <sub>vol</sub> steam)	27% <sub>vol</sub> steam	37% <sub>vol</sub> steam
		3	4	3
$y_{\text{H}_2}$	[% <sub>vol</sub> ]	39.0	45.5	46.4
$y_{\text{CO}}$	[% <sub>vol</sub> ]	32.7	25.7	24.5
$y_{\text{CH}_4}$	[% <sub>vol</sub> ]	10.5	10.8	9.9
$y_{\text{CO}_2}$	[% <sub>vol</sub> ]	5.0	11.4	13.5
$y_{\text{C}_2\text{H}_2}$	[% <sub>vol</sub> ]	7.5	5.4	4.9
$y_{\text{C}_2\text{H}_4}$	[% <sub>vol</sub> ]	5.1	1.3	0.9
$y_{\text{C}_2\text{H}_6}$	[% <sub>vol</sub> ]	0.1	0.0	0.0
$y_{\text{H}_2}/y_{\text{CO}}$	[ $-$ ]	1.19	1.77	1.89
$y_{\text{CO}_2}/y_{\text{CO}}$	[ $-$ ]	0.15	0.44	0.55
$T_{\text{tube}}$	[K]	1432	1425	1428
LHV <sub>syngas</sub>	[MJ/Nm <sup>3</sup> ]	19.4	15.8	14.9
$U$	[ $-$ ]	1.02	1.05	1.06
$X_{\text{C}}$	[ $-$ ]	0.45	0.53	0.61

Figure A-5 shows the product gas compositions for the different steam concentrations. Changing the steam concentration at the inlet from 0%<sub>vol</sub> to 37%<sub>vol</sub>, has a significant influence on the product gas composition. An increase in the concentrations of H<sub>2</sub> (39.0%<sub>vol</sub> to 46.4%<sub>vol</sub>) and CO<sub>2</sub> (5.0%<sub>vol</sub> to 13.5%<sub>vol</sub>) and a decrease of CO (32.7%<sub>vol</sub> to 24.5%<sub>vol</sub>), C<sub>2</sub>H<sub>2</sub> (7.5%<sub>vol</sub> to 4.9%<sub>vol</sub>) and C<sub>2</sub>H<sub>4</sub> (5.1%<sub>vol</sub> to 0.9%<sub>vol</sub>) were observed. CH<sub>4</sub> concentrations (10.5%<sub>vol</sub> to 9.9%<sub>vol</sub>) were hardly influenced by the presence of steam. The amount of C<sub>2</sub>H<sub>6</sub> was negligible under all conditions. The change in composition is caused by more water gas shift reaction and a better decomposition of hydrocarbons. This is also reflected by the increase in H<sub>2</sub>/CO ration (1.19 to 1.89) and CO<sub>2</sub>/CO ratio (0.15 to 0.55).

The LHV of the product gas is shown in Figure A-6. It reduces with increasing steam concentration from 19.4 MJ/Nm<sup>3</sup> for pure pyrolysis to 14.9 MJ/Nm<sup>3</sup> at a steam concentration of 37%<sub>vol</sub>. The lower values for higher



**Figure A-5:** Product gas compositions for different volumetric steam concentrations. Error bars indicate the span between the minimum and maximum values.



**Figure A-6:** LHV<sub>syngas</sub> for different volumetric steam concentrations. Error bars indicate the span between the minimum and maximum values.

steam concentrations are due to a greater extent of the water gas shift reaction and a better decomposition of C<sub>2</sub>H<sub>2</sub> and C<sub>2</sub>H<sub>4</sub>. The heating values found are significantly higher values than the 9.9–11.3 MJ/Nm<sup>3</sup> found by Hirano et al. [132] for the gasification of microalgae. They are also substantially higher than what is typically achieved by conventional autothermal biomass gasification.

The carbon conversion ( $X_C$ ) plotted in Figure A-7 was between 45% and 61%. A significant improvement for higher steam concentrations could be observed. This is caused by a reduction in the amount of tar not being converted as well as char gasification. Higher carbon conversions are expected to be achieved by increasing the length of the hot zone.

The upgrade factor ( $U$ ) was greater than 1 for all investigated conditions meaning that the biomass could be energetically upgraded and solar energy chemically stored in the syngas. Further, an increase of the upgrade factor with the steam concentration from 1.02 for the pure pyrolysis case to 1.06 for a steam concentration of 37%<sub>vol</sub> could be observed.

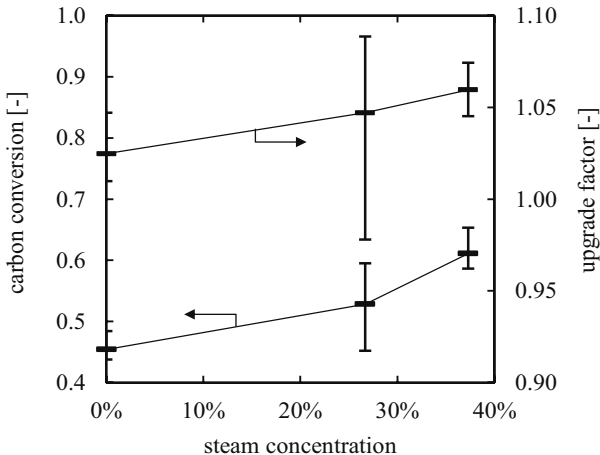


**Figure A-7:** Carbon conversion and upgrade factor for different volumetric steam concentrations. Error bars indicate the span between the minimum and maximum values.

The efficiency of the solar reactor is defined as

$$\eta = \frac{m_{\text{syngas}} \text{LHV}_{\text{syngas}}}{\int_{t_0}^{t_{\text{end}}} \dot{Q}_{\text{solar}} dt + m_{\text{algae}} \text{LHV}_{\text{algae}} - m_{\text{C,in}} (1 - X_C) \text{LHV}_{\text{char}}} \quad (\text{A.2})$$

where  $\dot{Q}_{\text{solar}} = 1.2 \text{ kW}$ ,  $m_{\text{syngas}}$  is the total mass of syngas produced,  $m_{\text{algae}}$  is the total mass of algae fed, and  $m_{\text{C,in}}$  is the total mass of carbon fed with the algae. Figure A-8 shows the efficiency  $\eta$  for the different steam concentrations over the particle feeding rate. The efficiency is between 3.8% and 7.2% and depends strongly on the feeding rate but also increased steam concentrations result in higher efficiencies. The main reasons for the low efficiency are conduction losses along the tube and through the cavity walls which are inherent to lab scale reactors and were discussed in Section 7.4. In larger reactors these losses are significantly smaller due to the higher volume to surface ratio. Moreover, the low particle feeding rates are responsible for the low efficiency. It is expected that the efficiency would benefit strongly by an increase in the particle loading.

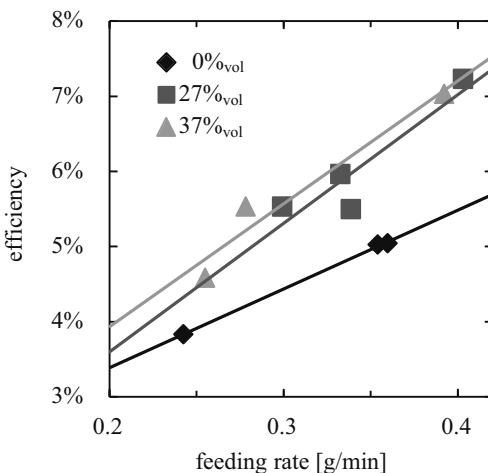


**Figure A-8:** Reactor efficiency  $\eta$  in dependence of the feeding rate for the three different steam concentrations.

## A.5 Conclusions

The steam-gasification of dry microalgae in a 1.2 kW indirectly-heated solar drop-tube gasifier consisting of an absorbing cavity and an absorbing tube was experimentally examined at ETH's high flux solar simulator at an inlet solid mass flux of 4.2 g/s·m<sup>2</sup>. Synthesis gas with a H<sub>2</sub>/CO ratio of up to 1.89 and a CO<sub>2</sub>/CO ratio of 0.55 was produced. The LHV of the syngas was between 19.4 MJ/Nm<sup>3</sup> for pure pyrolysis and 14.9 MJ/Nm<sup>3</sup> for 37%<sub>vol</sub> steam, thus significantly higher than those typically obtained in conventional autothermal gasification. It could also be confirmed that the biomass can be upgraded and solar energy stored.

An investigation of the influence of the inlet steam concentration showed that the carbon conversion, the upgrade factor, the efficiency as well as the concentrations of H<sub>2</sub> and CO<sub>2</sub> in the syngas increase with increasing steam concentration whereas the LHV of the syngas and the concentrations of CO,

$C_2H_2$ , and  $C_2H_4$  decreased.  $CH_4$  concentrations were hardly influenced by the presence of steam. Further it was seen that the efficiency increases strongly with an increase in the feeding rate.

## **Appendix B:**

### **Thermal Conductivity of a Bed of Char**

In the energy equation an effective thermal conductivity is applied for the heat flux within the moving bed. A comparison of a broad variety of different models [133] showed that the model of Yagi and Kunii [123] is suitable for heat conduction calculations of coal with ash deposits at high temperatures. The semi-empirical model of Yagi and Kunii that is followed in this work is a resistance network model. By applying the diffusion approximation for radiation within a solid medium, it includes the radiative conductivity in the network of resistances. The heat transfer within a packed or moving bed can be described as seven mechanisms that can be separated into two terms, a fluid flow independent and a fluid flow dependent term.

Fluid flow independent heat transfer mechanisms:

1. Thermal conduction through the solid particles
2. Thermal conduction through the contact surface of the particles
3. Radiative heat transfer between the surfaces of the particles
4. Radiative heat transfer between neighboring voids

Fluid flow dependent heat transfer mechanisms:

5. Thermal conduction through the fluid film near the contact surface of two particles
6. Convective heat transfer, solid-fluid-solid
7. Heat transfer by lateral mixing of fluid

For small Reynolds numbers the boundary layers around the solid particles are thick and the mechanisms 1, 3, 4, and 5 are predominant. However, for large Reynolds numbers, mechanism 7 controls the heat flux in any packed bed. Yagi and Kunii include mechanism 5 in the fluid flow independent term since the effect of the flow has only little effect on the mechanism. The model equation for the effective thermal conductivity  $k_{\text{eff}}$  consisting of the conductivity for motionless fluids  $k_{\text{eff}}^0$  and the conductivity due to lateral mixing of the fluid  $(k_{\text{eff}})_l$  is

$$k_{\text{eff}} = k_{\text{eff}}^0 + (k_{\text{eff}})_l \quad (\text{B.1})$$

In the case of gas-filled voids the effective conductivity for motionless fluid can be expressed as

$$\frac{k_{\text{eff}}^0}{k_f} = \frac{\beta(1-\phi)}{\gamma\left(\frac{k_f}{k_s}\right) + \frac{1}{(1/\phi) + (d_p h_{rs}/k_f)}} + \phi\beta \frac{d_p h_{rv}}{k_f} \quad (\text{B.2})$$

The radiation heat transfer coefficient  $h_{rs}$  through the contact surface is

$$h_{rs} = 1.163 \cdot 0.1952 \frac{\varepsilon}{2-\varepsilon} \left( \frac{T}{100} \right)^3 \quad (\text{B.3})$$

where  $\varepsilon$  is the emissivity. The radiation heat transfer coefficient through the voids is

$$h_{rv} = 1.163 \cdot \left[ 0.1952 \left/ \left\{ 1 + \frac{\phi}{2(1-\phi)} \cdot \frac{1-\varepsilon}{\varepsilon} \right\} \right] \cdot \left( \frac{T}{100} \right)^3 \quad (\text{B.4})$$

According to existing data, parameter  $\phi$  can be approximated as  $\phi \approx 0.04$  [133]. Typical values for granules were chosen for  $\beta$  and  $\gamma$ .  $\beta$  and  $\gamma$  were both set to 1.

In the present case the fluid flow is perpendicular to the direction of the main heat transfer. Although the Reynolds numbers are small, the effect of the fluid flow is not negligible.

$$\frac{(k_{\text{eff}})_t}{k_f} = (\alpha\beta) N_{\text{peM}} \quad (\text{B.5})$$

with  $N_{\text{peM}} = d_p C_p G / k_f$ .  $G$  is the mass velocity of the fluid based on the empty tube ( $G = u \cdot \rho$ ). For spheres, cylinders, pellets, or broken granules the values of  $(\alpha\beta)$  cover a narrow range of 0.1 to 0.14 for the different packing conditions [123]. Since no explicit values for the bed of char particles could be found in literature an intermediate value of 0.12 was chosen for  $(\alpha\beta)$ .

For the solid thermal conductivity in Eq. B2 the correlation of Atkinson and Merrick [134] for carbonaceous material was chosen.

$$k_s = (\rho_c / 4511)^{3.5} \sqrt{T} \quad [\text{W/m-K}] \quad (\text{B.6})$$

Although this correlation is not specifically for beech char, it is considered a reasonable approximation for chars with high carbon content. Based on a composition-dependent correlation for subbituminous chars a true density of  $\rho_c = 1279 \text{ kg/m}^3$  the char was estimated [134] and applied with good agreement by Piatkowski et al. [44]. The internal porosity of the particles was not considered and is part of the error. Since the sensitivity of the effective thermal conductivity to the solid thermal conductivity  $k_s$  is very small, no further attention was paid to this.

Since no values for emissivity of beech char could be found, the emissivity  $\varepsilon$  was assumed to be 0.92, the same as the one from straw char [135].



## Appendix C:

# Numerical Implementation of the Heat and Mass Transfer Model

The numerical implementation of the two-phase heat and mass transfer model described in Section 8.2 is described in more detail here. First, some definitions and a description of the discretization are given. Then, the discretization of the steady-state governing equations for mass, species, and energy in fluid and solid, which are solved iteratively using the cell centered finite volume method (FVM), is explained. Finally, the solution strategy is illustrated.

### C.1 Definitions

*Porosity* – The porosity of the domain  $\varphi$  is defined as the fraction of the fluid volume  $V_f$  to the total volume of the medium  $V_{\text{med}}$  comprising fluid and solid phases.

$$\varphi = V_f / V_{\text{med}} \quad (\text{C.1})$$

*Velocity* – The superficial or Darcy velocity of the fluid  $u$  is defined as

$$u = \dot{V}_f / A \quad (\text{C.2})$$

where  $\dot{V}_f$  is the volumetric fluid flow rate and  $A$  is the cross-sectional area.

*Molar mass* – The average molar mass of the fluid is defined as

$$\bar{M} = \sum_i w_i M_i \quad (\text{C.3})$$

where  $w_i$  and  $M_i$  are the mole fraction and molar mass of species  $i$ .

*Mass fraction* – The mass fraction of species  $k$  in dependence of the mole fraction  $y_k$  is defined as

$$w_k = \frac{y_k M_k}{\sum_i X_i M_i} = \frac{w_k M_k}{\bar{M}} \quad (\text{C.4})$$

*Density* – The density of the fluid  $\rho$  is computed using the ideal gas law.

$$\rho = \frac{p_{\text{tot}} \cdot \bar{M}}{R \cdot T_f} \quad (\text{C.5})$$

where  $p_{\text{tot}}$  is the total system pressure,  $R$  is the ideal gas constant, and  $T_f$  is the fluid temperature.

*Fluid temperature* – The fluid temperature  $T_f$  and the sensible energy of the mixture  $e_s$  are related via

$$e_s = \sum_k w_k h_{s,k}(T_f) - \frac{RT_0}{\bar{M}} \quad (\text{C.6})$$

where  $h_{s,k}$  is the sensible enthalpy of species  $k$  and  $T_0$  the reference temperature of 298 K.

## C.2 Discretization

The RPC section of the reactor, represented as a cylinder with diameter  $d_{\text{tube}}$  and height  $h_{\text{tube}}$ , was two-dimensionally discretized in cylindrical coordinates into  $N_z$  axial by  $N_r$  radial axisymmetric finite volumes  $\Delta V$  as shown in Figure C-1. In axial direction, the discretization was done uniformly with cell heights  $\Delta z$ . In radial direction, the mesh was refined towards the wall to capture

the large temperature and species concentration gradients. The radial cell size was described as

$$\Delta r_i = 1.2^{16/N_r} \Delta r_{i+1} \quad \text{for } i = 1, 2, \dots, N_r - 1 \quad (\text{C.7})$$

Figures C-2a and C-2b show the nomenclature in the grid-point cluster for the finite volume cells away from the domain boundary and at the domain boundary, respectively. P represents the cell center at which the cell properties such as  $D_k$ ,  $\rho$ , and  $k_{\text{eff}}$ , are evaluated. The neighboring cell centers or the domain boundary points in the north, east, south, and west are represented by N, E, S, and W, respectively. The cell boundaries are named n, e, s, and w. The cell centers are half way between the cell boundaries, i.e.  $\delta r_e = \delta r_w$  and  $\delta r_n = \delta r_s$ .

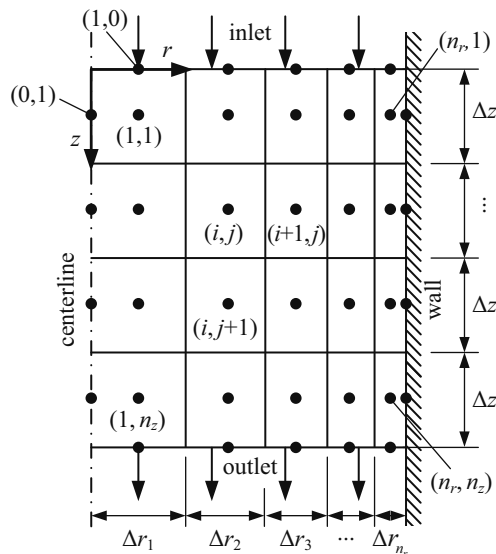


**Figure C-1:** Discretization of the RPC section of the reactor in the  $z$ - $r$  cylindrical coordinate system into  $N_r$  by  $N_z$  axisymmetric finite volumes  $\Delta V$ .

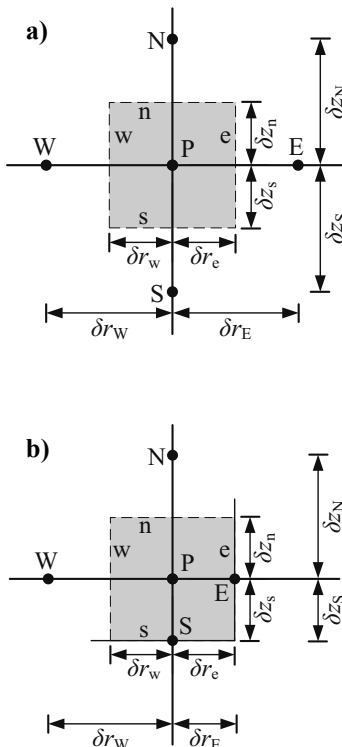


**Figure C-2:** Grid-point cluster for the finite volume cell  $\Delta V$  for a) cells away from the domain boundary and b) cells at the domain boundary (south east corner ( $N_r, N_z$ ) showed). P is the cell center. The neighboring cell centers or the domain boundary points are labeled N, E, S, and W. The cell boundaries are named n, e, s, and w.  $\delta r_e = \delta r_w$  and  $\delta r_n = \delta r_s$ .

The property and variable values at the cell boundaries were generally determined in the following way.

$$\Phi_x = f_x \Phi_p + (1 - f_x) \Phi_X \quad (C.8)$$

where  $x = n, e, s$ , and  $w$ ,  $X = N, E, S$ , and  $W$ , and

$$f_x = 1 - \frac{\delta r_x}{\delta r_X} \quad (C.9)$$

The diffusion coefficients  $D_k$  and the thermal conductivities  $k$  were computed as

$$D_{k,x} = \frac{1}{\frac{f_x}{D_{k,X}} + \frac{1-f_x}{D_{k,P}}} \quad (C.10)$$

$$k_x = \frac{1}{\frac{f_x}{k_X} + \frac{1-f_x}{k_p}} \quad (C.11)$$

The derivatives of the variables at the cell boundaries were defied as

$$\left( \frac{\partial \Phi}{\partial r} \right)_e = \frac{\Phi_E - \Phi_P}{\delta r_E} \text{ and } \left( \frac{\partial \Phi}{\partial r} \right)_w = \frac{\Phi_P - \Phi_W}{\delta r_W} \quad (C.12)$$

$$\left( \frac{\partial \Phi}{\partial z} \right)_s = \frac{\Phi_S - \Phi_P}{\delta z_S} \text{ and } \left( \frac{\partial \Phi}{\partial z} \right)_n = \frac{\Phi_P - \Phi_N}{\delta z_N} \quad (C.13)$$

### C.3 Determination of the Flow Field

The mass conservation equation introduced in Eq. 8.3 given by

$$\frac{1}{r} \frac{\partial}{\partial r} (r \rho u_r) + \frac{\partial}{\partial z} \rho u_z = \sum_k S_k \quad (C.14)$$

was used to compute the full velocity field. Equation C.14 was integrated over each control volume

$$\Delta V_{(i,j)} = \int_{\Delta V(i,j)} dV = \int_{z_n}^{z_s} \int_0^{2\pi} \int_{r_w}^{r_e} r dr d\theta dz \Big|_{(i,j)} \quad (C.15)$$

and simplified to

$$\begin{aligned} & \left\{ \Delta z \left[ (r \rho u_r)_e - (r \rho u_r)_w \right] + \frac{r_e^2 - r_w^2}{2} \left[ (\rho u_z)_s - (\rho u_z)_n \right] \right\}_{(i,j)} \\ &= \left[ \Delta z \frac{r_e^2 - r_w^2}{2} \sum_k \bar{S}_k \right]_{(i,j)} \end{aligned} \quad (\text{C.16})$$

where  $\Delta z = z_s - z_n$  and  $\bar{S}_k$  is the cell average of the mass source of species  $k$ . Equation C.16 is then summed up over all  $N_r$  control volumes in radial direction while using the relations

$$u_{r,w,(i+1,j)} = u_{r,e,(i,j)} \quad (\text{C.17})$$

$$\rho_{w,(i+1,j)} = \rho_{e,(i,j)} \quad (\text{C.18})$$

and the boundary conditions of no flow in radial direction at the wall  $r = r_{\max}$  and center  $r = 0$

$$u_{r,w,(1,j)} = u_{r,e,(N_r,j)} = 0 \quad (\text{C.19})$$

This leads to

$$\sum_{i=1}^{N_r} \left\{ \frac{r_e^2 - r_w^2}{2} \left[ (\rho u_z)_s - (\rho u_z)_n \right] \right\}_{(i,j)} = \sum_{i=1}^{N_r} \left[ \Delta z \frac{r_e^2 - r_w^2}{2} \sum_k \bar{S}_k \right]_{(i,j)} \quad (\text{C.20})$$

Applying the assumption that the axial velocity has no radial dependence

$$u_z(r, z) = u_z(z) \quad (\text{C.21})$$

allows solving for the axial velocity at the south side of each control volume.

$$u_{z,s,j} = \frac{\sum_{i=1}^{N_r} \left\{ (r_e^2 - r_w^2) \cdot \left[ (\rho u_z)_n + \Delta z \cdot \sum_k \bar{S}_k \right] \right\}_{(i,j)}}{\sum_{i=1}^{N_r} \left[ (r_e^2 - r_w^2) \cdot \rho_s \right]_{(i,j)}} \quad (\text{C.22})$$

Using the relation

$$u_{z,n,(i,j+1)} = u_{z,s,(i,j)} \quad (\text{C.23})$$

and the defined inlet velocity  $u_{z,n,(i,1)}$ ,  $u_{z,s}$  and  $u_{z,n}$  were then computed for the whole domain in the main flow direction i.e. starting from the north going south. To determine  $u_r$ , Eq. C.16 was solved for  $u_{r,e}$

$$u_{r,e,(i,j)} = \left. \frac{\frac{r_e^2 - r_w^2}{2} \left[ \Delta z \sum_k \bar{S}_k + (\rho u_z)_n - (\rho u_z)_s \right] + \Delta z (r \rho u_r)_w}{\Delta z (r \rho)_e} \right|_{(i,j)} \quad (\text{C.24})$$

Eq. C.24 is then evaluated for the whole domain starting from west going east using the  $u_{r,w,(1,j)}$  from boundary condition at the wall shown in Eq. C.19 to start with.

## C.4 Species Equation

The conservation equations for the species  $k = 1, 2, \dots, N_k$  were as introduced in Eq. 8.4 as

$$\begin{aligned} & \frac{1}{r} \frac{\partial}{\partial r} \left[ r \rho (u_r + v_r^c) w_k \right] + \frac{\partial}{\partial z} \left[ \rho (u_z + v_z^c) w_k \right] \\ &= \frac{1}{r} \frac{\partial}{\partial r} \left( r \rho D_{\text{eff},k,\perp} \frac{M_k}{M} \frac{\partial y_k}{\partial r} \right) + \frac{\partial}{\partial z} \left( \rho D_{\text{eff},k,\parallel} \frac{M_k}{M} \frac{\partial y_k}{\partial z} \right) + S_k \end{aligned} \quad (\text{C.25})$$

with the correction velocities

$$v_r^c = \sum_k D_{\text{eff},k,\perp} \frac{M_k}{M} \frac{\partial y_k}{\partial r} \quad (\text{C.26})$$

$$v_z^c = \sum_k D_{\text{eff},k,\parallel} \frac{M_k}{M} \frac{\partial y_k}{\partial z} \quad (\text{C.27})$$

The derivatives of the mole fractions  $y_k$  on the right hand side of Eq. C.25 are expressed in the following way.

$$\frac{M_k}{\bar{M}} \frac{\partial y_k}{\partial r} = \frac{\partial w_k}{\partial r} - \bar{M} w_k \frac{\partial}{\partial r} \sum_i \frac{w_i}{M_i} \quad (\text{C.28})$$

$$\frac{M_k}{\bar{M}} \frac{\partial y_k}{\partial z} = \frac{\partial w_k}{\partial z} - \bar{M} w_k \frac{\partial}{\partial z} \sum_i \frac{w_i}{M_i} \quad (\text{C.29})$$

Equations C.28 and C.29 are then substituted into Eq. C.25. In a next step, the resulting equation is rearranged and integrated over each control volume  $\Delta V$  defined in Eq. C.15. The derivatives of the mass fractions  $w_k$  at the cell boundaries are expressed as described in Eqs. C.12 and C.13. The mass fractions at the cell boundaries are evaluated as shown in Eq. C.8. This tedious procedure leads to

$$\begin{aligned} & r_e \Delta z \rho_e \left( u_r + v_r^C + D_{\text{eff},k,\perp} \bar{M} \frac{\partial}{\partial r} \sum_i \frac{w_i}{M_i} \right)_e \cdot \left[ f_e w_{k,p} + (1-f_e) w_{k,E} \right] \\ & - r_w \Delta z \rho_w \left( u_r + v_r^C + D_{\text{eff},k,\perp} \bar{M} \frac{\partial}{\partial r} \sum_i \frac{w_i}{M_i} \right)_w \cdot \left[ f_w w_{k,p} + (1-f_w) w_{k,W} \right] \\ & + \frac{r_e^2 - r_w^2}{2} \rho_s \left( u_z + v_z^C + D_{\text{eff},k,\parallel} \bar{M} \frac{\partial}{\partial z} \sum_i \frac{w_i}{M_i} \right)_s \cdot \left[ f_s w_{k,p} + (1-f_s) w_{k,S} \right] \\ & - \frac{r_e^2 - r_w^2}{2} \rho_n \left( u_z + v_z^C + D_{\text{eff},k,\parallel} \bar{M} \frac{\partial}{\partial z} \sum_i \frac{w_i}{M_i} \right)_n \cdot \left[ f_n w_{k,p} + (1-f_n) w_{k,N} \right] \quad (\text{C.30}) \\ & = r_e \Delta z \rho_e D_{\text{eff},k,\perp,e} \frac{w_{k,E} - w_{k,p}}{\delta r_E} - r_w \Delta z \rho_w D_{\text{eff},k,\perp,w} \frac{w_{k,p} - w_{k,W}}{\delta r_W} \\ & + \frac{r_e^2 - r_w^2}{2} \rho_s D_{\text{eff},k,\parallel,s} \frac{w_{k,S} - w_{k,p}}{\delta z_S} - \frac{r_e^2 - r_w^2}{2} \rho_n D_{\text{eff},k,\parallel,n} \frac{w_{k,p} - w_{k,N}}{\delta z_N} \\ & + \Delta z \frac{r_e^2 - r_w^2}{2} S_{k,p} \end{aligned}$$

where  $\Delta z = z_s - z_n$ .

The species source term  $S_{k,P}$  introduced in Eq. 8.18 was linearized around  $w_{k,P}^*$ , the value of the previous iteration of  $w_{k,P}$ , and expressed in the following form.

$$S_{k,P} = S_k(w_{k,P}) \approx S_k(w_{k,P}^*) + \frac{dS_k}{dw_k} \Big|_{w_{k,P}^*} \cdot w_{k,P} = S_{k,\text{const},P} + S_{k,\text{prop},P} \cdot w_{k,P} \quad (\text{C.31})$$

Inserting Eq. C.31 into Eq. C.30 and denoting the convection terms as  $F_n$ ,  $F_e$ ,  $F_s$ , and  $F_w$ , and the diffusion terms as  $D_n$ ,  $D_e$ ,  $D_s$ , and  $D_w$ , leads to

$$\begin{aligned} & F_e \cdot [f_e w_{k,P} + (1-f_e) w_{k,E}] - F_w \cdot [f_w w_{k,P} + (1-f_w) w_{k,W}] \\ & + F_s \cdot [f_s w_{k,P} + (1-f_s) w_{k,S}] - F_n \cdot [f_n w_{k,P} + (1-f_n) w_{k,N}] \\ & = D_e \cdot (w_{k,E} - w_{k,P}) - D_w \cdot (w_{k,P} - w_{k,W}) \\ & + D_s \cdot (w_{k,S} - w_{k,P}) - D_n \cdot (w_{k,P} - w_{k,N}) \\ & + \Delta z \frac{r_e^2 - r_w^2}{2} (S_{k,\text{const}} + S_{k,\text{prop}} \cdot w_{k,P}) \end{aligned} \quad (\text{C.32})$$

Eq. C.32 can now be brought into the standard form used by Patankar [136] and obtain the coefficients  $a_E$ ,  $a_W$ ,  $a_S$ , and  $a_N$ .

$$a_P \cdot w_{k,P} = a_E \cdot w_{k,E} + a_W \cdot w_{k,W} + a_S \cdot w_{k,S} + a_N \cdot w_{k,N} + b \quad (\text{C.33})$$

To have a mathematically more stable system of equations, the hybrid scheme [119] is applied and the coefficients  $a_E$ ,  $a_W$ ,  $a_S$ , and  $a_N$  are thus modified to

$$a_E = \llbracket -F_e, D_e - F_e (1-f_e), 0 \rrbracket \quad (\text{C.34})$$

$$a_W = \llbracket F_w, D_w + F_w (1-f_w), 0 \rrbracket \quad (\text{C.35})$$

$$a_S = \llbracket -F_s, D_s - F_s (1-f_s), 0 \rrbracket \quad (\text{C.36})$$

$$a_N = \llbracket F_n, D_n + F_n (1-f_n), 0 \rrbracket \quad (\text{C.37})$$

where  $\llbracket A, B, C \rrbracket$  denotes the greatest of  $A$ ,  $B$ , and  $C$ .

Equation C.33 is applied for all cells  $(i,j)$  where  $i = 1, 2, \dots, N_r$  and  $j = 1, 2, \dots, N_z$ . For the boundary nodes  $(i,0)$  for  $i = 1, 2, \dots, N_r$  and  $(0,j)$  for  $j = 1, 2, \dots, N_z$ , additional equations were defined to account for the boundary conditions. For a defined boundary value  $w_{k,\text{boundary}}$  the additional equation is

$$w_{k,\text{P}} = w_{k,\text{boundary}} \quad (\text{C.38})$$

For a defined gradient boundary condition, e.g. at the south boundary, the additional equation is

$$w_{k,\text{P}} = w_{k,\text{N}} + \delta z_N \cdot \left( \frac{\partial w_k}{\partial z} \right)_{\text{boundary}} \quad (\text{C.39})$$

For each species, the resulting linear system of equations, comprising Eqs. C.33, C.38, and C.39, was written into matrix form. The solutions were then found using MATLAB (The MathWorks, Inc.), by either permutation and forward solving, or by using the unsymmetric-pattern multifrontal method described by Davis [120].

## C.5 Fluid Phase Energy Equation

The fluid phase energy equation introduced in Eq. 8.7 was defined as

$$\begin{aligned} & \frac{1}{r} \frac{\partial}{\partial r} (r \rho u_r e_s) + \frac{\partial}{\partial z} (\rho u_z e_s) \\ &= \frac{1}{r} \frac{\partial}{\partial r} \left[ r \rho \sum_k \left( h_{s,k} D_{\text{eff},k,\perp} \frac{M_k}{\bar{M}} \frac{\partial y_k}{\partial r} \right) \right] \\ &+ \frac{\partial}{\partial z} \left[ \rho \sum_k \left( h_{s,k} D_{\text{eff},k,\parallel} \frac{M_k}{\bar{M}} \frac{\partial y_k}{\partial z} \right) \right] + h_{sf} A_0 (T_s - T_f) \end{aligned} \quad (\text{C.40})$$

Integrating Eq. C.40 over each control volume  $\Delta V$  defined in Eq. C.15, expressing the derivatives of the mass fraction at the cell boundaries as

described in Eqs. C.12 and C.13 and the sensible energy at the boundaries as shown in Eq. C.8 leads to

$$\begin{aligned}
 & r_e \Delta z \rho_e u_{r,e} \cdot [f_e e_{s,p} + (1-f_e) e_{s,E}] \\
 & - r_w \Delta z \rho_w u_{r,w} \cdot [f_w e_{s,p} + (1-f_w) e_{s,W}] \\
 & + \frac{r_e^2 - r_w^2}{2} \rho_s u_{z,s} \cdot [f_s e_{s,p} + (1-f_s) e_{s,S}] \\
 & - \frac{r_e^2 - r_w^2}{2} \rho_n u_{z,n} \cdot [f_n e_{s,p} + (1-f_n) e_{s,N}] \\
 = & r_e \Delta z \rho_e \sum_k h_{s,k,e} \left( D_{\text{eff},k,\perp} \frac{M_k}{\bar{M}} \right)_e \frac{y_{k,E} - y_{k,p}}{\delta r_E} \\
 & - r_w \Delta z \rho_w \sum_k h_{s,k,w} \left( D_{\text{eff},k,\perp} \frac{M_k}{\bar{M}} \right)_w \frac{y_{k,p} - y_{k,W}}{\delta r_W} \\
 & + \frac{r_e^2 - r_w^2}{2} \rho_s \sum_k h_{s,k,s} \left( D_{\text{eff},k,\parallel} \frac{M_k}{\bar{M}} \right)_s \frac{y_{k,S} - y_{k,p}}{\delta z_S} \\
 & - \frac{r_e^2 - r_w^2}{2} \rho_n \sum_k h_{s,k,n} \left( D_{\text{eff},k,\parallel} \frac{M_k}{\bar{M}} \right)_n \frac{y_{k,p} - y_{k,N}}{\delta z_N} \\
 & + \Delta z \frac{r_e^2 - r_w^2}{2} h_{sf} A_0 (T_{s,p} - T_{f,p})
 \end{aligned} \tag{C.40}$$

where  $\Delta z = z_s - z_n$ . The temperature difference  $T_{s,p} - T_{f,p}$  in the term for the heat transfer between solid and fluid can be expressed as a function of the sensible energy  $e_s$ . The temperature difference is thus expanded as

$$T_{s,p} - T_{f,p} = (T_{s,p} - T_{f,p}^*) + (T_{f,p}^* - T_{f,p}) \tag{C.41}$$

where the symbol  $T_{f,p}^*$  is used to denote the previous iteration value of  $T_{f,p}$ . Using the definition of the sensible energy

$$e_s = h_s - \frac{RT_0}{\bar{M}} = \int_{T_0}^T C_v dT - \frac{RT_0}{\bar{M}} \tag{C.42}$$

where  $h_s$  is the sensible enthalpy and  $C_v$  is the heat capacity of the mixture, we can formulate a sensible energy difference

$$e_{s,p}^* - e_{s,p} = \int_{T_0}^{T_{f,p}^*} C_v dT - \frac{RT_0}{M} - \left( \int_{T_0}^{T_{f,p}} C_v dT - \frac{RT_0}{M} \right) = \int_{T_{f,p}}^{T_{f,p}^*} C_v dT \quad (C.43)$$

With the approximation that  $C_v$  is constant within the small temperature difference  $T_{f,p}^* - T_{f,p}$ , Eq. C.43 can be simplified and rearranged to

$$T_{f,p}^* - T_{f,p} = \frac{e_{s,p}^* - e_{s,p}}{C_v(T_{f,p}^*)} \quad (C.44)$$

The term  $T_{f,p}^* - T_{f,p}$  is now expressed as a function of the sensible energy and can be inserted into Eq. C.41 yielding

$$T_{s,p} - T_{f,p} = (T_{s,p} - T_{f,p}^*) + \frac{e_{s,p}^* - e_{s,p}}{C_v(T_{f,p}^*)} \quad (C.45)$$

Substituting Eq. C.45 into Eq. C.40 and expressing the convection terms as  $F_n$ ,  $F_e$ ,  $F_s$ , and  $F_w$  leads to

$$\begin{aligned} & F_e \cdot [f_e e_{s,p} + (1-f_e) e_{s,E}] - F_w \cdot [f_w e_{s,p} + (1-f_w) e_{s,W}] \\ & + F_s \cdot [f_s e_{s,p} + (1-f_s) e_{s,S}] - F_n \cdot [f_n e_{s,p} + (1-f_n) e_{s,N}] \\ & = r_e \Delta z \rho_e \sum_k h_{s,k,e} \left( D_{\text{eff},k,\perp} \frac{M_k}{M} \right)_e \frac{y_{k,E} - y_{k,p}}{\delta r_e} \\ & - r_w \Delta z \rho_w \sum_k h_{s,k,w} \left( D_{\text{eff},k,\perp} \frac{M_k}{M} \right)_w \frac{y_{k,p} - y_{k,w}}{\delta r_w} \\ & + \frac{r_e^2 - r_w^2}{2} \rho_s \sum_k h_{s,k,s} \left( D_{\text{eff},k,\parallel} \frac{M_k}{M} \right)_s \frac{y_{k,S} - y_{k,p}}{\delta z_s} \\ & - \frac{r_e^2 - r_w^2}{2} \rho_n \sum_k h_{s,k,n} \left( D_{\text{eff},k,\parallel} \frac{M_k}{M} \right)_n \frac{y_{k,p} - y_{k,N}}{\delta z_n} \\ & + \Delta z \frac{r_e^2 - r_w^2}{2} h_{sf} A_0 \left[ \left( T_{s,p} - T_{f,p}^* + \frac{e_{s,p}^*}{C_v(T_{f,p}^*)} \right) - \frac{1}{C_v(T_{f,p}^*)} \cdot e_{s,p} \right] \end{aligned} \quad (C.46)$$

The terms  $D_n$ ,  $D_e$ ,  $D_s$ , and  $D_w$  applied in the previous section are 0 here as no diffusion terms are present. We can again bring the equation into the standard form and determine the coefficients  $a_E$ ,  $a_W$ ,  $a_S$ , and  $a_N$ .

$$a_p \cdot e_{s,p} = a_E \cdot e_{s,E} + a_W \cdot e_{s,W} + a_N \cdot e_{s,N} + a_S \cdot e_{s,S} + b \quad (C.47)$$

To obtain a mathematically more stable system of equations, the hybrid scheme [119] is applied and the coefficients  $a_E$ ,  $a_W$ ,  $a_S$ , and  $a_N$  are thus modified to

$$a_E = \llbracket -F_e, D_e - F_e(1 - f_e), 0 \rrbracket \quad (C.48)$$

$$a_W = \llbracket F_w, D_w + F_w(1 - f_w), 0 \rrbracket \quad (C.49)$$

$$a_S = \llbracket -F_s, D_s - F_s(1 - f_s), 0 \rrbracket \quad (C.50)$$

$$a_N = \llbracket F_n, D_n + F_n(1 - f_n), 0 \rrbracket \quad (C.51)$$

Equation C.47 is applied for all cells  $(i,j)$  where  $i = 1, 2, \dots, N_r$  and  $j = 1, 2, \dots, N_z$ . For the boundary nodes  $(i,0)$  for  $i = 1, 2, \dots, N_r$  and  $(0,j)$  for  $j = 1, 2, \dots, N_z$ , additional equations were defined to account for the boundary conditions. For a defined boundary value the additional equation is

$$e_{s,p} = e_{s,boundary} \quad (C.52)$$

For a defined gradient, shown for the south boundary here, the additional equation is of the form

$$e_{s,p} = e_{s,N} + \delta z_N \cdot \frac{\partial}{\partial z} e_{s,boundary} \quad (C.53)$$

The linear system of equations, comprising the equations for the cells and the ones for the boundary nodes, was then written into matrix form and solved as described in the previous section.

## C.6 Solid Phase Energy Equation

The energy equation of the solid phase introduced in Eq. 8.8 is given by

$$0 = \frac{1}{r} \frac{\partial}{\partial r} \left( r k_{\text{eff}} \frac{\partial T_s}{\partial r} \right) + \frac{\partial}{\partial z} \left( k_{\text{eff}} \frac{\partial T_s}{\partial z} \right) + h_{\text{sf}} A_0 (T_f - T_s) - \dot{Q}_{\text{react}} \quad (\text{C.54})$$

Integrating Eq. C.54 over all control volumes  $\Delta V$  and applying the solid temperature  $T_s$  derivatives at the cell boundaries as described in Eqs. C.12 and C.13, results in

$$\begin{aligned} 0 = & \Delta z \cdot r_e \cdot k_{\text{eff},e} \cdot \frac{T_{s,E} - T_{s,P}}{\delta r_E} - \Delta z \cdot r_e \cdot k_{\text{eff},w} \cdot \frac{T_{s,P} - T_{s,W}}{\delta r_W} \\ & + \frac{r_e^2 - r_w^2}{2} \cdot k_{\text{eff},s} \cdot \frac{T_{s,S} - T_{s,P}}{\delta z_S} - \frac{r_e^2 - r_w^2}{2} \cdot k_{\text{eff},n} \cdot \frac{T_{s,P} - T_{s,N}}{\delta z_N} \\ & + \Delta z \cdot \frac{r_e^2 - r_w^2}{2} \cdot \left[ h_{\text{sf}} A_0 (T_{f,P} - T_{s,P}) - \dot{Q}_{\text{react,P}} \right] \end{aligned} \quad (\text{C.55})$$

where  $\Delta z = z_s - z_n$ .

The chemical reaction term is linearized around  $T_{s,P}^*$ , the initial value or the value of the previous iteration of  $T_{s,P}$ .

$$\begin{aligned} \dot{Q}_{\text{react,P}} &= \dot{Q}_{\text{react}} (T_{s,P}) \\ &\approx \dot{Q}_{\text{react}} (T_{s,P}^*) + \frac{d\dot{Q}_{\text{react}}}{dT_s} \Big|_{T_{s,P}^*} \cdot T_{s,P} = \dot{Q}_{\text{react,const,P}} + \dot{Q}_{\text{react,prop,P}} \cdot T_{s,P} \end{aligned} \quad (\text{C.56})$$

Equation C.56 is inserted into Eq. C.55, that is then brought into the standard form and the coefficients  $a_E$ ,  $a_W$ ,  $a_S$ , and  $a_N$  are determined.

$$a_p T_{s,P} = a_E T_{s,E} + a_W T_{s,W} + a_S T_{s,S} + a_N T_{s,N} + b \quad (\text{C.57})$$

As the solid phase energy equation has no convective term, this is already the final form. Applying the hybrid scheme would lead the same form.

Eq. C.57 is applied for the cells  $(i,j)$  where  $i = 1, 2, \dots, N_r$  and  $j = 1, 2, \dots, N_z$ . For the boundary nodes  $(i,0)$  for  $i = 1, 2, \dots, N_r$  and  $(0,j)$  for  $j = 1, 2, \dots, N_z$ ,

additional equations were defined to take the boundary conditions into account. For a constant boundary temperature  $T_{s,\text{boundary}}$  the additional equation is

$$T_{s,p} = T_{s,\text{boundary}} \quad (\text{C.58})$$

For a defined gradient, e.g. at the south boundary, the additional equation is of the form

$$T_{s,p} = T_{s,N} + \delta z_N \cdot \frac{\partial}{\partial z} T_{s,\text{boundary}} \quad (\text{C.59})$$

The linear system of equations, comprising Eqs. C.57, C.58, and C.59, is then written into matrix form and solved as described in Section C.4.

## C.7 Solution Strategy

The solution to the set of governing equations was found iteratively by solving them in the order shown in Figure C-3. At first, the initial conditions were used to determine the variable properties such as  $k_{\text{eff}}$ ,  $D_{\text{eff},k}$ ,  $\rho$ ,  $h_{\text{sf}}$ , etc. In a next step, the full flow field ( $u_r$ ,  $u_z$ ) was computed as described in Section C.3 and the properties were updated. Then, the species conservation equations, the fluid phase energy equation and the solid phase energy equation were solved sequentially while updating the properties after each equation. This yields  $w_k$ ,  $e_s$ , and  $T_s$ .

The values of the dependent variable  $\Phi = u_r$ ,  $u_z$ ,  $T_s$ ,  $w_k$ , or  $e_s$  were then used to compute the residual error to check for convergence. The error of the  $i$ -th iteration step  $E_i$  was computed by taking the root mean square of the step change of the dependent variable  $\Phi$ , the quantity the governing equation was solved for, over all  $N$  cells.

$$E_i = \sqrt{\frac{1}{N} \sum_{n=1}^N (\Phi_{n,i} - \Phi_{n,i-1})^2} \quad (\text{C.60})$$

The residual error was then defined as the error of the  $i$ -th iteration normalized by the error of first iteration.

$$R_i = E_i / E_1 \quad (\text{C.61})$$

The described procedure was repeated until the convergence criterion for the residuals  $R_i < 10^{-7}$  was reached for all dependent variables  $u_r$ ,  $u_z$ ,  $T_s$ ,  $w_k$ , and  $e_s$ . Once reached, the solution was found and the result returned.

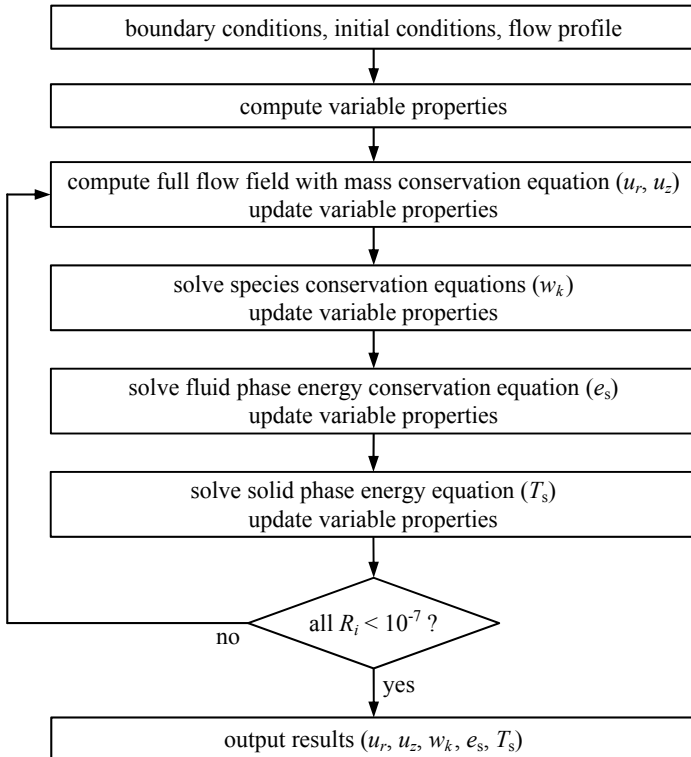


**Figure C-3:** Solution strategy.

## List of Figures

<b>Figure 1-1:</b> Solar-driven steam gasification process flow sheet.....	3
<b>Figure 2-1:</b> Primary and secondary reactions during pyrolysis of a biomass particle. Adapted from ref. [14].....	8
<b>Figure 2-2:</b> Biomass gasifier types with main flow streams: a) updraft (countercurrent), b) downdraft (concurrent), c) bubbling fluidized bed, d) circulating fluidized bed, e) dual fluidized bed, and f) entrained-flow. Colors indicate relative temperatures (red = hot, yellow = medium, gray = cold). Adapted from ref. [5]. .....	13
<b>Figure 2-3:</b> Solar tower concentrating systems: a) solar reactor on top of tower and b) beam down design with secondary hyperbolic mirror on tower and solar reactor at ground. Adapted from ref. [31]. .....	16
<b>Figure 2-4:</b> Solar gasifier concepts: a) tower-mounted drop-tube [41] and b) packed bed for a beam-down configuration [40]. Arrow indicates where the concentrated solar radiation enters the reactor. .....	19
<b>Figure 3-1:</b> Biomass feedstocks used: a) Brazilian sugarcane bagasse and b) beech char.....	21
<b>Figure 3-2:</b> Particle size distribution functions of ground and sieved bagasse, and beech char analyzed with LA-950 analyzer (HORIBA).....	24
<b>Figure 4-1:</b> Equilibrium composition as a function of temperature of the stoichiometric system of Eq. 4.1 for bagasse ( $\text{CH}_{1.665}\text{O}_{0.663}$ ) at 1 bar.....	26
<b>Figure 4-2:</b> Equilibrium composition as a function of temperature of the stoichiometric system of Eq. 4.1 for bagasse ( $\text{CH}_{1.665}\text{O}_{0.663}$ ) at 10 bar.....	26
<b>Figure 4-3:</b> Reaction enthalpy $\Delta h_R$ for the system $\text{CH}_x\text{O}_y + (1-y) \text{ H}_2\text{O}$ (reactants fed at 298 K and 1 bar, products obtained at	

chemical equilibrium) and LHV of product gas as a function of temperature.....	27
<b>Figure 4-4:</b> Equilibrium composition as a function of adiabatic temperature for the system in Eqs. 4.3 and 4.4 with $0 \leq \phi \leq 0.33$ .....	29
<b>Figure 4-5:</b> Molar ratios of H <sub>2</sub> /CO and CO <sub>2</sub> /CO at equilibrium over temperature for solar and autothermal gasification.....	29
<b>Figure 4-6:</b> Flow diagram applied in the first and second law analyses for the solar (left) and autothermal gasification (right).....	30
<b>Figure 5-1:</b> Thermogravimetric balance configuration.....	40
<b>Figure 5-2:</b> Apparent carbon conversion rate for the experimental measurements vs. the model for the temperature range 1173–1473 K and 25–75% <sub>vol</sub> steam concentration.....	47
<b>Figure 5-3:</b> Typical experimental results and linear fits for $-\ln(1-X)$ vs. time for selected experiments with a 75% <sub>vol</sub> steam/Ar mixture.....	47
<b>Figure 6-1:</b> Schematic of the laboratory-scale biomass gasification apparatus including the primary components and flows.....	51
<b>Figure 6-2:</b> Relative mole fractions (dry, N <sub>2</sub> and Ar free basis) of the product gases and the equilibrium composition (lines without markers).....	54
<b>Figure 7-1:</b> Schematic of the solar cavity-receiver/reactor configuration with thermocouple locations and blown up detail of the reactor tube showing the fast pyrolysis drop-tube zone and the trickle-bed char gasification zone (RPC = reticulate porous ceramic, CPC = compound parabolic concentrator) .....	58
<b>Figure 7-2:</b> Structure packing made of 10 ppi SiSiC reticulate porous ceramic (RPC) foam installed in the solar gasifier. Image from [88].....	59
<b>Figure 7-3:</b> Schematic of the solar-driven biomass gasifier, including the high-flux solar simulator and the auxiliary components and flows.....	61
<b>Figure 7-4:</b> Input power ( $\dot{Q}_{\text{solar}}$ ) and reactor temperatures during a typical experiment: ① steam on, ② biomass feed on, and ③ biomass feed off .....	63

---

<b>Figure 7-5:</b>	Molar flow rates of product gases as a function of time during a typical experimental run: ① steam on, ② biomass feed on, and ③ biomass feed off.....	64
<b>Figure 7-6:</b>	Average gas concentrations for a) H <sub>2</sub> , CO, CO <sub>2</sub> , and CH <sub>4</sub> , and b) C <sub>2</sub> H <sub>2</sub> , C <sub>2</sub> H <sub>4</sub> , and C <sub>2</sub> H <sub>6</sub> calculated on H <sub>2</sub> O, N <sub>2</sub> , and Ar free basis for the investigated configurations: A = 50 mm tall RPC, B = 100 mm tall RPC, PP = free-fall pure pyrolysis, and SG = free-fall steam-based gasification. Error bars indicate the span between the minimum and maximum values. ....	68
<b>Figure 7-7:</b>	Carbon conversion and upgrade factors for investigated configurations: A = 50 mm tall RPC, B = 100 mm tall RPC, PP = free-fall pure pyrolysis, SG = free-fall steam gasification. Error bars illustrate the span between the minimum and maximum values. ....	70
<b>Figure 7-8:</b>	The 50 mm tall RPC after one of the A experiments. The particles are uniformly distributed throughout the entire RPC. ....	71
<b>Figure 7-9:</b>	Overview temperature measurements and heat losses: radiation and convection through the aperture $\dot{Q}_{\text{rad}}$ and $\dot{Q}_{\text{conv}}$ , conduction through the cavity walls $\dot{Q}_{\text{walls}}$ and along the reactor tube towards the top $\dot{Q}_{\text{cond,top}}$ and the bottom $\dot{Q}_{\text{cond,bottom}}$ .....	72
<b>Figure 7-10:</b>	Convection losses through aperture: Air temperature distribution in cavity, aperture, and surrounding.....	76
<b>Figure 7-11:</b>	Energy losses of solar reactor via radiation and convection through the aperture $\dot{Q}_{\text{rad}}$ and $\dot{Q}_{\text{conv}}$ , conduction through the walls $\dot{Q}_{\text{walls}}$ and along the tube $\dot{Q}_{\text{cond,top}}$ and $\dot{Q}_{\text{cond,bottom}}$ .....	79
<b>Figure 8-1:</b>	Schematic of the experimental setup.....	84
<b>Figure 8-2:</b>	Photograph of the SiSiC reticulate porous ceramic (RPC) with 10 pores per inch (ppi) used as packing in the tubular gasifier. ....	85
<b>Figure 8-3:</b>	Schematic (not to scale) of the main reactor tube, RPC, and supporting tube assembly indicating thermocouple locations. Thermocouples $T_{W6}$ and $T_{W7}$ were movable along the tube wall.....	86

<b>Figure 8-4:</b>	Temporal product gas flow rates over the course of a typical experiment .....	88
<b>Figure 8-5:</b>	Carbon conversion ( $X_C$ ) as function of furnace set-point temperature ( $T_{furnace}$ ), steam concentration, and gasifier configuration (RPC versus no RPC). ....	89
<b>Figure 8-6:</b>	Discretization for the radiative exchange between the RPC's top and bottom surfaces to their surroundings. Tube sections above and below RPC: 100 segments each, RPC surfaces: 64 rings, flanges: individual surfaces. The smaller tube diameter below the RPC is due to the supporting tube. ....	95
<b>Figure 8-7:</b>	Results from code verification of the diffusion terms in the species equation, a) error norm $E_2$ and b) actual order of accuracy $q_a$ .....	100
<b>Figure 8-8:</b>	Comparison between experimental ( $T_{s,center,exp}$ - filled markers) and simulated centerline solid temperature profiles ( $T_{s,center,sim}$ - solid lines) for a) non-reacting conditions, and b) reacting conditions. The open markers indicate the experimental wall temperatures ( $T_{wall,exp}$ ); the dashed lines represent the boundary temperatures ( $T_{wall,bc}$ ) applied in the simulations. ....	102
<b>Figure 8-9:</b>	Comparison of experimentally determined and simulated molar flow rates of gasified carbon.....	103
<b>Figure 8-10:</b>	Simulated radial profiles of a) solid temperature, b) steam mole fraction, and c) gasification rate at $z = 0.5$ m for $l = 0.2$ and $T_{wall} = 1173, 1223$ , and $1273$ K. ....	105
<b>Figure 8-11:</b>	Sensitivity of a) the syngas production rate ( $\dot{n}_{C,syngas,RPC}$ ) and b) the temperature difference between wall and centerline at the outlet of the domain $\Delta T_{s,outlet} = T_{s,outlet,wall} - T_{s,outlet,center}$ to changes in nominal pore diameter ( $d_{nom}$ ), solid thermal conductivity ( $k_s$ ), RPC porosity ( $\varphi_{RPC}$ ), and particle loading ( $l$ ) for $T_{wall} = 1173, 1223$ , and $1273$ K. Reference case: $d_{nom} = 2.54$ mm, $k_s = k_{SiC}$ , $\varphi_{RPC} = 89\%$ , and $l = 0.2$ .....	107
<b>Figure 8-12:</b>	Simulated radial profiles of a) solid temperature ( $T_s$ ), b) steam mole fraction ( $y_{H_2O}$ ), and c) gasification rate ( $\dot{m}_C$ ) in moving bed (MB) and RPC ( $l = 0.1, 0.2$ , and $0.4$ ) at $z = 0.5$ m for $T_{wall} = 1223$ K.....	110

---

<b>Figure 8-13:</b> Effective thermal conductivity ( $k_{\text{eff}}$ ) over temperature for the moving bed (MB) with $\text{N}_2$ filled voids and the RPC configuration at various loadings ( $l$ ). ....	111
<b>Figure 8-14:</b> Contribution of radiation term $k_{\text{rad}}$ on the effective thermal conductivity $k_{\text{eff}}$ for RPC configuration.....	112
<b>Figure 8-15:</b> Simulation results for ratio of trickle-bed to moving-bed gasification rates as function of the particle loading in the RPC ( $l$ ) and wall temperatures of $T_{\text{wall}} = 1173$ , 1223, and 1273 K.....	113
<b>Figure A-1:</b> Spray dried microalgae (chlorella vulgaris). ....	123
<b>Figure A-2:</b> Particle size distribution of spray-dried microalgae analyzed with LA-950 analyzer (HORIBA). ....	124
<b>Figure A-3:</b> Schematic of the solar entrained flow gasifier including solar simulator and the primary components and flows. ....	125
<b>Figure A-4:</b> Molar flow rate of the product gases during a typical experiment.....	128
<b>Figure A-5:</b> Product gas compositions for different volumetric steam concentrations. Error bars indicate the span between the minimum and maximum values. ....	130
<b>Figure A-6:</b> LHV <sub>syngas</sub> for different volumetric steam concentrations. Error bars indicate the span between the minimum and maximum values. ....	131
<b>Figure A-7:</b> Carbon conversion and upgrade factor for different volumetric steam concentrations. Error bars indicate the span between the minimum and maximum values. ....	132
<b>Figure A-8:</b> Reactor efficiency $\eta$ in dependence of the feeding rate for the three different steam concentrations.....	133
<b>Figure C-1:</b> Discretization of the RPC section of the reactor in the $z-r$ cylindrical coordinate system into $N_r$ by $N_z$ axisymmetric finite volumes $\Delta V$ . ....	141
<b>Figure C-2:</b> Grid-point cluster for the finite volume cell $\Delta V$ for a) cells away from the domain boundary and b) cells at the domain boundary (south east corner ( $N_r, N_z$ ) showed). P is the cell center. The neighboring cell centers or the domain boundary points are labeled N, E, S, and W. The cell boundaries are named n, e, s, and w. $\delta r_e = \delta r_w$ and $\delta r_n = \delta r_s$ . ...	142

<b>Figure C-3:</b> Solution strategy .....	154
--	-----

## List of Tables

<b>Table 2-1:</b>	Typical product gas composition for different biomass gasifiers.....	14
<b>Table 2-2:</b>	Existing solar gasifier concepts and feedstocks used.....	17
<b>Table 3-1:</b>	Physical and chemical properties of bagasse and beech char: Ultimate and proximate analyses, heating value and mean particle size.....	23
<b>Table 4-1:</b>	Energy and exergy analysis for solar and autothermal gasification. Values for power refer to a biomass feed rate of $\dot{m}_{\text{CH}_x\text{O}_y} = 1 \text{ g/s}$ .....	34
<b>Table 5-1:</b>	Elemental composition of raw and rapidly pyrolyzed bagasse particles; C, H, N determined with CHN-900, O with RO-478, and S with CHNS-932 (all LECO Corporation, St. Joseph, MI).....	41
<b>Table 5-2:</b>	Apparent kinetic parameters for Eq. 5.16 for the steam gasification of rapidly pyrolyzed bagasse.....	46
<b>Table 6-1:</b>	Summary of the experimental results obtained for the gasification of bagasse in the electrically heated two-zone reactor .....	53
<b>Table 7-1:</b>	Summary of the experimental results (A = 50 mm tall RPC, B = 100 mm tall RPC, PP = free-fall pure pyrolysis, SG = free-fall steam-based gasification, all values are on a H <sub>2</sub> O, N <sub>2</sub> and Ar free basis).....	65
<b>Table 7-2:</b>	Summary of the statistical analysis for the effects of reactor configurations: for comparison X vs. Y “>” or “<” designate statistically higher or lower mean of a response for the configuration X; “~” designates no statistically significant difference.....	69
<b>Table 7-3:</b>	Energy flows in the solar reactor.....	80
<b>Table 8-1:</b>	Thermocouple positions: W = wall, C = centerline.....	86
<b>Table 8-2:</b>	Heat- and mass-transfer property correlations.....	96

<b>Table 8-3:</b>	Parameters used in order verification study (all in SI units) ...	100
<b>Table 8-4:</b>	Simulation results for a 1 m tall / 0.06 m inner diameter domain with $d_{\text{nom}} = 2.54 \text{ mm}$ , $k_s = k_{\text{SiC}}$ , $\varphi_{\text{RPC}} = 89\%$ , $\dot{m}_{\text{f,in}} = 2 \text{ g/s}$ , $T_{\text{f,in}} = 873 \text{ K}$ , and $l = 0.2$ .....	104
<b>Table A-1:</b>	Physical and chemical properties of dry microalgae: Ultimate and proximate analyses, heating value and mean particle size.....	123
<b>Table A-2:</b>	Summary of the experimental results (integral values averaged over all replicates). ....	129

## References

- [1] IEA, *World Energy Outlook 2013*: IEA, 2013.
- [2] S. Solomon, I. P. o. C. Change, and I. P. o. C. C. W. G. I., *Climate Change 2007 - The Physical Science Basis: Working Group I Contribution to the Fourth Assessment Report of the IPCC*: Cambridge University Press, 2007.
- [3] A. Steinfeld and R. Palumbo, "Solar Thermochemical Process Technology", in *Encyclopedia of Physical Science and Technology (Third Edition)*, A. M. Robert, Ed., ed New York: Academic Press, 2003, pp. 237-256.
- [4] A. Steinfeld, "Thermochemical production of syngas using concentrated solar energy", *Annual Review of Heat Transfer*, vol. 15(15), 2012.
- [5] A. V. Bridgwater, "The technical and economic feasibility of biomass gasification for power generation", *Fuel*, vol. 74(5), pp. 631-653, 1995.
- [6] P. De Filippis, C. Borgianni, M. Paolucci, and F. Pochetti, "Gasification process of Cuban bagasse in a two-stage reactor", *Biomass and Bioenergy*, vol. 27(3), pp. 247-252, 2004.
- [7] E. O. Gómez, L. A. B. Cortez, E. S. Lora, C. G. Sanchez, and A. Bauen, "Preliminary tests with a sugarcane bagasse fueled fluidized-bed air gasifier", *Energy Conversion and Management*, vol. 40(2), pp. 205-214, 1999.
- [8] M. Gabra, E. Pettersson, R. Backman, and B. Kjellström, "Evaluation of cyclone gasifier performance for gasification of sugar cane residue – Part 1: gasification of bagasse", *Biomass and Bioenergy*, vol. 21(5), pp. 351-369, 2001.
- [9] L. F. Pellegrini and J. S. de Oliveira, "Exergy analysis of sugarcane bagasse gasification", *Energy*, vol. 32(4), pp. 314-327, 2007.

- [10] N. Piatkowski, C. Wieckert, A. W. Weimer, and A. Steinfeld, "Solar-driven gasification of carbonaceous feedstock-a review", *Energy & Environmental Science*, vol. 4(1), pp. 73-82, 2011.
- [11] R. W. Taylor, R. Berjoan, and J. P. Coutures, "Solar gasification of carbonaceous materials", *Solar Energy*, vol. 30(6), pp. 513-525, 1983.
- [12] J. Corella, J. M. Toledo, and G. Molina, "A review on dual fluidized-bed biomass gasifiers", *Industrial & Engineering Chemistry Research*, vol. 46(21), pp. 6831-6839, 2007.
- [13] P. McKendry, "Energy production from biomass (Part 1): Overview of biomass", *Bioresour Technol*, vol. 83(1), pp. 37-46, 2002.
- [14] P. Basu, *Biomass gasification and pyrolysis: practical design and theory*. Burlington, MA: Academic Press, 2010.
- [15] E. Rensfelt, G. Blomqvist, C. Ekström, S. Engström, B. Espents, and L. Linnankki, "Basic gasification studies for development of biomass medium-BTU gasification processes", presented at the Energy from Biomass and Wastes, Washington, D.C., 1978.
- [16] F. Shafizadeh, "Introduction to Pyrolysis of Biomass", in *Specialists' workshop on fast pyrolysis of biomass*, Copper Mountain, CO, pp. 79-103, 1980.
- [17] C. Fushimi, K. Araki, Y. Yamaguchi, and A. Tsutsumi, "Effect of Heating Rate on Steam Gasification of Biomass. 1. Reactivity of Char", *Industrial & Engineering Chemistry Research*, vol. 42(17), pp. 3922-3928, 2003.
- [18] R. Zanzi, K. Sjöström, and E. Björnbom, "Rapid high-temperature pyrolysis of biomass in a free-fall reactor", *Fuel*, vol. 75(5), pp. 545-550, 1996.
- [19] F. Mermoud, S. Salvador, L. Van de Steene, and F. Golfier, "Influence of the pyrolysis heating rate on the steam gasification rate of large wood char particles", *Fuel*, vol. 85(10-11), pp. 1473-1482, 2006.
- [20] I. Milosavljevic, V. Oja, and E. M. Suuberg, "Thermal effects in cellulose pyrolysis: Relationship to char formation processes",

- Industrial & Engineering Chemistry Research*, vol. 35(3), pp. 653-662, 1996.
- [21] J. F. Stubington and S. Aiman, "Pyrolysis kinetics of bagasse at high heating rates", *Energy & Fuels*, vol. 8(1), pp. 194-203, 1994.
  - [22] Y. Zhang, S. Kajitani, M. Ashizawa, and K. Miura, "Peculiarities of Rapid Pyrolysis of Biomass Covering Medium- and High-Temperature Ranges", *Energy & Fuels*, vol. 20(6), pp. 2705-2712, 2006.
  - [23] Y. Zhang, S. Kajitani, M. Ashizawa, and Y. Oki, "Tar destruction and coke formation during rapid pyrolysis and gasification of biomass in a drop-tube furnace", *Fuel*, vol. 89(2), pp. 302-309, 2010.
  - [24] C. Higman and M. v. d. Burgt, *Gasification*, 2nd ed. Amsterdam ; Boston: Gulf Professional Pub./Elsevier Science, 2008.
  - [25] L. Devi, K. J. Ptasiński, and F. J. J. G. Janssen, "A review of the primary measures for tar elimination in biomass gasification processes", *Biomass & Bioenergy*, vol. 24(2), pp. 125-140, 2003.
  - [26] H. Knoef and J. Ahrenfeldt, *Handbook biomass gasification*: AE Enschede: btg, 2005.
  - [27] T. A. Milne, R. J. Evans, and N. Abatzoglou, "Biomass Gasifier "Tars": Their Nature, Formation, and Conversion", National Renewable Energy Laboratory, Golden, CO NREL/TP-570-25357, 1998.
  - [28] R. G. Graham and R. Bain, *Biomass gasification hot-gas clean-up*: IEA biomass gasification working group, 1993.
  - [29] R. Evans and T. Milne, "Chemistry of Tar Formation and Maturation in the Thermochemical Conversion of Biomass", in *Developments in Thermochemical Biomass Conversion*, A. V. Bridgwater and D. G. B. Boocock, Eds., ed: Springer Netherlands, 1997, pp. 803-816.
  - [30] H. Hofbauer, R. Rauch, G. Loeffler, S. Kaiser, E. Fercher, and H. Tremmel, "Six years experience with the FICFB-gasification process", in *12th European Conference and Technology Exhibition on Biomass for Energy, Industry and Climate Protection*, pp. 982-985, 2002.

- [31] N. Piatkowski, "Solar driven steam gasification of carbonaceous feedstocks: Feedstock characterization to pilot facility testing", Doctor of Sciences, ETH Zurich, 2011.
- [32] D. Trommer, F. Noembrini, M. Fasciana, D. Rodriguez, A. Morales, M. Romero, and A. Steinfield, "Hydrogen production by steam-gasification of petroleum coke using concentrated solar power – I. Thermodynamic and kinetic analyses", *International Journal of Hydrogen Energy*, vol. 30(6), pp. 605-618, 2005.
- [33] R. Müller, P. von Zedtwitz, A. Wokaun, and A. Steinfield, "Kinetic investigation on steam gasification of charcoal under direct high-flux irradiation", *Chemical Engineering Science*, vol. 58(22), pp. 5111-5119, 2003.
- [34] P. von Zedtwitz and A. Steinfield, "Steam-Gasification of Coal in a Fluidized-Bed/Packed-Bed Reactor Exposed to Concentrated Thermal Radiation – Modeling and Experimental Validation", *Industrial & Engineering Chemistry Research*, vol. 44(11), pp. 3852-3861, 2005.
- [35] A. Z'Graggen, P. Haueter, D. Trommer, M. Romero, J. De Jesus, and A. Steinfield, "Hydrogen production by steam-gasification of petroleum coke using concentrated solar power – II Reactor design, testing, and modeling", *International Journal of Hydrogen Energy*, vol. 31(6), pp. 797-811, 2006.
- [36] D. W. Gregg, R. W. Taylor, J. H. Campbell, J. R. Taylor, and A. Cotton, "Solar gasification of coal, activated carbon, coke and coal and biomass mixtures", *Solar Energy*, vol. 25(4), pp. 353-364, 1980.
- [37] J. P. Murray and E. A. Fletcher, "Reaction of steam with cellulose in a fluidized bed using concentrated sunlight", *Energy*, vol. 19(10), pp. 1083-1098, 1994.
- [38] P. Lichy, C. Perkins, B. Woodruff, C. Bingham, and A. Weimer, "Rapid High Temperature Solar Thermal Biomass Gasification in a Prototype Cavity Reactor", *Journal of Solar Energy Engineering*, vol. 132(1), pp. 0110121-0110127, 2010.
- [39] T. Melchior, C. Perkins, P. Lichy, A. W. Weimer, and A. Steinfield, "Solar-driven biochar gasification in a particle-flow reactor", *Chemical*

- 
- Engineering and Processing: Process Intensification*, vol. 48(8), pp. 1279-1287, 2009.
- [40] N. Piatkowski, C. Wieckert, and A. Steinfield, "Experimental investigation of a packed-bed solar reactor for the steam-gasification of carbonaceous feedstocks", *Fuel Processing Technology*, vol. 90(3), pp. 360-366, 2009.
  - [41] C. Perkins, Z. Jovanovic, S. Strand, C. Hilton, and D. Kelley, "Systems and methods for an indirect radiation driven gasifier reactor & receiver configuration", US 2010/0303692 A1 Patent US 2010/0303692 A1, 2010.
  - [42] A. Z'Graggen, P. Haueter, G. Maag, A. Vidal, M. Romero, and A. Steinfield, "Hydrogen production by steam-gasification of petroleum coke using concentrated solar power – III. Reactor experimentation with slurry feeding", *International Journal of Hydrogen Energy*, vol. 32(8), pp. 992-996, 2007.
  - [43] A. Z'Graggen, P. Haueter, G. Maag, M. Romero, and A. Steinfield, "Hydrogen production by steam-gasification of carbonaceous materials using concentrated solar energy – IV. Reactor experimentation with vacuum residue", *International Journal of Hydrogen Energy*, vol. 33(2), pp. 679-684, 2008.
  - [44] N. Piatkowski and A. Steinfield, "Solar-Driven Coal Gasification in a Thermally Irradiated Packed-Bed Reactor", *Energy & Fuels*, vol. 22(3), pp. 2043-2052, 2008.
  - [45] J. Lede, F. Verzaro, B. Antoine, and J. Villermaux, "Flash pyrolysis of wood in a cyclone reactor", *Chemical Engineering and Processing: Process Intensification*, vol. 20(6), pp. 309-317, 1986.
  - [46] T. Melchior and A. Steinfield, "Radiative Transfer Within a Cylindrical Cavity With Diffusely/Specularly Reflecting Inner Walls Containing an Array of Tubular Absorbers", *Journal of Solar Energy Engineering*, vol. 130(2), pp. 0210131-0210137, 2008.
  - [47] T. Melchior, C. Perkins, A. W. Weimer, and A. Steinfield, "A cavity receiver containing a tubular absorber for high-temperature thermochemical processing using concentrated solar energy",

- International Journal of Thermal Sciences*, vol. 47(11), pp. 1496-1503, 2008.
- [48] A. Z'Graggen and A. Steinfeld, "Hydrogen production by steam-gasification of carbonaceous materials using concentrated solar energy – V. Reactor modeling, optimization, and scale-up", *International Journal of Hydrogen Energy*, vol. 33(20), pp. 5484-5492, 2008.
- [49] K. Svoboda, M. Pohořelý, M. Hartman, and J. Martinec, "Pretreatment and feeding of biomass for pressurized entrained flow gasification", *Fuel Processing Technology*, vol. 90(5), pp. 629-635, 2009.
- [50] G. Maag and A. Steinfeld, "Design of a 10 MW Particle-Flow Reactor for Syngas Production by Steam-Gasification of Carbonaceous Feedstock Using Concentrated Solar Energy", *Energy & Fuels*, vol. 24(12), pp. 6540-6547, 2010.
- [51] A. Steinfeld, "Solar hydrogen production via a two-step water-splitting thermochemical cycle based on Zn/ZnO redox reactions", *International Journal of Hydrogen Energy*, vol. 27(6), pp. 611-619, 2002.
- [52] A. Meier, N. Gremaud, and A. Steinfeld, "Economic evaluation of the industrial solar production of lime", *Energy Conversion and Management*, vol. 46(6), pp. 905-926, 2005.
- [53] R. Pitz-Paal, N. B. Botero, and A. Steinfeld, "Heliostat field layout optimization for high-temperature solar thermochemical processing", *Solar Energy*, vol. 85(2), pp. 334-343, 2011.
- [54] S. Q. Turn, B. M. Jenkins, L. A. Jakeway, L. G. Blevins, R. B. Williams, G. Rubenstein, and C. M. Kinoshita, "Test results from sugar cane bagasse and high fiber cane co-fired with fossil fuels", *Biomass and Bioenergy*, vol. 30(6), pp. 565-574, 2006.
- [55] R. P. Beeharry, "Extended sugarcane biomass utilisation for exportable electricity production in mauritius", *Biomass & Bioenergy*, vol. 11(6), pp. 441-449, 1996.
- [56] A. Pandey, C. R. Soccol, P. Nigam, and V. T. Soccol, "Biotechnological potential of agro-industrial residues. I: sugarcane bagasse", *Bioresource Technology*, vol. 74(1), pp. 69-80, 2000.

- 
- [57] FAOSTAT. (2011, 09/21/2011). *FAOSTAT database*. Available: <http://faostat.fao.org/site/567/default.aspx#ancor>
  - [58] F. Teixeira, "Bagaço de cana-de-açúcar na alimentação de bovinos", *Revista eletrónica de veterinária*, vol. 8(6), pp. 1695-1704, 2007.
  - [59] A. Roine, "Outokumpu HSC Chemistry", ed. Pori, Finland: Outokumpu Research, 1997.
  - [60] A. Steinfeld, C. Larson, R. Palumbo, and M. Foley, "Thermodynamic analysis of the co-production of zinc and synthesis gas using solar process heat", *Energy*, vol. 21(3), pp. 205-222, 1996.
  - [61] E. A. Fletcher and R. L. Moen, "Hydrogen-and Oxygen from Water", *Science*, vol. 197(4308), pp. 1050-1056, 1977.
  - [62] A. Bejan, *Entropy generation through heat and fluid flow*: Wiley New York, 1982.
  - [63] N. Sato, *Chemical energy and exergy: An introduction to chemical thermodynamics for engineers*. Amsterdam; Boston: Elsevier, 2004.
  - [64] M. J. Moran and H. N. Shapiro, *Fundamentals of engineering thermodynamics: SI version*, 5th ed. Hoboken, NJ: Wiley, 2006.
  - [65] J. Szargut, D. R. Morris, and F. R. Steward, *Exergy analysis of thermal, chemical, and metallurgical processes*. New York, NY: Hemisphere Publishing, 1988.
  - [66] C. C. M. Wu, T. Yosenick, C. Kim, M. Kahn, and M. Chase, "Continuous poling of PZT bars", *Manufacturing of Electronic Materials and Components*, vol. 90, pp. 21-31, 1998.
  - [67] M. Holmgren, "XSteam", ed: [www.x-eng.com](http://www.x-eng.com), 2006.
  - [68] J. Hong, G. Chaudhry, J. G. Brisson, R. Field, M. Gazzino, and A. F. Ghoniem, "Analysis of oxy-fuel combustion power cycle utilizing a pressurized coal combustor", *Energy*, vol. 34(9), pp. 1332-1340, 2009.
  - [69] I. Pfaff and A. Kather, "Comparative thermodynamic analysis and integration issues of CCS steam power plants based on oxy-combustion

- with cryogenic or membrane based air separation", *Energy Procedia*, vol. 1(1), pp. 495-502, 2009.
- [70] W. T. Welford and R. Winston, *High collection nonimaging optics*. San Diego: Academic Press, 1989.
- [71] M. Barrio, B. Gøbel, H. Rimes, U. Henriksen, J. E. Hustad, and L. H. Sørensen, "Steam Gasification of Wood Char and the Effect of Hydrogen Inhibition on the Chemical Kinetics", in *Progress in Thermochemical Biomass Conversion*, ed: Blackwell Science Ltd, 2008, pp. 32-46.
- [72] A. Moilanen and H.-J. Mühlen, "Characterization of gasification reactivity of peat char in pressurized conditions: Effect of product gas inhibition and inorganic material", *Fuel*, vol. 75(11), pp. 1279-1285, 1996.
- [73] C. Di Blasi, "Combustion and gasification rates of lignocellulosic chars", *Progress in Energy and Combustion Science*, vol. 35(2), pp. 121-140, 2009.
- [74] K. J. Hüttinger and W. F. Merdes, "The carbon-steam reaction at elevated pressure: Formations of product gases and hydrogen inhibitions", *Carbon*, vol. 30(6), pp. 883-894, 1992.
- [75] S. Kimura, S. Tone, and T. Otake, "Reaction order in the grain model with grain size distribution", *J. Chem. Engng Japan*, vol. 14(6), pp. 491-493, 1981.
- [76] O. Levenspiel, *Chemical reaction engineering*, 3rd ed. New York: Wiley, 1999.
- [77] Z. R. Jovanovic, "Kinetics of direct nitridation of pelletized silicon grains in a fluidized bed: experiment, mechanism and modelling", *Journal of Materials Science*, vol. 33(9), pp. 2339-2355, 1998.
- [78] R. Bryan Woodruff and A. W. Weimer, "A novel technique for measuring the kinetics of high-temperature gasification of biomass char with steam", *Fuel*, vol. 103(0), pp. 749-757, 2013.
- [79] P. Simell, P. Ståhlberg, E. Kurkela, J. Albrecht, S. Deutsch, and K. Sjöström, "Provisional protocol for the sampling and analysis of tar and

- particulates in the gas from large-scale biomass gasifiers. Version 1998", *Biomass and Bioenergy*, vol. 18(1), pp. 19-38, 2000.
- [80] A. Demirbas, D. Gullu, A. ÇAglar, and F. Akdeniz, "Estimation of Calorific Values of Fuels from Lignocellulosics", *Energy Sources*, vol. 19(8), pp. 765-770, 1997.
- [81] E. Natarajan, M. Öhman, M. Gabra, A. Nordin, T. Liliedahl, and A. N. Rao, "Experimental determination of bed agglomeration tendencies of some common agricultural residues in fluidized bed combustion and gasification", *Biomass and Bioenergy*, vol. 15(2), pp. 163-169, 1998.
- [82] L. V. Barysheva, E. S. Borisova, V. M. Khanaev, V. A. Kuzmin, I. A. Zolotarskii, N. A. Pakhomov, and A. S. Noskov, "Motion of particles through the fixed bed in a gas-solid-solid downflow reactor", *Chemical Engineering Journal*, vol. 91(2-3), pp. 219-225, 2003.
- [83] A. W. M. Roes and W. P. M. Van Swaaij, "Hydrodynamic behaviour of a gas—solid counter-current packed column at trickle flow", *The Chemical Engineering Journal*, vol. 17(2), pp. 81-89, 1979.
- [84] E. Saatdjian and J. F. Large, "Heat transfer simulation in a raining packed bed exchanger", *Chemical Engineering Science*, vol. 40(5), pp. 693-697, 1985.
- [85] K. R. Westerterp and M. Kuczynski, "Gas-solid trickle flow hydrodynamics in a packed column", *Chemical Engineering Science*, vol. 42(7), pp. 1539-1551, 1987.
- [86] J. H. A. Kiel, W. Prins, and W. P. M. Van Swaaij, "Modelling of non-catalytic reactions in a gas-solid trickle flow reactor: dry, regenerative flue gas desulphurisation using a silica-supported copper oxide sorbent", *Chemical Engineering Science*, vol. 47(17-18), pp. 4271-4286, 1992.
- [87] A. B. Verver and W. P. M. Vanswaij, "The Heat-Transfer Performance of Gas Solid Trickle Flow over a Regularly Stacked Packing", *Powder Technology*, vol. 45(2), pp. 133-144, 1986.
- [88] A. David, "Experimental demonstration of a novel drop-tube packed bed solar gasifier for sugarcane bagasse", Semester project, Department of Mechanical and Process Engineering, ETH Zürich, 2012.

- [89] I. Hischier, P. Leumann, and A. Steinfeld, "Experimental and Numerical Analyses of a Pressurized Air Receiver for Solar-Driven Gas Turbines", *Journal of Solar Energy Engineering*, vol. 134(2), pp. 021003-8, 2012.
- [90] W. T. Welford and R. Winston, *High collection nonimaging optics*. San Diego: Academic Press, 1989.
- [91] J. Petrasch, P. Coray, A. Meier, M. Brack, P. Haberling, D. Wuillemin, and A. Steinfeld, "A Novel 50 kW 11,000 suns High-Flux Solar Simulator Based on an Array of Xenon Arc Lamps", *Journal of Solar Energy Engineering*, vol. 129(4), pp. 405-411, 2007.
- [92] M. Kruesi, Z. R. Jovanovic, E. C. dos Santos, H. C. Yoon, and A. Steinfeld, "Solar-driven steam-based gasification of sugarcane bagasse in a combined drop-tube and fixed-bed reactor – Thermodynamic, kinetic, and experimental analyses", *Biomass and Bioenergy*, vol. 52, pp. 173-183, 2013.
- [93] F. E. Grubbs, "Procedures for Detecting Outlying Observations in Samples", *Technometrics*, vol. 11(1), pp. 1-21, 1969.
- [94] C. Erlich and T. H. Fransson, "Downdraft gasification of pellets made of wood, palm-oil residues respective bagasse: Experimental study", *Applied Energy*, vol. 88(3), pp. 899-908, 2011.
- [95] R. Siegel and J. R. Howell, *Thermal radiation heat transfer*, 4th ed. New York: Taylor & Francis, 2002.
- [96] J. Petrasch, "A Free and Open Source Monte Carlo Ray Tracing Program for Concentrating Solar Energy Research", *ASME Conference Proceedings*, vol. 2010(43956), pp. 125-132, 2010.
- [97] Y. S. Touloukian and D. P. DeWitt, *Thermal radiative properties: nonmetallic solids*. New York,: IFI/Plenum, 1972.
- [98] M. F. Modest, *Radiative heat transfer*, 2nd ed. Amsterdam ; Boston: Academic Press, 2003.
- [99] ANSYS Inc., "CFX 13.0", 13.0 ed, 2010.
- [100] Y. A. Çengel, *Heat Transfer: A Practical Approach*: McGraw-Hill, 2003.

- 
- [101] A. M. Clausing, "Convective Losses from Cavity Solar Receivers - Comparisons between Analytical Predictions and Experimental Results", *Journal of Solar Energy Engineering-Transactions of the ASME*, vol. 105(1), pp. 29-33, 1983.
  - [102] Design Institute for Physical Properties, Sponsored by AIChE, "DIPPR Project 801 - Full Version", ed: Design Institute for Physical Property Research/AIChE, 2010.
  - [103] J. P. Holman, *Heat transfer*, 10th ed. Boston: McGraw Hill Higher Education, 2010.
  - [104] *VDI-Wärmeatlas*, 10 ed. Berlin: Verein Deutscher Ingenieure VDI-Gesellschaft Verfahrenstechnik und Chemieingenieurwesen (GVC), 2006.
  - [105] M. Kruesi, Z. R. Jovanovic, and A. Steinfield, "A two-zone solar-driven gasifier concept: Reactor design and experimental evaluation with bagasse particles", *Fuel*, vol. 117, Part A, pp. 680-687, 2014.
  - [106] T. Poinsot and D. Veynante, *Theoretical and numerical combustion*, 2nd ed. Philadelphia: Edwards, 2005.
  - [107] A. Moilanen, K. Saviharju, and T. Harju, "Steam Gasification Reactivities of Various Fuel Chars", in *Advances in Thermochemical Biomass Conversion*, A. V. Bridgwater, Ed., ed: Springer Netherlands, 1993, pp. 131-141.
  - [108] R. H. Leuenberger and R. A. Person, "Compilation of Radiation Shape Factors for Cylindrical Assemblies", presented at the ASME paper 56-A-144, ASME Annual Meeting, New York, 1956.
  - [109] A. J. Buschman and C. M. Pittman, "Configuration factors for exchange of radiant energy between axisymmetrical sections of cylinders, cones and hemispheres and their bases", *NASA TN D-944*, 1961.
  - [110] R. Siegel, "Transient Radiative Cooling of a Droplet-Filled Layer", *Journal of Heat Transfer-Transactions of the ASME*, vol. 109(1), pp. 159-164, 1987.
  - [111] S. Suter and S. Haussener, "Morphology Engineering of Porous Media for Enhanced Solar Fuel and Power Production", *JOM*, pp. 1-8, 2013.

- [112] J. Petrasch, "Multi-scale analyses of reactive flow in porous media", Doctor of Sciences, ETH Zurich, 2007.
- [113] E. N. Fuller, Schettle.Pd, and J. C. Giddings, "A New Method for Prediction of Binary Gas-Phase Diffusion Coefficients", *Industrial and Engineering Chemistry*, vol. 58(5), pp. 19-27, 1966.
- [114] D. F. Fairbanks and C. R. Wilke, "Diffusion Coefficients in Multicomponent Gas Mixtures", *Industrial & Engineering Chemistry*, vol. 42(3), pp. 471-475, 1950.
- [115] R. G. Munro, "Material properties of a sintered alpha-SiC", *Journal of Physical and Chemical Reference Data*, vol. 26(5), pp. 1195-1203, 1997.
- [116] C. L. Yaws, *Transport Properties of Chemicals and Hydrocarbons: Viscosity, Thermal Conductivity, and Diffusivity for more than 7800 Hydrocarbons and Chemicals, Including C1 to C100 Organics and Ac to Zr Inorganics*: Elsevier Science, 2009.
- [117] M. W. Chase and National Institute of Standards and Technology (U.S.), *NIST-JANAF thermochemical tables*, 4th ed.: American Chemical Society, Washington, DC; American Institute of Physics for the National Institute of Standards and Technology, New York, 1998.
- [118] D. Merrick, "Mathematical-Models of the Thermal-Decomposition of Coal .2. Specific-Heats and Heats of Reaction", *Fuel*, vol. 62(5), pp. 540-546, 1983.
- [119] D. B. Spalding, "A novel finite difference formulation for differential expressions involving both first and second derivatives", *International Journal for Numerical Methods in Engineering*, vol. 4(4), pp. 551-559, 1972.
- [120] T. A. Davis, "Algorithm 832: UMFPACK V4.3 – an unsymmetric-pattern multifrontal method", *ACM Trans. Math. Softw.*, vol. 30(2), pp. 196-199, 2004.
- [121] P. J. Roache, "Code verification by the method of manufactured solutions", *Journal of Fluids Engineering-Transactions of the Asme*, vol. 124(1), pp. 4-10, 2002.

- 
- [122] P. Knupp and K. Salari, *Verification of Computer Codes in Computational Science and Engineering*: Chapman and Hall/CRC, 2002.
  - [123] S. Yagi and D. Kunii, "Studies on Effective Thermal Conductivities in Packed Beds", *AICHE Journal*, vol. 3(3), pp. 373-381, 1957.
  - [124] M. A. N. Coelho and J. R. F. Guedes de Carvalho, "Transverse dispersion in granular beds. I: Mass transfer from a wall and the dispersion coefficient in packed beds", *Chemical Engineering Research & Design*, vol. 66(2), 1988.
  - [125] J. M. P. Q. Delgado, "A critical review of dispersion in packed beds", *Heat and Mass Transfer*, vol. 42(4), pp. 279-310, 2006.
  - [126] P. C. Carman, "Fluid Flow Through Granular Beds", *Transactions - Institution of Chemical Engineers*, vol. 15, pp. 150-166, 1937.
  - [127] A. Gopalratnam, "Algal Biofuels: The Backstory", *Chemical Engineering Progress*, vol. 107(3), pp. 35-36, 2011.
  - [128] A. Demirbas, "Use of algae as biofuel sources", *Energy Conversion and Management*, vol. 51(12), pp. 2738-2749, 2010.
  - [129] G. Shelef, A. Sukenik, and M. Green, "Microalgae harvesting and processing: a literature review", SERI/STR-231-2396; Other: ON: TI84013036 United States10.2172/6204677Other: ON: TI84013036Thu Mar 06 08:02:44 EST 2008NTIS, PC A04.NREL; EDB-84-189417English, 1984.
  - [130] E. P. Knoshaug and A. Darzins, "Algal Biofuels: The Process", *Chemical Engineering Progress*, vol. 107(3), pp. 37-47, 2011.
  - [131] US DOE, "National algal biofuels technology roadmap", *US Department of Energy, Office of Energy Efficiency and Renewable Energy, Biomass Program*, 2010.
  - [132] A. Hirano, K. Hon-Nami, S. Kunito, M. Hada, and Y. Ogushi, "Temperature effect on continuous gasification of microalgal biomass: theoretical yield of methanol production and its energy balance", *Catalysis Today*, vol. 45(1-4), pp. 399-404, 1998.

- [133] A. Zbogar, F. J. Frandsen, P. A. Jensen, and P. Glarborg, "Heat transfer in ash deposits: A modelling tool-box", *Progress in Energy and Combustion Science*, vol. 31(5-6), pp. 371-421, 2005.
- [134] B. Atkinson and D. Merrick, "Mathematical-Models of the Thermal-Decomposition of Coal, 4. Heat-Transfer and Temperature Profiles in a Coke-Oven Charge", *Fuel*, vol. 62(5), pp. 553-561, 1983.
- [135] J. Fjellerup, U. Henriksen, A. D. Jensen, P. A. Jensen, and P. Glarborg, "Heat transfer in a fixed bed of straw char", *Energy & Fuels*, vol. 17(5), pp. 1251-1258, 2003.
- [136] S. V. Patankar, *Numerical Heat Transfer and Fluid Flow*: Hemisphere Publishing Corporation, 1980.

## List of Publications

### Journal Papers:

M. Kruesi, M. E. Galvez, M. Halmann, and A. Steinfeld, "Solar Aluminum Production by Vacuum Carbothermal Reduction of Alumina—Thermodynamic and Experimental Analyses", *Metallurgical and Materials Transactions B*, vol. 42, pp. 254-260, 2011.

M. Kruesi, Z. R. Jovanovic, E. C. dos Santos, H. C. Yoon, and A. Steinfeld, "Solar-driven steam-based gasification of sugarcane bagasse in a combined drop-tube and fixed-bed reactor – Thermodynamic, kinetic, and experimental analyses", *Biomass and Bioenergy*, vol. 52, pp. 173-183, 2013.

M. Kruesi, Z. R. Jovanovic, and A. Steinfeld, "A two-zone solar-driven gasifier concept: Reactor design and experimental evaluation with bagasse particles", *Fuel*, vol. 117, Part A, pp. 680-687, 2014.

M. Kruesi, Z. R. Jovanovic, A. Haselbacher, and A. Steinfeld, "Analysis of Solar-Driven Gasification of Biochar Trickling through an Interconnected Porous Structure", *submitted*